
GAZİ ÜNİVERSİTESİ
Gazi
1926

SIMULATION AND EXPERIMENTAL STUDIES OF MELTING PROCESS IN ADDITIVE MANUFACTURING

A THESIS SUBMITTED TO
THE GRADUATE SCHOOL OF NATURAL AND APPLIED SCIENCES
OF
GAZİ UNIVERSITY

BY
Peyman ANSARI

IN PARTIAL FULFILLMENT OF THE REQUIREMENTS
FOR
THE DEGREE OF DOCTOR OF PHILOSOPHY
IN
MECHANICAL ENGINEERING

FEBRUARY 2022

ETHICAL STATEMENT

I hereby declare that in this thesis study I prepared in accordance with thesis writing rules of Gazi University Graduate School of Natural and Applied Sciences;

- All data, information and documents presented in this thesis have been obtained within the scope of academic rules and ethical conduct,
- All information, documents, assessments and results have been presented in accordance with scientific ethical conduct and moral rules,
- All material used in this thesis that are not original to this work have been fully cited and referenced,
- No change has been made in the data used,
- The work presented in this thesis is original,

or else, I admit all loss of rights to be incurred against me.

PEYMAN ANSARI

15/02/2022

EKLEMELİ İMALATTA ERGİTME PROSESİNİN SİMÜLASYONU VE DENEYSEL ÇALIŞMALARI

(Doktora Tezi)

Peyman ANSARİ

GAZİ ÜNİVERSİTESİ

FEN BİLİMLERİ ENSTİTÜSÜ

Şubat 2022

ÖZET

Seçici Lazer Ergitmede (SLE) nihai ürünün kalitesinde önemli rol oynayan faktör, üretimde kullanılan proses parametre setidir. Genel olarak, bu fabrikasyon parametre setleri, malzemenin enerji yoğunluğu gereksinimleri kullanılarak deneysel olarak elde edilir. Deneysel araştırma, kısmen zaman ve maliyet tüketen bir süreç olan deneme yanılma yaklaşımıdır. Öte yandan, ergiyik havuzunun sıcaklığının izin verilen aralıkta tutulması, uygulanan proses parametre setlerinin hakim olduğu ve sıcaklık dalgalanmalarının önlenmesi, üretimin stabilitesini ve dolayısıyla nihai ürünün kalitesini etkiler. Bu tez, malzeme ortamı olarak Paslanmaz Çelik 316L, AlSi10Mg ve Ti6Al4V metal alaşım tozlarını kullanarak bir SLE işleminde parametrelerin elde edilmesi için çok fizikli bir sayısal model yaklaşımı sunmaktadır. Önerilen yaklaşım, proses parametreleri ve oluşturdukları sıcaklık arasındaki matematiksel ilişkiler sağlar. Farklı tarama hızlarında lazer gücü ve lazer nokta çapının sıcaklık üzerindeki etkisi araştırılarak her iki metal alaşım tozları için geniş proses parametre setleri elde edilmiştir. Ayrıca, ergiyik havuzu sıcaklığını anlık olarak kontrol edecek bir kontrolör tasarlamak için temel sistem transfer fonksiyonu yapısını oluşturacak farklı tarama hızlarında lazer gücü-sıcaklığı ve lazer nokta çapı-sıcaklığı arasındaki matematiksel ilişkiler geliştirilmiştir. Simülasyonlardan elde edilen parametre setleri kullanılarak, modeli doğrulamak için mikroyapı inceleme ve mekanik test çalışmaları yapılmıştır. Bunun için test numuneleri üretilerek deneysel doğrulama çalışmaları yapılmıştır. Yetersiz sıcaklıktan kaynaklanan ergimemiş tozlar ve bağlantısız ergiyik havuzu kusurları, aşırı sıcaklıktan kaynaklanan buharlaşma kusurları ve simülasyonlarla tahmin edilen uygun ve homojen mikroyapılar sonucunda mikroyapı ve mekanik özellikleri etkileyen model doğrulanmıştır. Deneysel çalışma, üretilen test numunelerinin mikroyapı ve çekme özellikleri incelenerek gerçekleştirilmiştir.

Bilim Kodu : 91418

Anahtar Kelimeler : Eklemeli imalat, seçici lazer ergitme, proses parametresi, matematiksel ilişki, transfer fonksiyonu, 316L paslanmaz çelik, AlSi10Mg, Ti6Al4V, sonlu elemanlar yöntemi, simülasyon

Sayfa Adedi : 114

Danışman : Prof. Dr. Metin U. SALAMCI

SIMULATION AND EXPERIMENTAL STUDIES OF MELTING PROCESS IN ADDITIVE MANUFACTURING

(Ph. D. Thesis)

Peyman ANSARI

GAZİ UNIVERSITY

GRADUATE SCHOOL OF NATURAL AND APPLIED SCIENCES

February 2022

ABSTRACT

The most important factors that play vital role in the quality of the final product in selective laser melting (SLM) are the process parameter sets used in production. In general, these fabrication parameter sets are obtained experimentally by using the energy density requirements of the material. The experimental investigation is partly a trial and error approach, which is a time and cost-consuming process. On the other hand, keeping the temperature of the melt pool in an allowable range, which is dominated by the applied process parameters sets, and preventing temperature fluctuations impress the stability of the production and therefore the quality of the final product. The thesis presents a multiphysics numerical model approach to obtain process parameters in an SLM additive manufacturing by using Stainless Steel 316L, AlSi10Mg and Ti6Al4V metal alloy powders as the material medium. The proposed approach provides mathematical relationships between the process parameters and the temperature they form. By investigating the effect of laser power and laser spot diameter on the temperature at different scanning velocities, wide process parameter sets were obtained for the powders. In addition, mathematical relationships between laser power-temperature and laser spot diameter-temperature at different scanning velocities, which could be considered as Transfer Functions to design a controller to control the melt pool temperature instantly, were developed. Using the parameter sets obtained from the simulations, microstructure investigation and mechanical testing studies were carried out to validate the model. Then, experimental validation studies were carried out by fabricating test samples. The un-melted powders and nonconnected melt pool defects due to insufficient temperature, evaporation defects caused by extreme temperature, and appropriate and homogeneous microstructures as a result of suitable parameters that were predicted through simulations, affecting microstructure and mechanical properties; validated the proposed model. The experimental study was carried out by examining the microstructure and tensile properties of the fabricated test samples.

Science Code : 91418

Key Words : Additive manufacturing, selective laser melting, process parameter, mathematical relationship, transfer functions, 316L stainless steel, AlSi10Mg, Ti6Al4V , FEM, simulation

Page Number : 114

Supervisor : Prof. Dr. Metin U. SALAMCI

ACKNOWLEDGMENT

I would like to express my deepest gratitude and thanks to Prof. Dr. Metin U. SALAMCI. I will be indebted to him for the rest of my life, as he has always been the key to my closed doors and the light of my darkness throughout my doctoral process. I will continue to learn from him.

My special thanks go to Assoc. Prof. Mickael Courtois for his unconditional help and support.

The EKTAM team deserve special thanks for their support and assistance.

I would like to express my gratitude to my mother, father, Parastou, and Sina, who are the only real meaning of my life, for their support, help, and encouragement.

Finally, I present my work to the streets of Tabriz.

CONTENTS

Page

ÖZET iv

ABSTRACT v

ACKNOWLEDGMENT vi

CONTENTS vii

LIST OF TABLES ix

LIST OF FIGURES xi

SYMBOLS AND ABBREVIATIONS xv

1. INTRODUCTION AND LITERATURE REVIEW 1

2. MATHEMATICAL MODELING OF SLM 9

2.1. Selective Laser Melting (SLM) 9

2.2. Governing Equations of Mathematical Modeling 10

2.2.1. Heat transfer equation 11

2.2.2. Navier-Stokes and conservation of mass equations 14

2.3. Multiphysics Model 15

2.4. Experimental Approach 17

3. SIMULATION RESULTS OF THE SLM PROCESS 21

3.1. Stainless Steel 316L 21

3.1.1. Effect of laser power 25

3.1.2. Effect of laser spot diameter 31

3.2. AlSi10Mg 37

3.2.1. Effect of laser power 39

3.2.2. Effect of laser spot diameter 45

Page

4. EXPERIMENTAL VALIDATION 51

4.1. Stainless Steel 316L 51

4.2. AlSi10Mg 61

4.2.1. Microstructure 64

4.2.2. Tensile behavior 73

5. AN IMPROVED MATHEMATICAL MODEL WITH PHASE FIELD PHYSICS 79

5.1. Governing Equations of Improved Mathematical Modeling 79

5.2. Results 82

5.2.1. Ti6Al4V 82

5.2.2. AlSi10Mg 93

6. CONCLUSION 103

REFERENCES 105

CURRICULUM VITAE 113

LIST OF TABLES

Table **Page**

Table 3.1. Equations of fitted curves of laser power–temperature simulation results with a laser spot diameter of 80 μm 28

Table 3.2. Equations of fitted curves of laser spot diameter–temperature simulation results with a laser power of 150 W 34

Table 3.3. Equations of the fitted curves for simulation results of the laser power-temperature during different scanning velocities 42

Table 3.4 Equations of the fitted curves for simulation results of the laser spot diameter-temperature at different scanning velocities. 48

Table 4.1. Results of the sieve analysis of powders used for fabrication of samples 51

Table 4.2. Powder size distribution of powders used for the fabrication of samples 51

Table 4.3. Material properties of Stainless Steel 316L 52

Table 4.4. Parameter sets of fabricated samples. A hatch space of 115 μm was used... 54

Table 4.5. Chemical composition of AlSi10Mg powder 61

Table 4.6. Powder size distribution of AlSi10Mg powder by light scattering as per ASTM B822 61

Table 4.7. Material Properties of AlSi10Mg..... 62

Table 4.8. Parameter sets of fabricated samples 64

Table 5.1. Material Properties of Ti6Al4V 85

Table 5.2. Equations of the fitted curves for simulation results of the laser power-melt pool width and laser power- melt pool life time for Ti6Al4V at different scanning velocities 88

Table 5.3. Equations of the fitted curves for simulation results of the scanning velocity-melt pool width and scanning velocity- melt pool life time for Ti6Al4V at different laser powers 92

Table 5.4. Equations of the fitted curves for simulation results of the laser power-melt pool width and laser power- melt pool life time for AlSi10Mg at different scanning velocities 97

Table **Page**

Table 5.5. Equations of the fitted curves for simulation results of the scanning velocity-melt pool width and scanning velocity- melt pool life time for AlSi10Mg at different laser powers 101

LIST OF FIGURES

Figure **Page**

Figure 1.1. The schematic illustration of the block diagram of the process control system. 8

Figure 2.1. (a) The schematic illustration of the SLM process; (b) The prepotent physical phenomena during the selective laser melting. 10

Figure 2.2. The representation of the heat source models, (a) cylindrical shape; (b) semi-spherical shape; (c) semi-ellipsoidal shape; (d) conical shape, (e) radiation transfer method; (f) ray-tracing method; (g) linearly decaying method; (h) exponentially decaying method. Here r_l is the radius of the laser beam; a, b, c are semi-axes parallel to the coordinate axes of x, y, z; a_f and a_r are the semi-axes of the front and rear ellipsoids; r_e and r_i are the radius at the top and bottom. 12

Figure 2.3. Description of the model, (a) powder bed; (b) ideal powder with a diameter of 40 μm; (c) symmetry view of the powders lined up on the powder bed; (d) complete view of the powders lined up on the powder bed. 16

Figure 2.4. Free Tetrahedral meshed powders 17

Figure 2.5. a) Pattern and dimensions of the fabricated samples of Stainless Steel 316L. Samples were cut in line with the plane (A) to examine the microstructure. b) Cutting and c) embedding the samples for microstructure inspection 19

Figure 2.6. Design and dimensions of fabricated samples for microstructure characterizations. 20

Figure 2.7. Schematic of the tensile test specimens following ASTM standard E8/E8M – 13a. 20

Figure 3.1. 3-D temperature distributions using 900 mm/s scanning velocity, 150 W laser power, and 50 μm laser spot diameter: (a) symmetry view, (b) complete view, (c) and isosurface view showing the zones with various temperature values at the moment. 22

Figure 3.2. Phase change from solid phase (0) to liquid phase (1). 23

Figure 3.3. Target point to record temperature during simulations 25

Figure 3.4. Simulation results and fitted curves of melt-pool temperature at various laser powers with a laser spot diameter of 80 μm and scanning velocity of (a) 600 mm/s, (b) 900 mm/s, (c) 1200 mm/s, and (d) 1400 mm/s. 24

Figure 3.5. Fitted curves of laser power–temperature during various scanning velocities with a laser spot diameter of 80 μm 30

Figure **Page**

Figure 3.6. Simulation results and fitted curves of melt-pool temperature at various laser spot diameters with a laser power of 150 W and scanning velocity of (a) 600 mm/s, (b) 900 mm/s, (c) 1200 mm/s, and (d) 1400 mm/s 31

Figure 3.7. Gaussian distribution of the heat source for laser spot diameters of (a) 50 μm, (b) 100 μm, (c) 150 μm, and (d) 200 μm..... 33

Figure 3.8. Fitted curves of laser spot diameter–temperature during various scanning velocities with a laser power of 150 W..... 36

Figure 3.9. 3-D temperature distribution using 800 mm/s scanning velocity, 200 W laser power and 140 μm laser spot diameter. a) Complete view, b) Symmetrical view of isosurface and contours distribution. c) Phase change during process from solid to liquid, while solid phase is denoted with 0 and the liquid phase is denoted with 1. 37

Figure 3.10. Phase change during process from solid to liquid, while solid phase is denoted with 0 and the liquid phase is denoted with 1..... 38

Figure 3.11. Simulation results and fitted curves of melt pool temperature at different laser powers and a laser spot diameter of 140 μm; scanning velocity of a) 600 mm/s, b) 800 mm/s, c) 1100 mm/s, and d) 1400 mm/s 40

Figure 3.12. Fitted Curves of the laser power- temperature for a laser spot diameter of 140 μm at different scanning velocities 44

Figure 3.13. Simulation results and fitted curves of melt pool temperature at different laser spot diameters and a laser power of 110 W; scanning velocity of a) 600 mm/s, b) 800 mm/s, c) 1100 mm/s, and d) 1400 mm/s 46

Figure 3.14. Fitted curves of the laser spot diameter- temperature for a Laser Power of 110 W at different scanning velocities..... 50

Figure 4.1. SEM image of Stainless Steel 316L powders used for the fabrication of samples. 53

Figure 4.2. Optical micrographs of fabricated samples after etching. Black regions are defects, and the building direction is perpendicular to the plane. The optical micrographs are arranged from sample (a) to sample (j), respectively. Table 7.4 can be consulted for the production parameters of the samples (scale bar: 100 μm). 55

Figure 4.3. SEM images of defects: void with melt-pool boundaries in the sample (a), a crack in the sample (b), entrapped gas pore in the sample (h), unmelted powders in the sample (j)..... 57

Figure **Page**

Figure 4.4. Reflection of SEM images of experimental results on simulation results with a laser spot diameter of 80 μm. 59

Figure 4.5. Reflection of SEM images of experimental results on simulation results with a laser power of 150 W 60

Figure 4.6. SEM image of AlSi10Mg powders used for the fabrication of samples 63

Figure 4.7. Optical micrographs of fabricated samples. Black regions are defects and the building direction is perpendicular to the plane. The optical micrographs are arranged from sample (1) to sample (19), respectively. Table 7.8 can be consulted for the production parameters of the samples. (Scale bar:200(μm)). 66

Figure 4.8. SEM image of: (a) hole defect in sample (1), (b) un-melted powder defect in samples (3) and (c), (d), (e) smooth microstructure in samples (10), (15) and (19). (Scale bar:10 μm). 70

Figure 4.9. Reflection of SEM images of experimental results on simulation results with a laser spot diameter of 140 μm. (Scale bar:10 μm). 71

Figure 4.10. Reflection of SEM images of experimental results on simulation results with a laser power of 110 W. (Scale bar:10 μm). 72

Figure 4.11. Tensile properties of SLM fabricated AlSi10Mg samples fabricated by the parameters given in Table 7.8. The blue-colored samples have a laser spot diameter of 140 μm with different laser powers and speeds, while the red-colored samples have a laser power of 110 W with different laser spot diameters and velocities 74

Figure 4.12. UTS and YS distribution of the samples versus the temperature including microstructure details. The blue-colored samples have a laser spot diameter of 140 μm with different laser powers and speeds, while the red-colored samples have a laser power of 110 W with different laser spot diameters and velocities (Scale bar:200 μm). 75

Figure 4.13. SEM images of the fracture surfaces of: (a) sample 2, (b) sample 5, (c) sample 12 and (d) sample 19. 76

Figure 5.1. Details of the improved model, including shielding gas, double layer powder and base plate. 80

Figure 5.2. 3-D molten track and melt pool temperature distributions of Ti6Al4V using 500 mm/s scanning velocity, 110 W laser power, and 85 μm laser spot diameter: (a) angular complete view, (b) top complete view, (c) symmetry view. 83

Figure **Page**

Figure 5.3. Simulation results and fitted curves of melt pool width for Ti6Al4V at different laser powers and a laser spot diameter of 85 μm; scanning velocity of a) 800 mm/s, b) 1100 mm/s, c) and d) 1400 mm/s 84

Figure 5.4. Simulation results and fitted curves of melt pool life time for Ti6Al4V at different laser powers and a laser spot diameter of 85 (μm); scanning velocity of a) 800 mm/s, b) 1100 mm/s, c) and d) 1400 mm/s 86

Figure 5.5. Simulation results and fitted curves of melt pool width for Ti6Al4V at different scanning velocities and a laser spot diameter of 85 μm; laser power of a) 80 W, b) 110 W, c) and d) 140 W 90

Figure 5.6. Simulation results and fitted curves of melt pool life time for Ti6Al4V at different scanning velocities and a laser spot diameter of 85 μm; laser power of a) 80 W, b) 110 W, c) and d) 140 W 91

Figure 5.7. 3-D molten track and melt pool temperature distributions of AlSi10Mg using 1100 mm⁄s scanning velocity, 180 W laser power, and 85 μm laser spot diameter: (a) angular complete view, (b) top complete view, (c) symmetry view 94

Figure 5.8. Simulation results and fitted curves of melt pool width for AlSi10Mg at different laser powers and a laser spot diameter of 85 μm; scanning velocity of a) 800 mm/s, b) 1100 mm/s, c) and d) 1400 mm/s 95

Figure 5.9. Simulation results and fitted curves of melt pool life time for AlSi10Mg at different laser powers and a laser spot diameter of 85 μm; scanning velocity of a) 800 mm/s, b) 1100 mm/s, c) and d) 1400 mm/s 96

Figure 5.10. Simulation results and fitted curves of melt pool width for AlSi10Mg at different scanning velocities and a laser spot diameter of 85 μm; laser power of a) 80 W, b) 110 W, c) and d) 140 W..... 99

Figure 5.11. Simulation results and fitted curves of melt pool life time for AlSi10Mg at different scanning velocities and a laser spot diameter of 85 μm; laser power of a) 80 W, b) 110 W, c) and d) 140 W..... 100

SYMBOLS AND ABBREVIATIONS

The symbols and abbreviations used in this study are presented below with their explanations.

Symbol	Description
C_p^*	Modified specific heat capacity
T	Temperature
u	Velocity
k	Thermal conductivity
A	Absorption coefficient
Q_{Laser}	Input laser energy source
Q_{Rad}	Radiated energy source
Q_{ev}	Evaporation heat loss
I_0	Intensity of the laser beam
b	Penetration distance of the laser beam
r	Distance from the point to the center of the beam
r_0	Radius of the laser beam
z	Vertical position of the powder
z_0	Position of the top of pow
P	Laser power
x, y	Positions of every irradiated point
α	Thermal diffusivity
ε	Emissivity of the powder
σ	Stefan-Boltzmann constant
T_0	Ambient temperature
H_{ev}	Latent heat of evaporation
$\dot{m}$	Evaporation rate
h	Mesh size
$p_v(T)$	Vapor pressure

Symbol	Description
$\mathbf{p_0}$	Ambient pressure
M	Molar mass
R	Ideal gas constant
$\mathbf{T_{ev}}$	Evaporation temperature
p	Pressure
I	Identity matrix
μ	Viscosity
$(.)^{\mathbf{T}}$	Transposed matrix
g	Gravity
F	Volume force
β	Coefficients of thermal expansion
$\mathbf{T_m}$	Melting temperature
κ	Curvature of interface
γ	Surface tension coefficient
n	Unit normal to the local surface
$\boldsymbol{\nabla_s}$	Surface gradient operator
δT	Melting interval
$\mathbf{A_1}$	Constant
$\mathbf{A_2}$	Constant
$\mathbf{f_l}$	Liquid fraction
$\mathbf{T_l}$	Liquidus temperature
$\mathbf{T_s}$	Solidus temperature
Π	Interface function
$\mathbf{Q_s}$	Source term
$\boldsymbol{\rho_{vap}}$	Vapor density
$\boldsymbol{\rho_{met}}$	Metal density
∅	Phase-field variable
γ	Mobility
λ	Mixing energy density
ε	Interface thickness parameter
ψ	Phase-field help variable

Symbol	Description
Q_s'	Source term
w	Melt pool width
$\mathbf{T_p}$	Preheat temperature

Abbreviations	Description
AM	Additive Manufacturing
SLM	Selective Laser Melting
SLE	Seçici Lazer Ergitme
ASTM	American Society for Testing and Materials
BTU	British Thermal Unit
EKTAM	Eklemeli İmalat Teknolojileri Uygulama ve Araştırma Merkezi
SEM	Scanning Electron Microscope
3-D	3 dimensional
UTS	Ultimate tensile strength
YS	Yiels stress

1. INTRODUCTION AND LITERATURE REVIEW

Additive Manufacturing (AM) technology builds parts layer by layer using powders (Powder Bed Additive Manufacturing) or wires (Wire Arc Additive Manufacturing) as a medium in 3-D printers. The powders or wires are exposed to a heat source and are melted. Referring to the manufacturing method, the heat source could be a laser, plasma or electron beam. It can be regarded as a revolution in fabrication technologies due to its superior advantages. AM technology leads the part directly from design to production. It reduces the need for conventional methods like casting and punching and enables building complex shaped parts directly. Fabrication with additive technology reduces the need of large amount of parts to be assembled together and allows to manufacture a unique part in an assembled form [1][2]. One of the most favorable techniques of additive manufacturing technology is Selective Laser Melting (SLM). In the SLM process, a layer of powder is spread on the build plate. The laser beam respecting the pattern which is designed and imported to the machine scans the powder layer, and the process repeats for every layer, and finally, the part will be ready for post-processes if needed [3][4][5].

The properties of the final product especially its metallurgical properties (microstructural features such as grain size and grain flow patterns) are affected by various parameters, among which the most important one is the formed temperature during the printing [6]. Subsequently, the forming temperature is affected by various factors such as laser power, scanning velocity, laser spot diameter, powder size, preheating, and laser beam properties. Also, keeping the temperature constant and preventing deviation of temperature from the specified value is necessary for having a homogeneous and uniform structure [7][8]. Currently, the suitable process parameters which lead to a desired microstructure are often extracted by the experimental methods which are high cost and time-consuming. A reliable model will enable us to extract the process parameters with very low cost and time. The suitable process parameters will result in a final product with minimum defects.

There have been studies and efforts made to model the SLM until today. Zhang et al. [9] investigated a thermal model to study the melt-pool of the alumina ceramic. They showed that the laser power and the scanning velocity affect the maximum temperature, lifetime, dimensions, and temperature gradients of the melt-pool. Bruna-Rosso et al. [10] developed a model to compute the thermal field in millimeter-scale together with the consequent melt-

pool dimension and temperature, and the model was validated with high-speed imaging. A two-dimensional Finite Difference model was developed by Foteinopoulos et al. [11] to calculate the temperature of a part in each time step and employed an algorithm for node birth and distance adaptation over time to reduce the computational time.

Leitz et al. [12] studied the effect of the laser power and laser energy density on the melt-pool width by developing a multiphysics model. They figured out that the melt-pool dimensions are wider in steel compared to the molybdenum because of the thermal conductivity difference in materials. Artinov et al. [13] developed a multiphysics model to calculate a reliable equivalent heat source and to predict the thermal behavior during the laser welding using a moving mesh and weak constraints. Bayat et al. [14] investigated a multiphysics model for laser-based powder bed fusion to study the keyhole phenomena in the melting of Ti6Al4V and confirmed their work doing an X-CT analysis. Courtois et al. [15] simulated the SLM and keyhole formation with a new approach. They took the reflection of the laser beam in the keyhole into account. Finally, they compared the melt-pool shapes resulting from modeling with experimental micrographs. Mukherjee et al. [16] developed a 3-D , transient, heat transfer, and fluid flow model to calculate temperature and velocity fields, build shape and size, cooling rates, and the solidifica-tion parameters during the PBF process. Shi et al. [17] developed a single track method for parameter optimization of Ti47Al2Cr2Nb powder in SLM. Using the single track scan results, they developed a parameter window and optimized the fabrication parameters for Ti47Al2Cr2Nb powder. They also built regression models to predict the geometric characteristics of single traces. Liu et al. [18] developed a thermal 3-D finite element model utilizing to simulate a single track scanning of AlSi10Mg metal powder. They established a high accurate transient model that predicts the thermal gradients and the microstructure of the part. Liu et al. [19] investigated a thermal 3-D finite element model to show the efficiency of the multi-laser scanning during the SLM of AlSi10Mg. They showed the reliability of the model employing SLM-fabricated samples. Han et al. [20] developed a numerical thermal model to explore the microstructural-mechanical properties of as-fabricated $Al - Al_2O_3$ nanocomposite in SLM. They determined an optical laser energy density and laser scanning velocity that provided 99.49% relative density in part. Liu et al. [21] investigated a thermal model to study the effect of the track length and track number on the evolution of the thermal variables and molten pool characteristics of SLM of aluminum alloy (AlSi10Mg). They did multi-track SLM fabrication and employed 3D imaging of multi-track to verify their model. Li & Gu

[22] established a thermal 3-D finite element model to investigate the effect of the laser power and scanning velocity on the thermal behavior of AlSi10Mg during the SLM process. Du et al. [23] developed a thermal model for predicting the temperature field of the AlSi10Mg molten pool in the SLM process. They explored the influence of the laser power and scanning velocity on the thermal behavior of the SLM process. They performed single-track productions to confirm the model.

Nonetheless, the thermal study of the SLM process will not be able to give us a realistic temperature, as it does not contribute the convective transport of heat in the calculations. In the absence of fluid flow physics, the driving forces of the fluid will not include the modeling and it is a big loss in the realistic approach to the SLM process. Mukherjee et al. [24] developed a 3D transient heat transfer and fluid flow model to calculate the effect of various parameters including, temperature and velocity fields, fusion zone shape and size and etc. to lack of fusion defect and distortion, on metallurgical quality of Stainless Steel 316L, Ti6Al4V, IN 718 and AlSi10Mg alloys. They carried out multi-layer and multi-hatch experiments to show the model reliability. Pei et al. [25] studied the thermodynamic behaviors of the molten pool during SLM of AlSi10Mg powder. They established a 3D model and simulated randomly distributed powders employing the discrete element method. They studied the effects of laser scanning velocity, laser power, and hatch spacing.
Although various studies were carried out on the energy source-powder interactions, the existing models mainly focus on the model development by using a given parameter set. Therefore, there is still a large gap in obtaining process parameters for Stainless Steel 316L and AlSi10Mg metal powders with a reliable model and investigating the mathematical relationships between them.

On the other hand, there are more studies on process parameters to date. Cherry et al. [26] studied the effect of the process parameters on the porosity and microstructure of the additively manufactured Stainless Steel 316L. Their study was an experimental study and presented the balling, hardness, surface roughness and porosity amounts in relation to laser energy density. Liverani et al. [27] tried to present a correlation between the process parameters and the resulting microstructure and mechanical properties of SLM Stainless Steel 316L specimens. The results showed that the effects of hatch space and building direction did not have a significant effect on the density of the produced part, whereas the laser power had a strong effect on it. Kempen et al. [28] presented a process parameter

window for AlSi10Mg as a result od an experimental single track study. Their process window describes the effect of the scanning velocity and laser power changes on each other. They obtained optimal density and surface quality results for the 3-D fabricated AlSiMg parts. Trevisan et al. [29] did a comprehensive study on the SLM fabrication of the AlSi10Mg alloy. They examined the effect of the main process varialbles on the microstructure of the final part. They showed that employing the standard heat treatment on the fabricated samples of their study do not lead to the usual results. They also notice that SLM fabricated parts need to be treated differently from bulk alloy parts. Kasperovich et al. [30] performed a systematic optimization strategy to obtain minimum porosity volume fraction in the TiAl6V4 SLM fabricated parts. They conclude that the porosity of the parts can be reduced to <0.05 vol% by optimizing the process parameters. Also, they observed two classes of porosities at insufficient and excessive energy inputs: circular pores with a diameter of >50 μm at excessive energy regimes probably resulting from keyhole formation and elongated, narrow crack-like defects as a result of lack of fusion with a length of >100 μm. Majumdar et al. [31] studied the effect of the laser power and scanning speed on the SLM fabricated TiAl6V4 parts. More melt-pool depth and increase in remelting/recooling cycles of every layer is a result of the laser power increase. Also, an increase in scanning speed, besides the increasing Plateau-Rayleigh instabilities and a higher likelihood of balling, results in an elongated melt pool. They showed that in the fabrication of the TiAl6V4, a combination of the high laser scan speed (> 1000 mm/s) with low laser power (< 120 W) will give us poor solidification of the powders due to insufficient supply of thermal energy. On the other hand, a low scanning speed and high laser power will result in an excessive supply of energy and consequently keyhole porosities.

As it seems, production defects play a very important role in the additive manufacturing. In other words, quality of the final product is very important. Controlling the fabrication quality of SLM process instantly during the process is an important study subject. Rezaeifar and Elbestawi [32] utilized a thermal camera and an IR-transmissive window as monitoring system to correlate the temperature and porosity types. They presented a safe thermal zone for fabrication and used a PID controller to keep the fabrication temperature in the safe thermal zone. Bartlett et al. [33] tried to detect the lack of fusion and keyhole defects employing a long-wave infrared camera (LWIR). For recognition of the lack of fusion defects, they tried to obtain the temperature distribution map of each layer. Their effort had an 85% accuracy for detecting the lack of fusion defects but was not sufficient to detect the

keyhole defects. A pyrometer showing the melt pool temperature was employed by Forien et al. [34] to predict the keyhole defects. They showed that the probability of the occurring of the keyhole defect increases as the temperature exceeds a threshold. Coeck et al. [35] used two photodiodes as monitoring system to examine the lack of fusion defects with a 90% acuuracy for defects with a minimum 160 μm diameter. Clijsters et al. [36] performed an in situ monitoring system for selective laser melting to handle the process quality simoltaniously. They presented two major deveplopment in their study. One of them was designing a complete optical sensor setup. The setup consists two optical sensors connected to a field-programmable gate array (FPGA) which communicates directly with the machine control unit. Another development was the translation and visulisation of the measured values by the sensors using an analysis system. “Mapping algorithm” was used for visulisation which transfers the measurements from a time-domain into a position-domain representation. Rodriguez et al. [37] integrated a thermal imaging system employing an infrared camera. For catching a certain accuracy of the infrared camera they provided the TiAl6V4 powders’ emissivity, reflected temperature, and optics transmission. The system resulted in a high level of feedback to identify absolute thermal non-uniformity on the fabricated parts’ surface by capturing infrared images.

As discussed so far, there are at least three key matters in the additive manufacturing process study and implication as Modeling and Simulation, Process Parameters for Fabrication and Controlling the Melt Pool (Quality of the Fabrication).

The listed works do not in general suppose a certain process parameter window and do not experience a sample part experimental task. Almost all of their experimental confirmation is done on single layer scanning, not sample part fabrication, which includes the previous and next layer’s effect. As regards, these models are presented only as developed models, and there is a significant gap in the development of various process parameters and the relationships between them and their application for sustainable performance during printing. That is to say, what still missing, are the various process parameter sets and their mutual relationships between them. This has been obtained via a reliable model that presents us the temperature values considering the melt process's effective aspects.

On the other hand, another important issue is controlling the quality of the SLM process and consequently controlling the melt pool during the fabrication process in SLM. Instantaneous

monitoring of the melt pool and fabrication surface is important to simultaneously respond to fabrication process parameters based on the defects encountered or the geometry of the particular region of the part. In addition to the general studies, excessive and insufficient definitions of the process parameters, the parameters to be used in different regions of the one part should be selected according to the shape of the part in that zone. For example, parameters to be used in thin and narrow zones should not be the same as the parameters to be used in thick and wide zones.

All these mentioned issues make it inevitable to develop the ability to interfere with parameters during production. Although there have been extensive efforts to find out admissible process parameters, either through simulations or conducting experiments, in the SLM process, there is still a need to formulate input and output relationships so that a Transfer Function representation could be defined for a possible feedback control mechanism. This thesis is an attempt to clarify the input and output relationship in AM process.

The thesis presents a simulation approach to extract a wide range of process parameters for SLM fabrication with Stainless Steel 316L, AlSi10Mg and TiAl6V4 alloy metal powders. A 3-D multiphysics model, that time dependently solves equations of heat transfer, conservation of mass, Navier-Stokes and Cahn-Hilliard by using temperature dependent material properties, was developed. The model calculates the melt pool temperature and dimensions employing the driving forces and a volumetric heat source. The proposed mathematical approach was validated by testing the melting and mechanical conditions of fabricated samples. The presented approach provides mathematical relationships between the process parameters and the temperature they form. Mathematical relationships are important for a possible feedback control design to control the melt pool temperature. Controlling the temperature using mathematical relationships is particularly important because it results in a final product with homogeneous and minimal defective microstructure and optimum mechanical properties. These properties are achievable by keeping the melt pool temperature in an allowable range, which could prevent deviation of the formed temperature during fabrication. Therefore, by controlling the melt pool temperature during the process, the microstructure and mechanical properties of the final part could be controlled and a reliable final part could be obtained.

Mathematical relationships are extracted from the simulation results of the SLM process. These mathematical relationships will be used in the control process of the melt pool. For designing a controller, we need to provide the base materials which, the most important of them is the transfer function. Extracted mathematical relationships are transfer functions we need.

Reviewed literature studies show that a control system is the essential need of the 3-D printers but there is no notable success and progress in the field. There is a gap in the controller design for the 3-D printers and the thesis tries to take notable steps in the process of developing the controller systems for the 3-D printers. Figure 1.1 shows the schematic illustration of the block diagram of the process control system that needed to be developed. The thesis study was carried out on Stainless Steel 316L, AlSi10Mg and Ti6Al4V metal powders. This is because these alloys are among the most used powders in industries such as aerospace and medicine. In addition, the available research on these powders in the literature allows us to take a comparative look at the results. The special properties of austenitic steel alloys, aluminium alloy and titanium alloys locates them among the most popular group of alloy. The contribution of various alloy elements gives them a very important and notable feature in the laser powder bed fusion. The weldability of the Stainless Steel 316L and its usefulness allocate special space for it in additive manufacturing. Stainless Steel 316L, as austenitic steel, stands out with its perfect resistance to oxidation at high temperatures while maintaining a low coefficient of thermal expansion, creep resistance, resistance to fatigue and heat resistance [38][39][40][41]. Aluminum alloys have a special position because of their lightweight. In return, due to its high thermal conductivity and oxidation, it is a challenging alloy in fabrication. Conductivity has a powerful and direct influence on thermal behavior and melting phenomena [42]. TiAl6V4 alloy has gained a special place in the field of medicine as well as its special position in the aerospace and defense industry. This alloy owes high corrosion resistance and high specific strength [31][43][44].

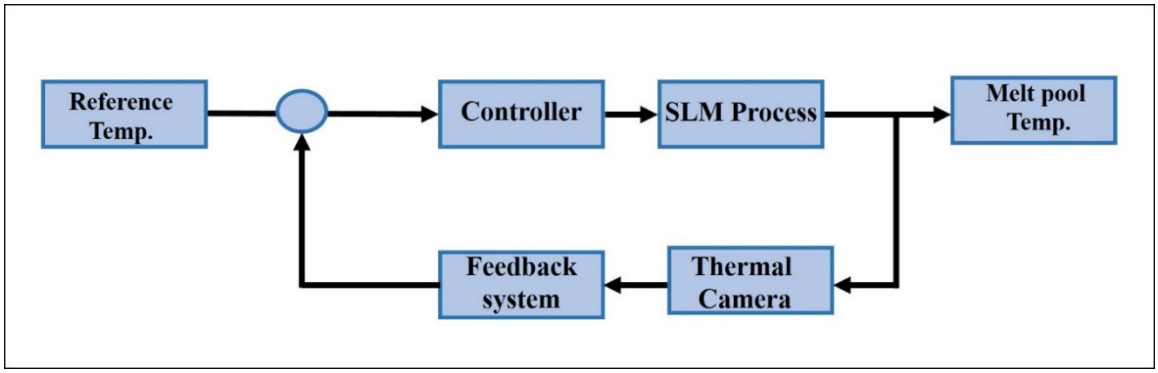


Figure 1.1. The schematic illustration of the block diagram of the process control system.

The structure of the thesis is as follows; Mathematical Modelling of Selecetive Laser Melting is given in Chapter 2, which typically describes the governing equations during the SLM process. Simulation Results of the SLM Process are submitted in Chapter 3, which the effect of the process parameters on the melt pool temperature (process parameter windows) and mathematical relationships between them are presented. Chapter 4, Experimental Validation, describes microstructure and mechanical experiments to conform the validity of the simulatlons. In Chapter 5, An Improved Mathematical Model with Phase Field Physics, the developed model in Chapter 2 is improved by adding a new physics as Phase Field physics. Here the effect of the process parameters on the melt pool width and melt pool life is presented. Also, mathematical relationships between them is shown. Chapter 6 includes the Conclusions of the thesis.

The purposes of this study are twofold; to investigate the mathematical model of selective laser melting additive manufacturing process and to simulate the SLM process leading to developing process parameters for Stainless Steel 316L, AlSi10Mg, and TiAl6V4. Then mathematical relationships of the process are established between process parameters such that melt pool temperature and melt pool width could be formulated. Indeed, these mathematical relationships will compose the basic materials for designing a control system to control the melt pool instantaneously.

2. MATHEMATICAL MODELING OF SLM

"A simulation is the imitation of the operation of a real-world process or system over time." [45]. Simulation is used in various fields of science to monitor functioning. Simulation enables us to understand the details of the simulated phenomena and study the process in detail. To simulate a process, it is needed to prepare the model of the process. The model is the key tool for presenting the properties of the system during the occurrence of phenomena. Mathematical model presents the process, employing the equations for different physics. The software simulates the phenomena using the mathematical model and solves the relevant equations throughout the problem domain.

2.1. Selective Laser Melting (SLM)

Selective Laser Melting (SLM) is a widely used and favorable AM method. Production starts after preliminary preparations and importing the appropriate process parameters to the 3-D printer. Throughout the process, the appropriate amount of powder is spread over the fabrication plate with a roller as shown in Figure 2.1. The laser beam selectively scans the powders according to the pattern taken to the machine as a CAD file. When the machine finishes the pattern scanning of the current layer, to distribute the powder and form the new layer, it moves the powder delivery piston up one step/layer and the fabrication piston moves one step/layer down. This process continues until the last layer is scanned and the process is terminated [46]. The interaction zone includes three regions. These are respectively the powder region, melting-evaporation region and solidification region. Contrary to the conventional method, the SLM includes complex physics and therefore needs a multiphysics approach to understand. Process parameters such as laser power, laser spot diameter, and scanning velocity must be appropriate to obtain a suitable final product. The fabrication chamber is filled with a suitable gas depending on the powder material.

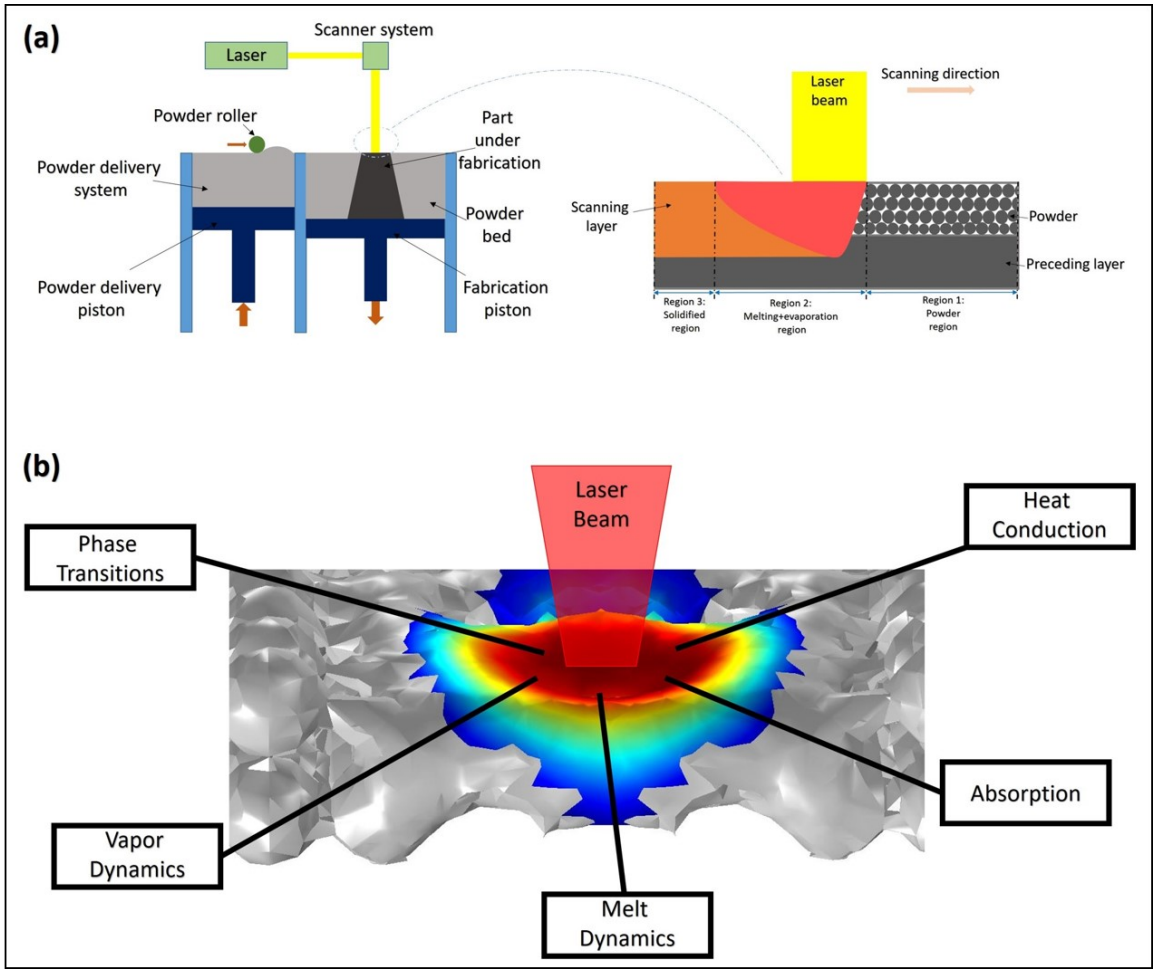


Figure 2.1. (a) The schematic illustration of the SLM process; (b) The prepotent physical phenomena during the selective laser melting.

2.2. Governing Equations of Mathematical Modeling

The mathematical model has been developed to simulate the interaction of laser beam and powder. As stated earlier, every simulation needs to be modeled with mathematical relationships. The more detailed physics of phenomena are included in the model; the more accurate results will be obtained. The inclusion of the heat equation alone in modeling the laser beam-material interaction will not give us accurate results because the physics of heat does not include convection driving forces. Therefore, the presence of the momentum equations (Navier-Stokes and conservation of mass) are necessary for this modeling to include the convection driving forces.

Neither heat equation and momentum equation solve the topology changes of the melted powders and do not present the fluid flow during the melting process. A third physics must

be added to the mathematical model in order to address this deficiency and to solve the topology changes during the melting process. This third physics is phase-field physics, which solves the Cahn-Hilliard equations.

2.2.1 Heat Transfer Equation

In the study of heat, one can imagine a physical model in which heat is considered a fluid in matter, free to flow from one location to another. The amount of fluid available is measured in some units such as calories (cal) or BTU (British Thermal Unit). Proof of its existence in matter is the temperature of the substance, the more heat presents the higher the temperature and it is assumed that it flows from places of higher temperature to places of lower temperature. The temperature can be measured straight with a thermometer; the amount of heat available is determined indirectly, one unit heat is the amount needed to raise one unit water temperature by one unit temperature [47].

The heat transfer equation (energy equation) describes the temperature and temperature gradient and is solved numerically during the simulation of the SLM process:

$$\rho C_p^* \frac{\partial T}{\partial t} + \rho C_p^* u.\nabla T = \nabla.(k\nabla T) + AQ_{Laser} + Q_{Rad} + Q_{ev} \quad (1)$$

where ρ, C_p^*, T, t, u, k, A, Q_{Laser}, Q_{Rad}, and Q_{ev} are density (kg/m^3), modified specific heat capacity ($J/kg.K$), temperature (K), time (s), velocity (m/s), thermal conductivity ($W/(m.K)$), absorption coefficient (-), input laser energy source (W/m^3), radiated energy source (W/m^2) and evaporation heat loss (W/m^3) respectively. The laser beam is modeled as a moving Gaussian distributed heat source on the powders. Shadowing effect, multi-reflection, and beam angle effect on the absorption of the laser are neglected [48].

Proper heat source model will present a more realistic approach to the simulation because it determines the generated energy of the laser power, leads to temperature formed in the melt pool and affects the microstructure and mechanical properties of the final product. Heat source models are generally introduced in two dimensions and three dimensions. Two-dimensional model includes the distribution in two axes, however, in reality the laser beam

penetrates in the third direction as well. Zhang et al. [49] extensively studied the background of heat transfer modeling used in LPBF, as presente in Figure 3.2.

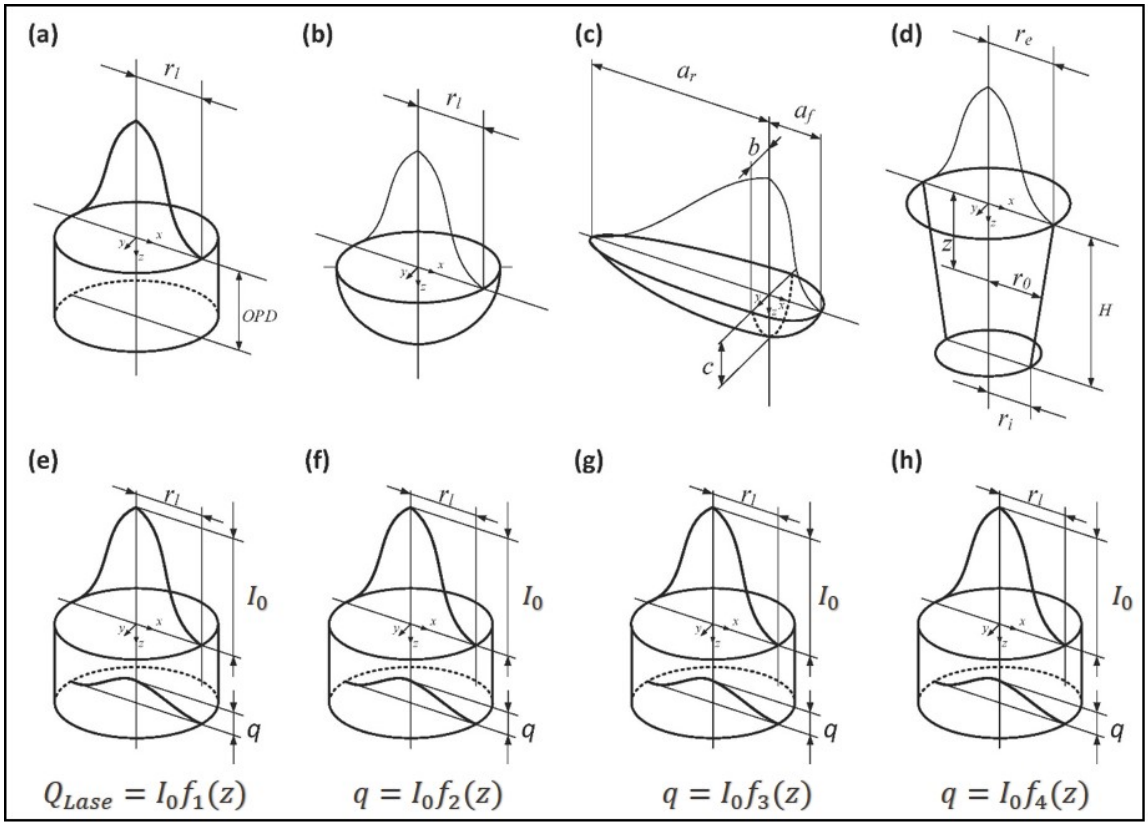


Figure 2.2. The representation of the heat source models, (a) cylindrical shape; (b) semi-spherical shape; (c) semi-ellipsoidal shape; (d) conical shape, (e) radiation transfer method; (f) ray-tracing method; (g) linearly decaying method; (h) exponentially decaying method. Here r_l is the radius of the laser beam; a, b, c are semi-axes parallel to the coordinate axes of x, y, z; a_f and a_r are the semi-axes of the front and rear ellipsoids; r_e and r_i are the radius at the top and bottom [49].

In order to take into account the penetration of the laser beam [18], a cylindrical shape Gaussian distribution volumetric heat source belonging to the absorptivity profile group has been developed [49]:

$$Q_{Laser} = \frac{I_0}{b} \exp(\frac{-2r^2}{r_0})\exp(\frac{z-z_0}{b}) \quad (2)$$

$$I_0 = \frac{2P}{\pi {r_0}^2} \quad (3)$$

where I_0, b, r, r_0, z, and z_0 are the intensity of the laser beam at the beam axis (W/m^2), penetration distance of the laser beam (m), distance from the point to the center of the beam (m), the radius of the laser beam (m), the vertical position of the powder (m), the position of the top of powder (m) and P denotes the laser power (W). The vertical position of the powder, $r(m)$, shows the $x(m)$ and $y(m)$ positions of every irradiated point at time $t(s)$ ($r = \sqrt{x^2 + y^2}$) through scanning path with a scanning velocity of $v_x(m/s)$ that is equal to $v_x = x/t$ [9].

The radiative heat loss is illustrated using Stefan- Boltzmann law, which defines the power radiated from a black body in terms of its temperature [50], that is nonlinear and is indicated by:

$$Q_{Rad} = -\varepsilon\sigma\,(T^4 - T_0^4) \tag{4}$$

where ε, σ, and T_0 are the emissivity of the powder (-), Stefan-Boltzmann constant for radiation ($5.67 \times 10^{-8}(W/m^2.K^4)$), and ambient temperature (K) respectively. Also, evaporation heat loss is introduced, that is determined through the following expression [51]:

$$Q_{ev} = -\frac{H_{ev}m^{\bullet}}{h} \tag{5}$$

where H_{ev}, $m^{\bullet}$, and h are latent heat of evaporation (J/kg), evaporation rate ($1/s$), and mesh size (m) respectively. Referring to the Hertz-Knudsen equation, the evaporation rate is determined as [52]:

$$m^{\bullet} = (p_v(T) - p_0)\sqrt{\frac{M}{2\pi RT}} \tag{6}$$

where $p_v(T)$, p_0, M, and R are vapor pressure at the temperature of T (N/m^2), ambient pressure (N/m^2), molar mass (kg/mol), and ideal gas constant ($J/mol.K$) respectively. The vapor pressure at the temperature of T can be determined by [52]:

$$p_v(T) = p_0 e^{\frac{H_{ev}M}{RT_{ev}}(1-\frac{T_{ev}}{T})} \tag{7}$$

where T_{ev} is the evaporation temperature (K).

2.2.2 Navier-Stokes and Conservation of Mass Equations

Navier-Stokes equations designate the relation of the velocity, pressure, temperature and density in a moving fluid. The equations were independently derived in the early 1800s by G.G. Stokes in England and M. Navier in France [53]. The equations include the viscosity effect on the flow and are inspired by Euler's Equations. It is usually employed in three spatial dimensions and time dependently.
Also, the principle of conservation of mass designates that in the lack of mass sources and sinks, a region will conserve its mass locally.

The transition of the powder from the solid phase to the liquid phase occurs by absorbing the energy of the laser beam. The fluid flow physics solves the conservation of mass and Navier-Stokes equations. The equations are:

$$\nabla . u = 0 \tag{8}$$

$$\rho\left(\frac{\partial u}{\partial t} + u(\nabla . u)\right) = \nabla . [-pI + \mu(\nabla u + (\nabla u)^T)] + \rho g + F \tag{9}$$

where p, I, μ, $(.)^T$, g, and F are pressure (N/m^2), identity matrix, viscosity $(Pa.s)$, transposed matrix, gravity (m/s^2) and volume force (N/m^3), respectively [13].

The volume force contains four terms [49] involved in buoyancy force (first term), Carman-Kozeny equation (second term) [15], surface tension force (third term) and Marangoni effect (fourth term) as:

$$F = \rho g \beta (T - T_m) - A_1\left(\frac{(1-f_l)^2}{{f_l}^3 + A_2}\right) + \kappa \gamma n + \nabla_s \gamma \tag{10}$$

where β, T_m, κ, γ ,n and ∇_s are coefficients of thermal expansion $(1/K)$, melting temperature (K), curvature of interface, surface tension coefficient (N/m), unit normal to

the local surface and surface gradient operator, respectively. The buoyancy force is the deviation of the density during changing temperature.

Carman-Kozeny equation describes mushy zone. In this zone, which includes a mixture of solid and liquid metal, the transition from the solid phase to the liquid phase during a temperature interval which is named melting interval (δT) occurs. This mixed region is named mushy zone [54] . A_1 is a huge constant that is defined to fix the powders under melting temperature as a solid phase, and A_2 is a small constant to satisfy the convergence during the simulation and it does not allow the denominator to be zero. As the powder is melted, the damping force vanishes. In other words, it acts just in the mushy and solid-state of the powders. The force removes linearly respecting f_l , the liquid fraction, which changes linearly with respect to the solidus temperature (T_s) and liquidus temperature (T_l),

$$f_l = \begin{cases} 0 & if\ T < T_s \\ \frac{T-T_s}{T_l-T_s} & if \quad T_s \le T \le T_l \\ 1 & if\ T > T_l \end{cases} \tag{11}$$

As the temperature decreases and solidification begins, the damping force appears and acts on the solid phase.

The melt pool surface refers to be a free surface defined as an open boundary. The Marangoni effect applies a tangential force while surface tension exerts a normal force on the surface. The molten flow during the simulations was assumed laminar and incompressible.

2.3. Multiphysics Model

The multiphysics model as described in Section 3.2 was used to simulate the metal powder–laser interaction. A 3-D model was designed, and a time-dependent study was used. Considering the powder size distribution in the datasheet of the Concept Laser Company and the practical layer thickness during the manufacturing, the average diameter of powders was considered 40 μm (layer thickness). Then powders were modeled as homogeneous 40 μm spheres, which were assumed to be homogeneously distributed on the built plate.

Simulations were done in one path of 720 μm distance and the model was formulated symmetrically to reduce the calculation time in the simulations.

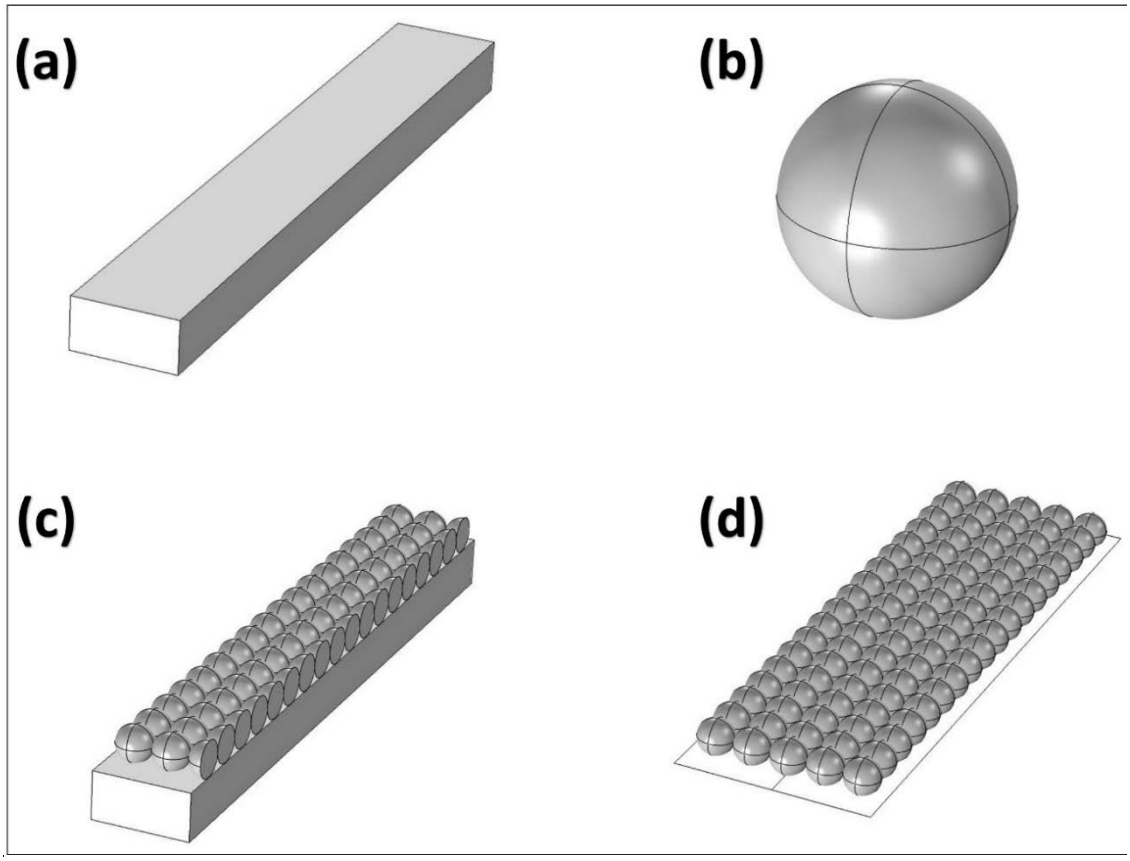


Figure 2.3. Description of the models, (a) powder bed; (b) ideal powder with a diameter of 40 μm; (c) symmetry view of the powders lined up on the powder bed; (d) complete view of the powders lined up on the powder bed.

Simulation was done by coupling heat transfer and laminar flow physics of the commercial finite element software COMSOL Multiphysics 5.4. A free tetrahedral mesh was used for all domains, and a mesh size of 5 μm was used. The volumetric heat source, radiative, and evaporation heat loss heat boundaries were employed, and incompressible flow patterns with gravity force, buoyancy force, Carman–Kozeny force, surface tension force, and Marangoni effect were applied. Computation times were found to be in a range of 6–15 h for a scanning track of 720 μm on two cores of a dual CPU Intel Xeon Gold 6230 CPU workstation.

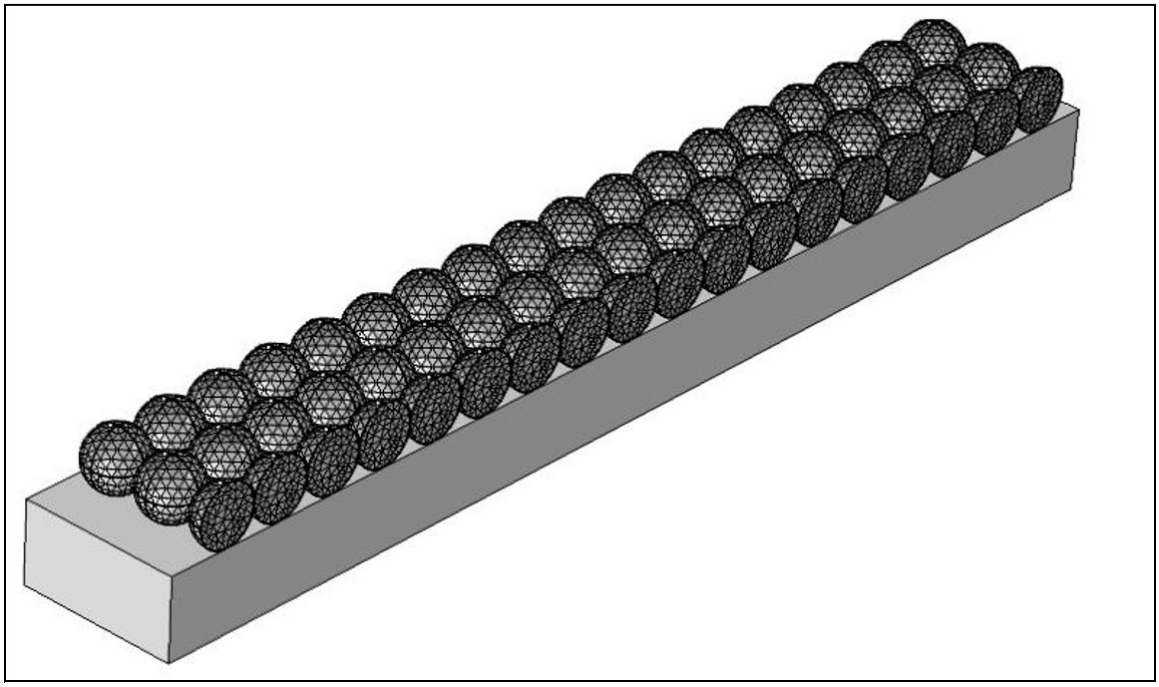


Figure 2.4. Free Tetrahedral meshed powders.

Convergence is a noteworthy point during simulations. There are different solvers to solve equations numerically in software, such as the fully coupled and segregated solvers. In our simulations a segregated solver was used (a tolerance factor of 0.005) to solve the mentioned three equations applying the Newton–Raphson iteration (a minimum damping factor of 10^{-6}) until the solution was converged. The software, in every time step, first calculates the temperature in heat transfer physics. Then, it passes to the laminar flow physic and there, employing the achieved temperature as well, calculates the velocity and pressure. If it converged, the computation continues to the next time step, otherwise, it repeats the cycle until the convergence obtained.

2.4. Experimental Approach

In order to confirm the simulation results, experimental studies were performed at the Additive Manufacturing Technology Application and Research Center (EKTAM) of Gazi University. Experiments were done using a 3D printer of the Concept Laser-M2 CUSING model. The machine has a continuous wave Ipg Ylr 400 ac y14 ytterbium fiber laser (λ=1070 nm) with a nominal maximum laser power of 400 W. Fabrication was done in a controlled build chamber under a nitrogen gas for Stainless Steel 316L and argon for AlSi10Mg, which

contained a maximum 0.4% O_2. The base plate of the machine is steel for Stainless Steel 316L and aluminium for AlSi10Mg with nominal dimensions of 245 × 245 × 25 mm (length × width × hight), respectively. The preparation process was carried out on the plate and it was made ready for production. The surface was ground with the FOREMAN ST4080A Surface Grinder to have a plate with minimum roughness and maximum flatness. Next, the plate was sandblasted to prevent reflection.

For Stainless Steel 316L, sets of parameters were selected from the results of the simulations, which are shown in later chapters. Using these parameters, a hatch space of 115 μm and powder layer of 25 μm, samples were fabricated, and their microstructures were examined to illustrate the conformity of the simulation results. The layer thickness was selected as 40 μm. In the fabrication process, the fabrication piston moved down 25 μm in each layer to spread the powder for the upcoming layer. However, since the melted preview layer's surface was a rough surface and included concavities, as the spread powder fills them too, the powder layer that should be scanned after powder delivery was therefore 40 μm. That was why the powder layer in the simulations was assumed to be 40 μm. Every sample was fabricated in 100 layers using the island scanning strategy. The final dimensions of the Stainless Steel 316L samples were nominally 80 × 10 × 2 mm (length × width × hight), respectively. The produced samples were prepared under slice cutting to be ready for the microstructure inspection. Cutting was done with diamond micron wire at a very slow speed with water cooling to avoid affecting the microstructure. The method of cutting and preparing samples for microstructure inspection is shown in detail in Figure 2.5. The cross-section of the cut samples was polished using different metallographic sandpapers and etched with a proper reagent (55%HCl,20%NHO_3 and 25% methanol [55]) for the microstructure inspection. DMi8 Leica Microsystems microscope was employed for the micrograph imaging and a JSM-6060LV JEOL microscope was used for scanning electron microscopy (SEM).

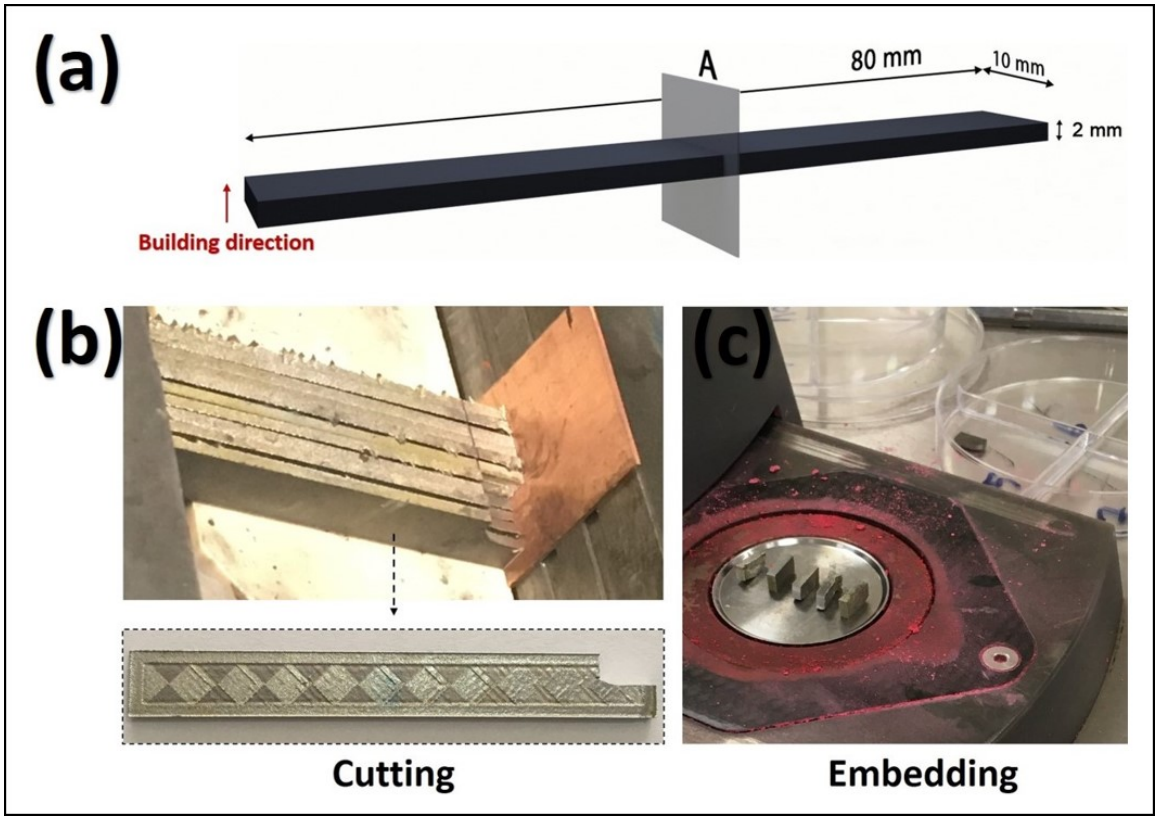


Figure 2.5. a) Pattern and dimensions of the fabricated samples of Stainless Steel 316L. Samples were cut in line with the plane (A) to examine the microstructure. b) Cutting and c) embedding the samples for microstructure inspection.

For AlSi10Mg, two sets of SLM test samples were fabricated to validate the model and simulation results, each for microstructure and tensile analyses. The experimental works were carried out at the Additive Manufacturing Technology Application and Research Center (EKTAM) of Gazi University. Specimens were fabricated by a 3-D printer of Concept Laser-M2 CUSING model. The machine has a nominal maximum laser power of 400(W) and a continuous wave Ipg Ylr 400 ac y14 ytterbium fiber laser (λ=1070 nm). The build chamber is controlled under a nitrogen gas with a maximum %0.4 O_2. The gas atomized AlSi10Mg powders of Concept Laser company were used in fabrication. Sets of process parameters were selected from the simulated parameters and used for the production of two sets of samples using continuous scanning strategy with a hatch space of 112 μm. Fabrication was carried out horizontally in order to obtain optimized microstructural and mechanical properties [56]. One set, the samples for microstructure analyses, were fabricated in one hundred layers in nominal dimensions of 2.5 ×10 ×50 mm (length × width × hight), respectively. Another set, tensile analyses (Yield Stress, Ultimate Tensile Strength and Elongation) samples, were produced bar-shaped in four hundred layers of 10 mm diameter

and 80 mm length. Similar to the previous samples, these were also fabricated using a continuous scanning strategy. The AlSi10Mg bars were machined to produce rod tension test specimens following ASTM standard E8/E8M – 13a [57]. Subsequently, the microstructure of the samples was investigated with a DMi8 Leica Microsystems optic microscope and JSM-6060LV JEOL electron microscope. Samples were etched with a proper reagent (10% H_2SO_4 and 5% HF [58]) for the microstructure examination. Detailed illustration of fabricated samples and slicing is presented in Figures 2.6 and 2.7.

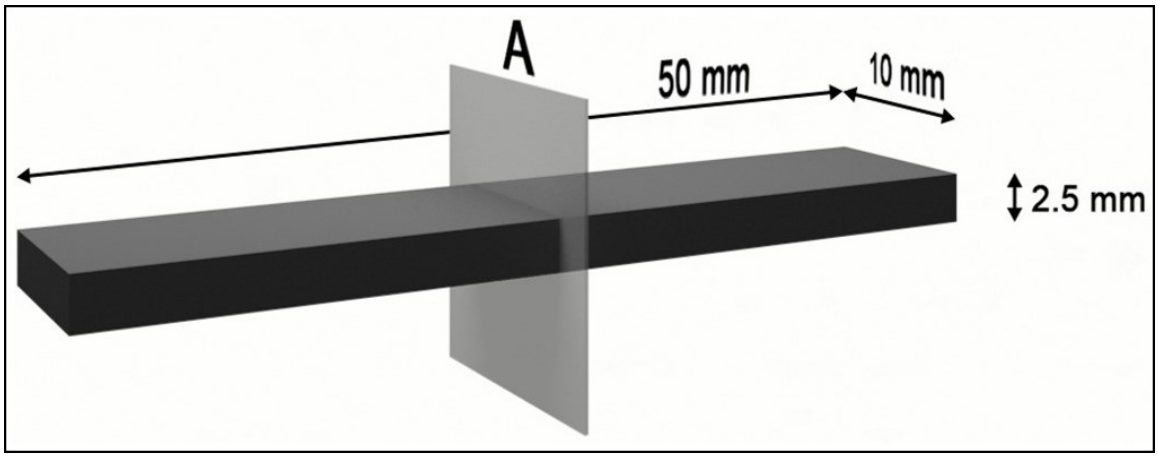


Figure 2.6. Design and nominal dimensions of fabricated samples for microstructure characterizations. For analysis, samples were cut in line with the (A) plane.

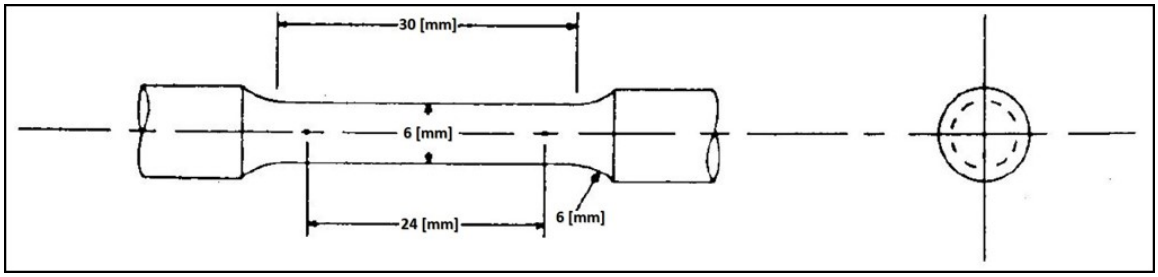


Figure 2.7. Schematic of the tensile test specimens following ASTM standard E8/E8M – 13a.

3. SIMULATION RESULTS OF THE SLM PROCESS

3.1 Stainless Steel 316L

The simulation model presents coupling of two types of physics, and the results are shown in Figures 3.1 and 3.2. An SLM process was simulated and melting during moving laser heat source was presented. The simulations were done in symmetry mode to reduce the calculations and process time. Basically, Figure 3.1 illustrates the temperature values of a powder layer for a given set of laser power, laser spot diameter, and scanning velocity. The symmetry view (Figure 3.1a) shows the laser beam penetration in powder, and the complete view (Figure 3.1b) shows a complete scanned row of powders. Isosurface temperature view (Figure 3.1c) and the phase change is depicted (Figure 3.2). Figure 3.2 is an illustration of the melted area. The area with the value of one is the liquid phase, while the zero value area belongs to the solid phase. Indeed, the area with the value of one is the melt-pool area. The thin border area, which has a value between one and zero, is the mushy region as illustrated earlier.

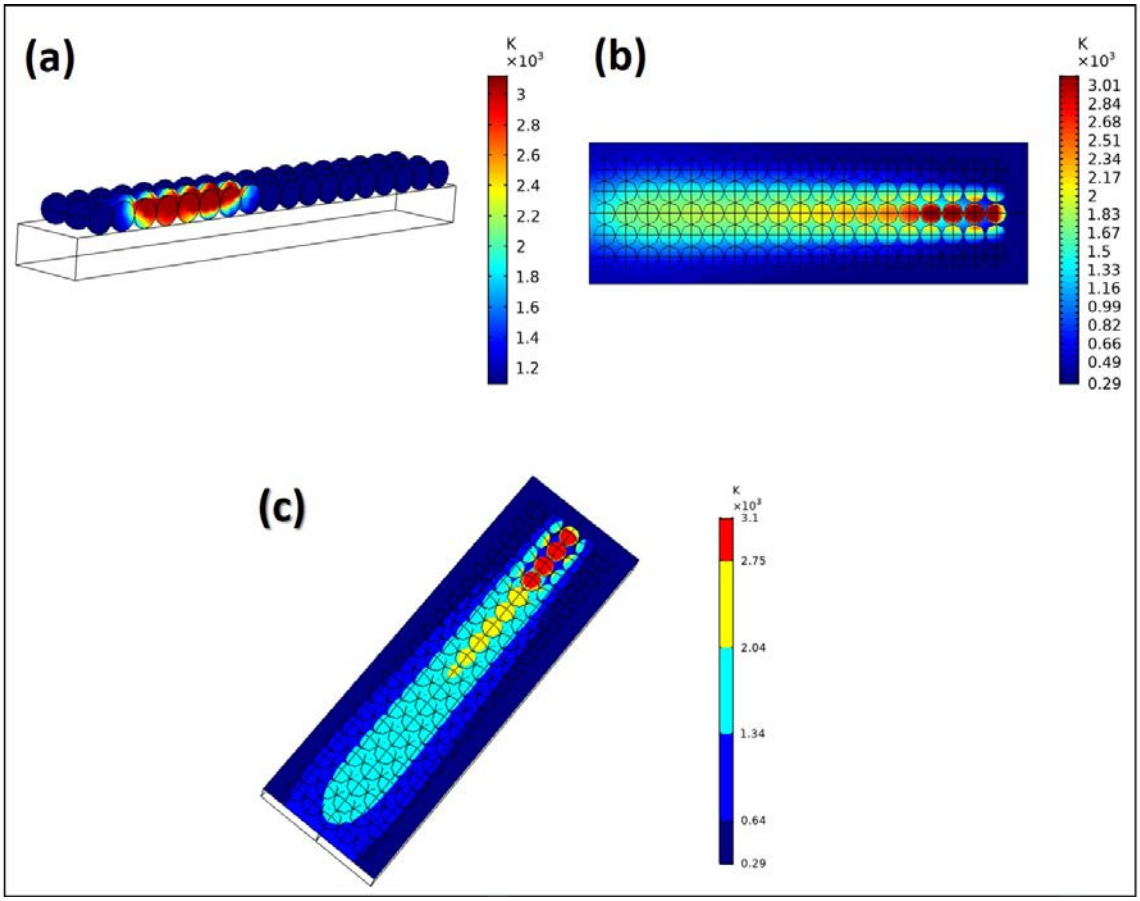


Figure 3.1. 3-D temperature distributions using 900 (mm)⁄s scanning velocity, 150 W laser power, and 50 μm laser spot diameter: (a) symmetry view, (b) complete view, (c) and isosurface view showing the zones with various temperature values at the moment.

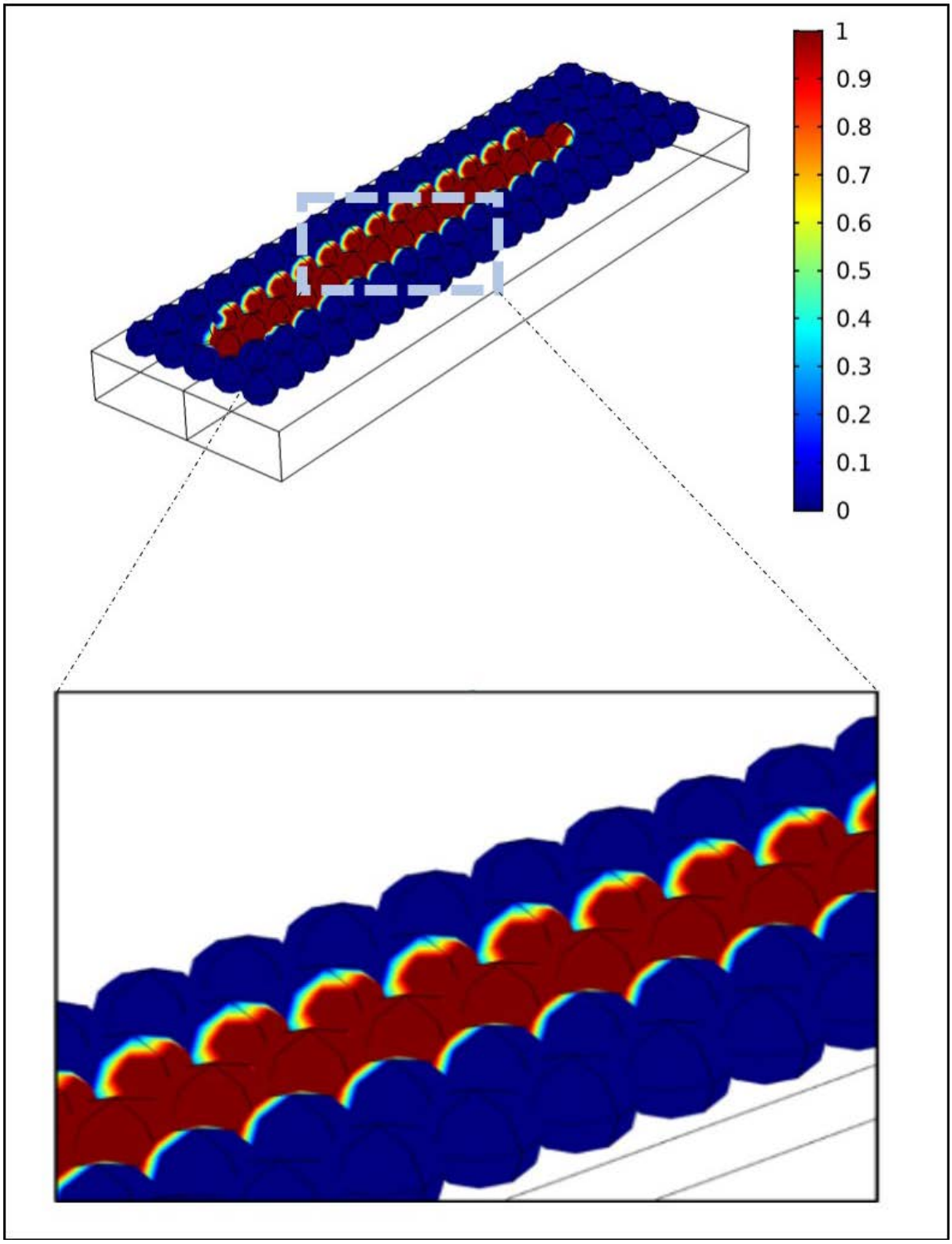


Figure 3.2. Phase change from solid phase (0) to liquid phase (1).

Selecting proper process parameters is undoubtedly crucial for various aspects of additively manufactured parts. Optimal process parameters can reduce the cracking effect and reach fully density [59]. This also leads to optimum and adequate microstructure and mechanical properties [60]. Improper parameters will result in pores and spatters, leading to undesired

mechanical properties; also, low speed of manufacturing or high fabrication costs will be encountered if improper process parameters are used. The investigated model enables us to simulate the process with selected parameters. That is to say, the model is a tool that could be used to predict the process parameters in the SLM.

Low melt-pool temperature will result in pores in the manufactured parts. Lack of fusion causes elongated and inconsistent pores. These defects refer to insufficient temperature in the melt-pool [61]. Through low temperature, there might be unmelted powders, which will lead to a part full of pore defects. On the other hand, extreme temperatures will result in defects such as spatter, overcooking, holes, and high heat tensions. Spatters come up due to evaporation force, which forces the melted metal to separate from the plane by overcoming surface tension. It leads to surface defects in layers. Accordingly, the temperature exceeding the evaporation temperature leads to undesirable products. Evaporation may lead to the formation of keyhole pores that are deeply embedded in the part [62]. However, fabrication speed is an important issue in the process; high scanning speeds lead to fast fabrication.
Referring to all the mentioned notes above, the most important goal is to reach a complete melting without evaporation. Indeed, the favorable parameters are a set of parameters that melt the distributed powder layer completely and also melt a part of the prior layers to make a proper bond between layers. For this purpose, the selected parameters should satisfy the melting phenomena all over the powder layer. The most critical area is the depth of the powder layer. If the parameter set produces enough temperature at a depth of the powder layer for melting, and meanwhile the parameter set does not lead to any evaporation at any part of the powder layer, this may be considered as a proper and satisfactory parameter set which does not cause any defects due to temperature deficiency or excess. Formation of the spatter and residual porosities are related and promoted by instability regimes at high energy density [63]. For this purpose, here, the maximum temperature was recorded at the depth of 40 μm, since the powder layer thickness in experiments was 40 μm. In order to reveal the effects of different process parameters on the SLM additive manufacturing of stainless steel, the simulations have been carried out for the different sets of parameters.

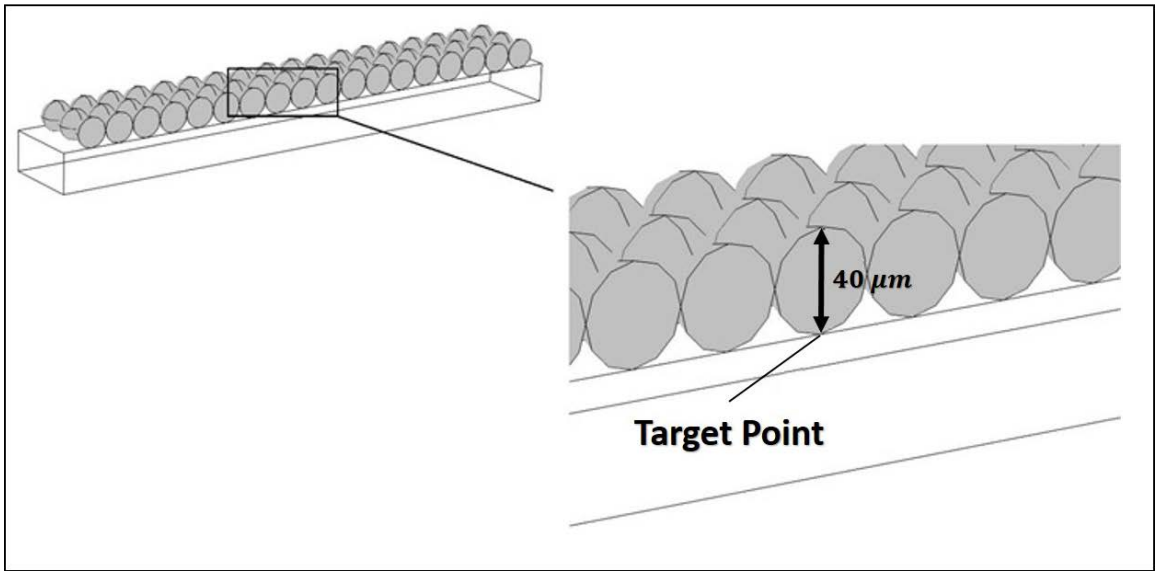


Figure 3.3. Target point to record temperature during simulations.

3.1.1 Effect of laser power

Simulations were performed for four different scanning velocities. Referring to Equation (12), regarding Rosenthal's equation, which approximates the temperature distribution of a single track in the SLM process [64], the relation between temperature and laser power, in a constant moving heat point source velocity, is a linear relationship. Figure 3.4 shows the simulation results and fitted curves of the powder layer tem-perature at various laser powers.

$$T(y) = \frac{AP}{2\pi rk}.exp(\frac{-v_x}{2\alpha}) \quad (12)$$

where v_x (m/s) is the moving heat point source velocity and α is the thermal diffusivity (m^2/s).

At each scanning velocity, temperature values were recorded after a steady state was achieved. Achieving the stability condition and, respectively, the point of recording the temperature throughout the strip, was different at every scanning velocity.

Table 3.1 shows equations of the fitted curves for laser power–temperature simulation results in which the most important factor is the slope. Referring to Table 3.1, the slope of the curve increases when the scanning velocity decreases. In fact, the temperature increase rate rises when scanning velocity decreases. The slope of the linear equation may be used as a transfer function in a control system design if a process control is considered for the 3D printer

machine. Namely, by using the relationship between temperature and laser power for a given scanning speed and laser spot diameter, the machine could be able to determine a suitable laser power to achieve the desired temperature instantly.

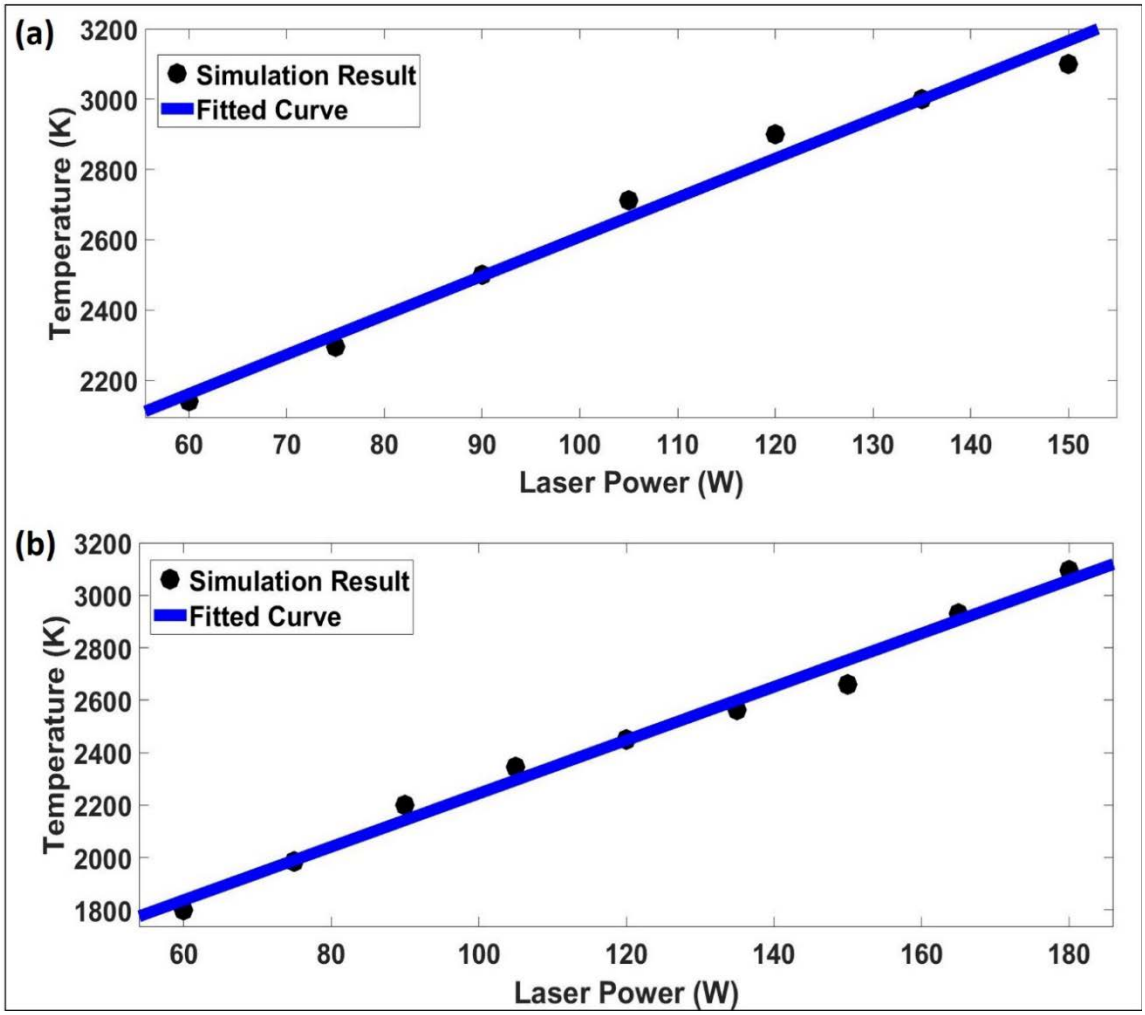


Figure 3.4. Simulation results and fitted curves of melt-pool temperature at various laser powers with a laser spot diameter of 80 μm and scanning velocity of (a) 600 mm/s, (b) 900 mm/s, (c) 1200 mm/s, and (d) 1400 mm/s.

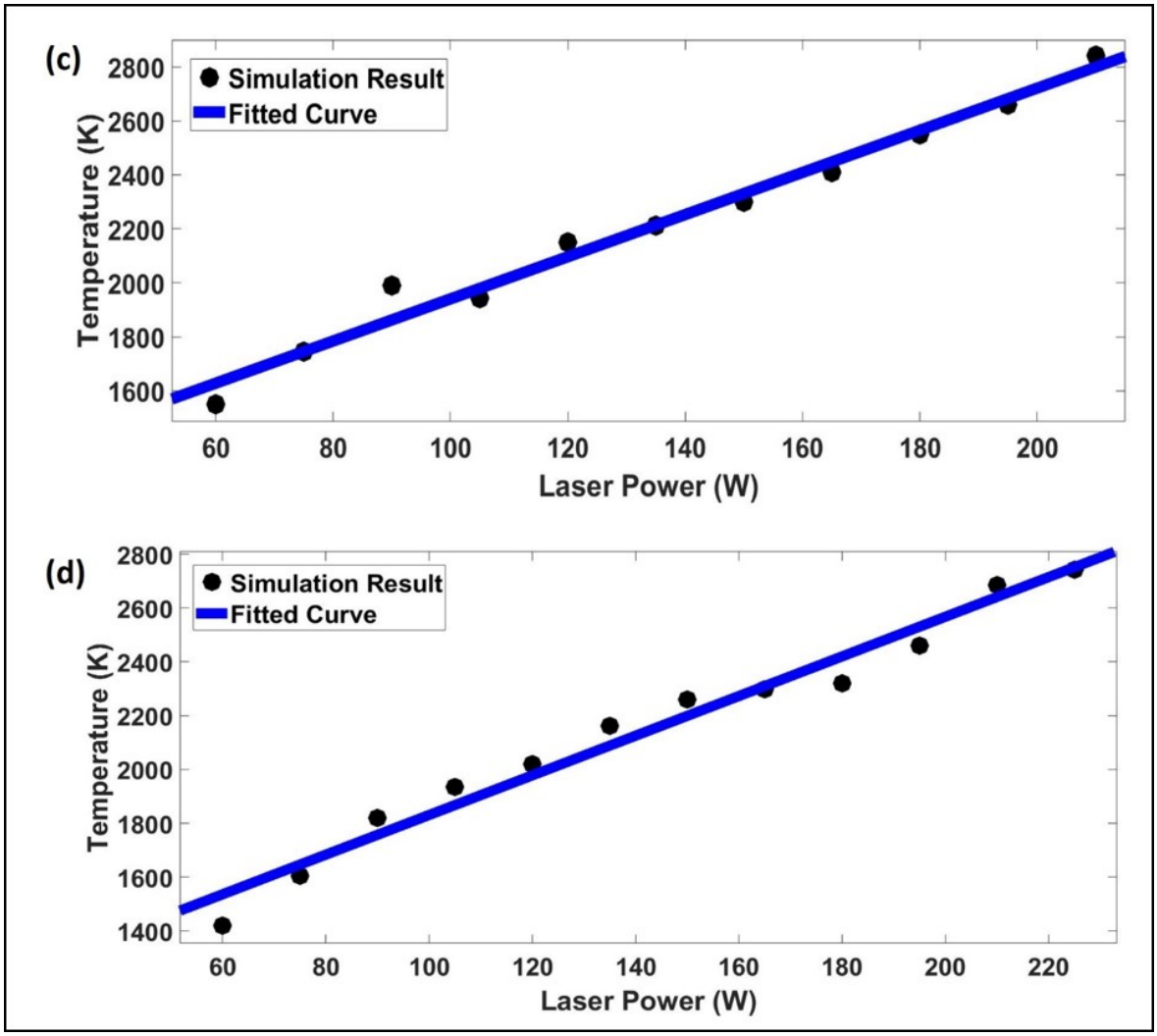


Figure 3.4. (Continue) Simulation results and fitted curves of melt-pool temperature at various laser powers with a laser spot diameter of 80 μm and scanning velocity of (a) 600 mm/s, (b) 900 mm/s, (c) 1200 mm/s, and (d) 1400 mm/s.

Table 3.1. Equations of fitted curves of laser power–temperature simulation results with a laser spot diameter of 80 μm. In equations, T denotes the temperature(K) and P denotes the laser power (W).

Velocity (mm/s)	Fitted Curve Equation	Slope	Domain	Range	Error (%)
600	$T = 11.17P + 1491$	11.7	$60 \leq P \leq 160$	$2161 \leq T \leq 3278$	1.35
900	$T = 10.18P + 1227$	10.18	$60 \leq P \leq 190$	$1837 \leq T \leq 3161$	1.56
1200	$T = 7.8P + 1160$	7.8	$60 \leq P \leq 260$	$1628 \leq T \leq 3188$	2.16
1400	$T = 7.367P + 1094$	7.637	$60 \leq P \leq 280$	$1491 \leq T \leq 3111$	2.96

Figure 3.5 shows the fitted curves of laser power–temperature in various scanning speeds together. The red lines split the graph into three parts. The upper part of the evaporation temperature line denotes laser powers, which will cause evaporation mixing melting and the related defects in part, while the lower part of the melting temperature line will have unmelted or low-melted/sintered powders in the final part. The laser power should be able to melt not only the powders of the new layer, but also it should be able to melt a part of the previous melted layers (lower and neighboring layers) again to bond the new and prior layers together. The proper laser powers for melting are the areas between evaporation and melting temperature lines.

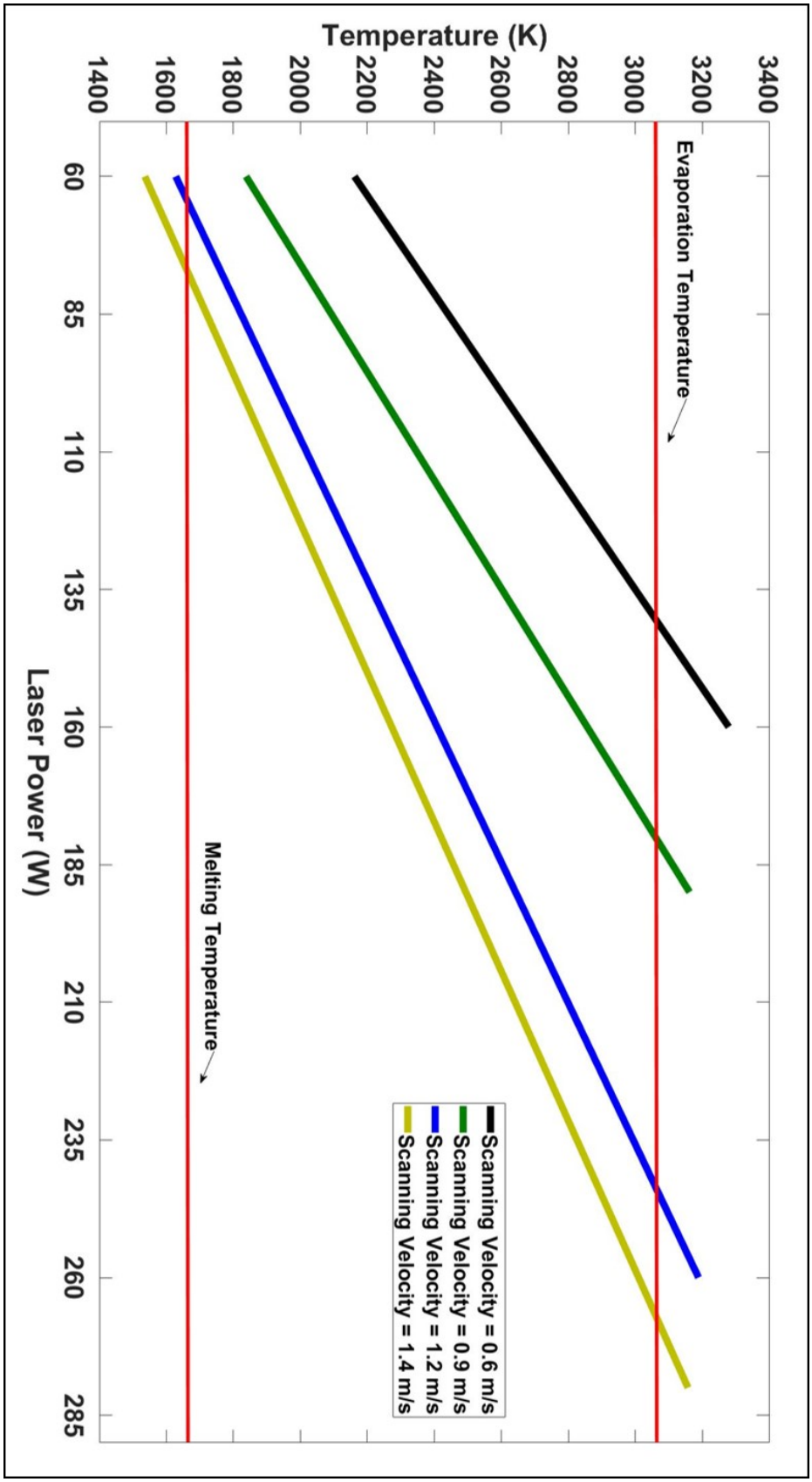


Figure 3.5. Fitted curves of laser power–temperature during various scanning velocities with a laser spot diameter of 80 μm.

3.1.2 Effect of laser spot diameter

Figure 3.6 illustrates the results of the simulations and fitted curves for the effect of the laser spot diameter on the temperature of the powder layer at the depth of 40 μm. Increasing the melt-pool temperature can be explained via the energy density concept. Energy density is defined as the ratio of laser power to fabrication parameters, one of which is the laser spot diameter. The smaller the spot diameter, the higher the energy density and melt-pool temperature.

Referring to Equations (2) and (3), the second-order relation of the laser spot diameter to the heat source could be described. The Gaussian distribution of the heat source for several laser spot diameters is shown in Figure 3.7 During constant laser power, the effect of different laser spot diameters on the heat source is evident. As discussed earlier, temperature values have been recorded at the same conditions.

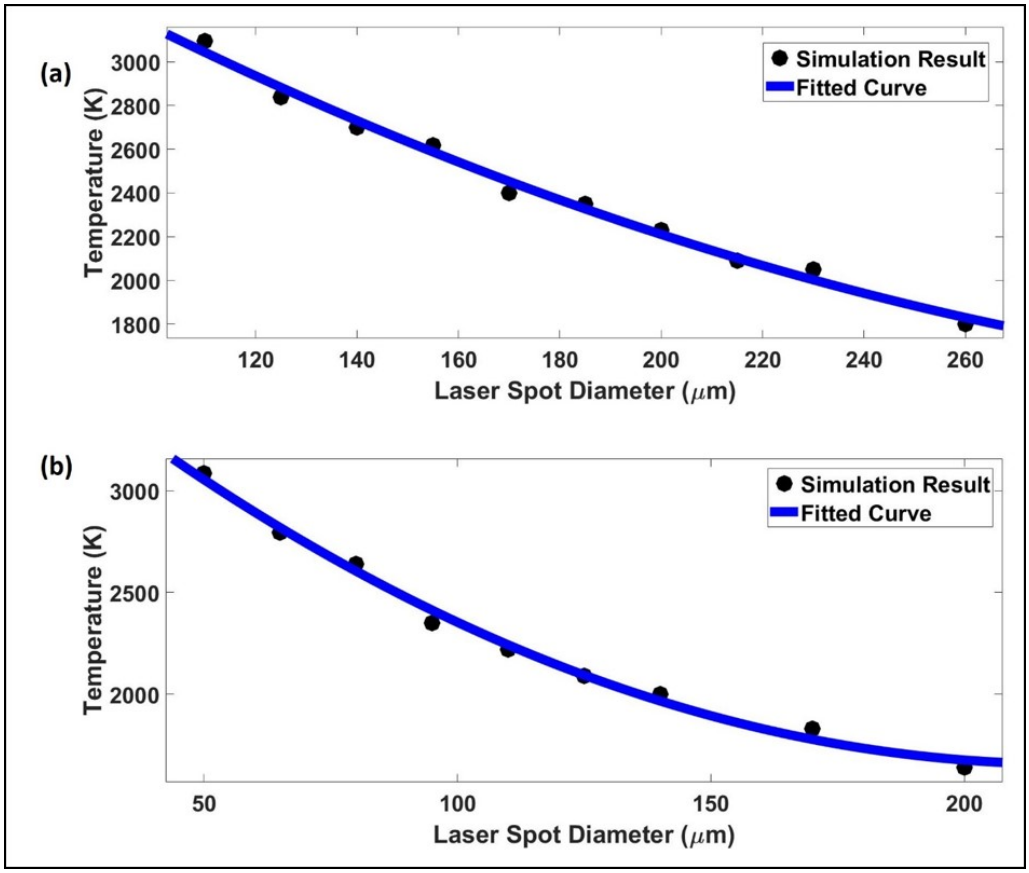


Figure 3.6. Simulation results and fitted curves of melt-pool temperature at various laser spot diameters with a laser power of 150 W and scanning velocity of (a) 600 mm/s, (b) 900 mm/s, (c) 1200 mm/s, and (d) 1400 mm/s.

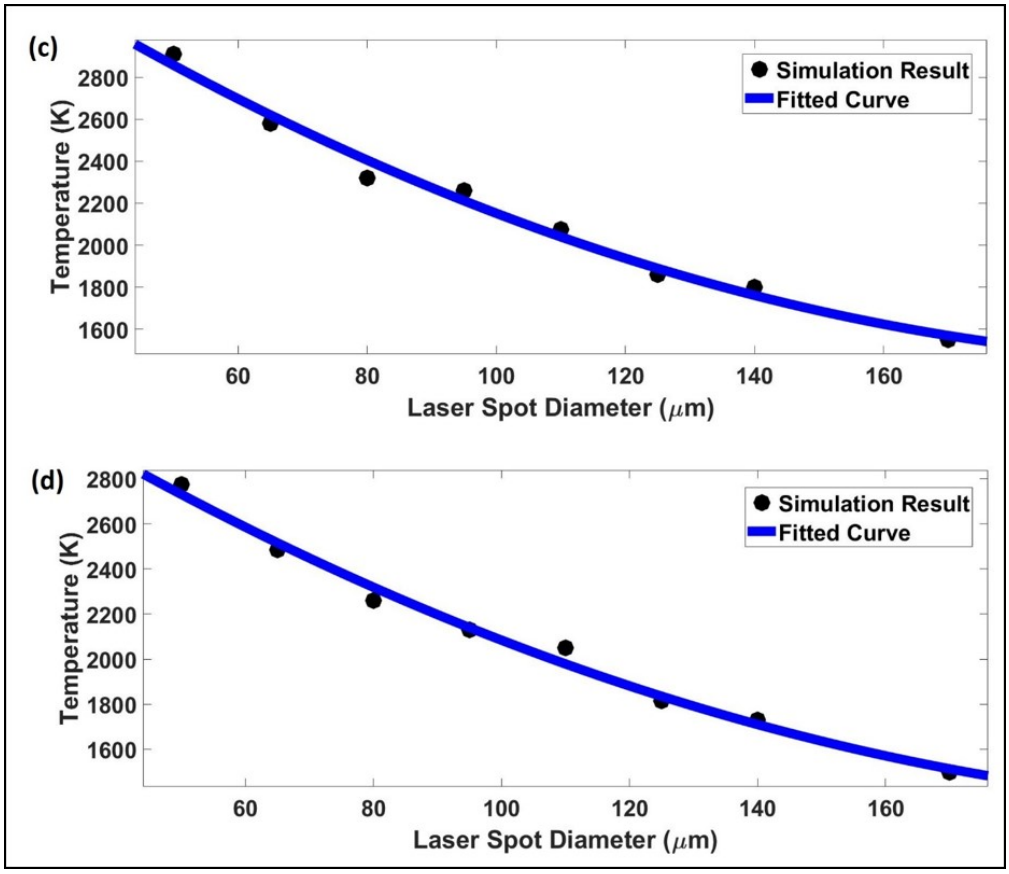


Figure 3.6. (Continue) Simulation results and fitted curves of melt-pool temperature at various laser spot diameters with a laser power of 150 W and scanning velocity of (a) 600 mm/s, (b) 900 mm/s, (c) 1200 mm/s, and (d) 1400 mm/s.

Table 3.2 denotes the equations of the second-order fitted curves of the laser spot diameter-temperature curves.

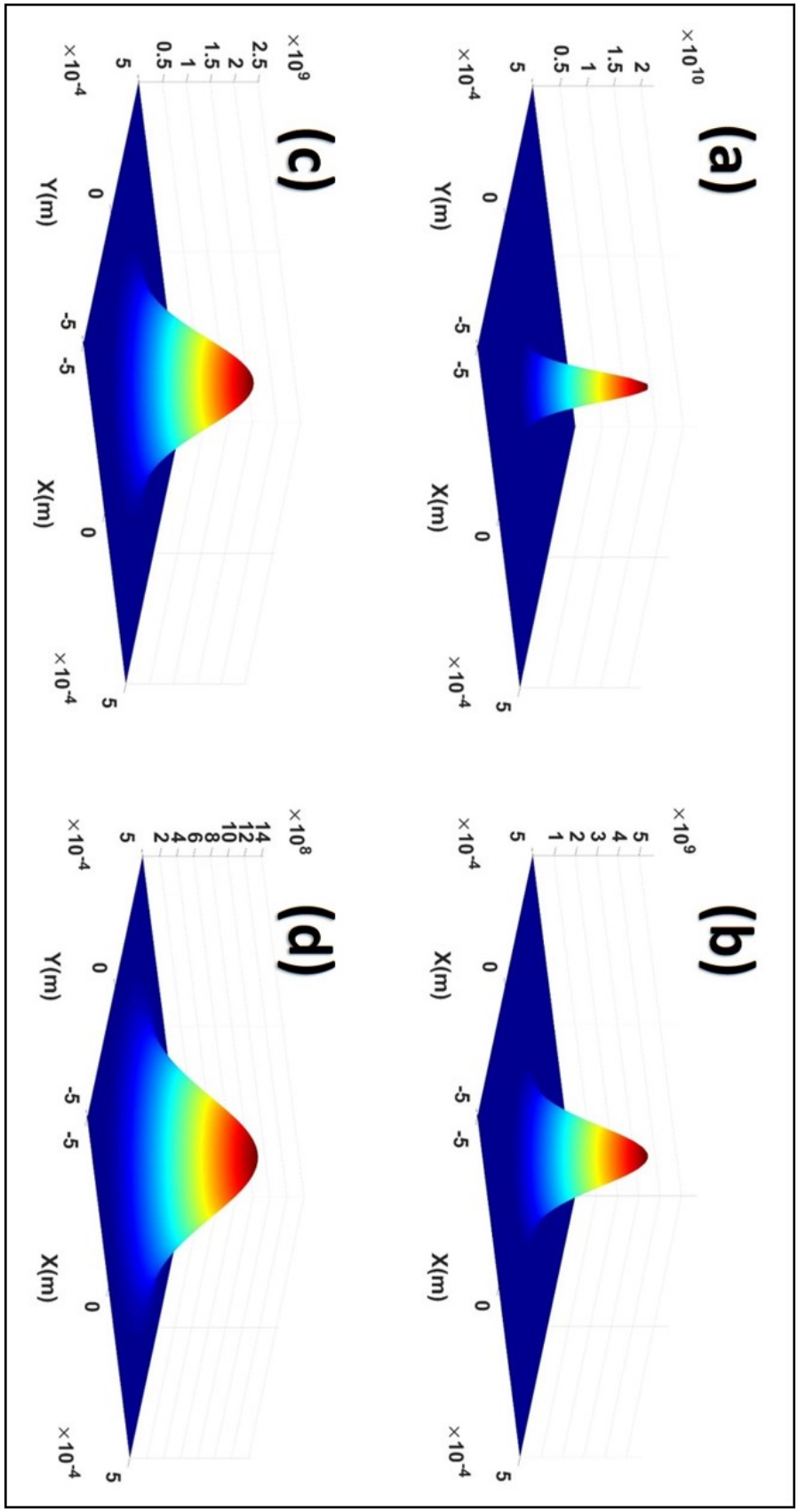


Figure 3.7. Gaussian distribution of the heat source for laser spot diameters of (a) 50 μm, (b) 100 μm, (c) 150 μm, and (d) 200 μm.

Table 3.2. Equations of fitted curves of laser spot diameter–temperature simulation results with a laser power of 150 W. In equations, T represents the temperature(K) and d stands for the laser spot diameter (μm).

Velocity (mm/s)	Fitted Curve Equation	Domain	Range	Error (%)
600	$T = 0.01945d^2 - 15.29d + 4491$	$100 \leq d \leq 310$	$1620 \leq T \leq 3156$	1.365
900	$T = 0.04837d^2 - 21.29d + 3999$	$40 \leq d \leq 210$	$1661 \leq T \leq 3224$	1.52
1200	$T = 0.0482d^2 - 21.33d + 3803$	$40 \leq d \leq 170$	$1569 \leq T \leq 3026$	1.98
1400	$T = 0.0398d^2 - 18.9d + 3576$	$40 \leq d \leq 170$	$1513 \leq T \leq 2883$	1.57

In Figure 3.8, the red lines split the graph into three parts. It illustrates the fitted curves of the laser spot diameter–temperature relationship. The diameter values whose relative temperatures are under the melting line will not have sufficient capability to melt the stainless-steel powder completely. However, those diameters whose relative temperatures are above the evaporation line will result in evaporation mixing with melting under the defined situation of the laser power, scanning velocity, and laser spot diameter. The temperature below the melting line will lead to defects such as not melting of powders, district melting, and weak or lack of bonding between layers of printing. On the other hand, temperatures exceeding evaporation temperature line will lead to defects such as spatters, holes, overcooking, and high heat tensions. Suitable diameters for fabrication are the diameters in the middle part of the graph.

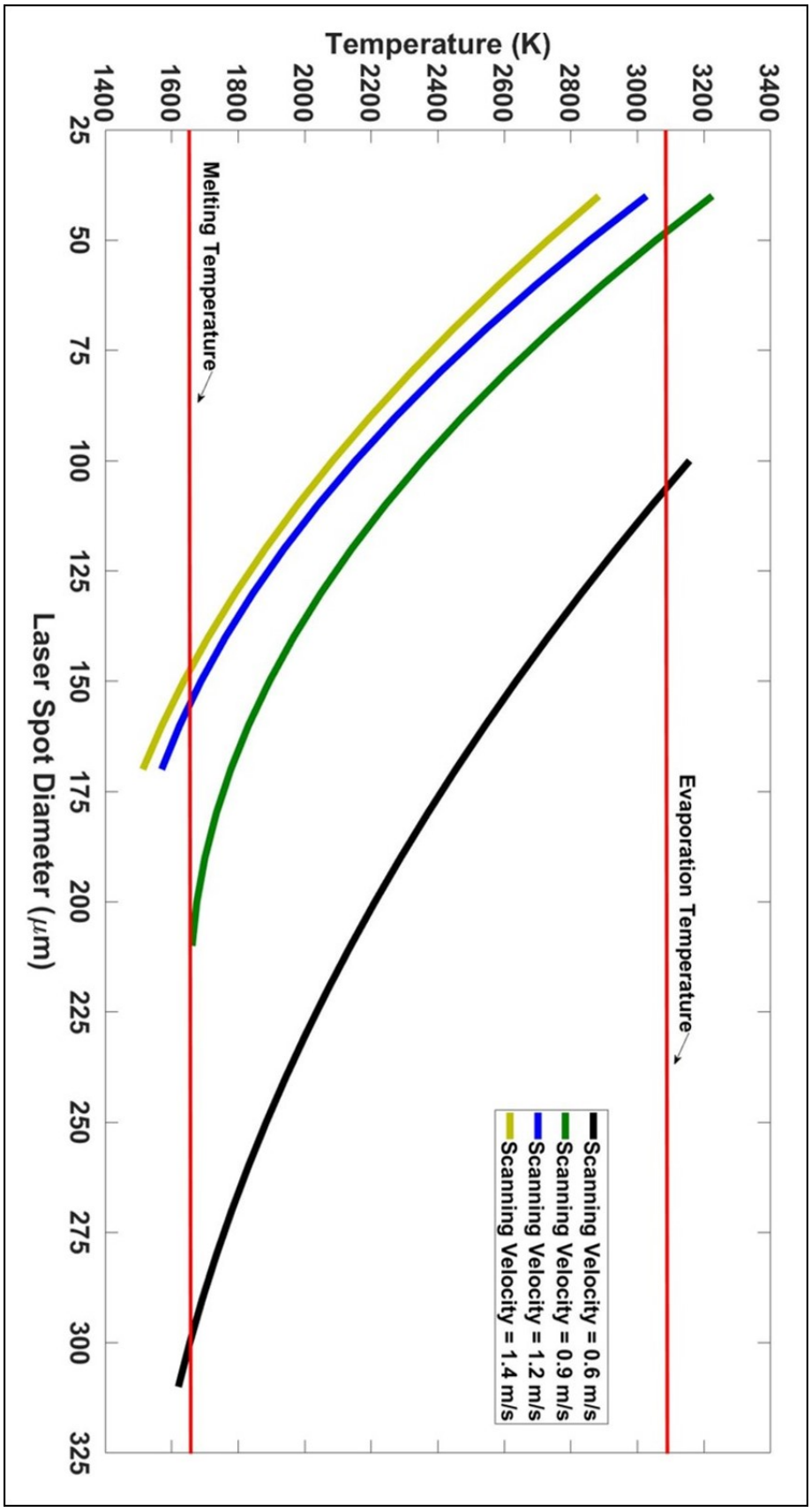


Figure 3.8. Fitted curves of laser spot diameter–temperature during various scanning velocities with a laser power of 150 W.

3.2 AlSi10Mg

In the case of the AlSi10Mg, the model simulates a 3-D laser-powder interaction to extract the proper fabrication process parameters and indicate the sensitive and critical parameters as well. Mathematical relationships describing the relationship between laser power-temperature and laser spot diameter-temperature at different scanning velocities were obtained. Here, because of the high heat conduction specialty of the AlSi10Mg, temperatures were recorded at the surface of the melt pool until a steady melt pool temperature was reached. Figure 3.9a shows a complete view of the temperature distribution and Figure 3.9b shows a symmetrical view of the contours and isosurfaces of the temperature generated in AlSi10Mg powders exposed to the laser beam. Also, Figure 3.10 shows the phase of the solid and liquid and also the mushy border zone between them which is illustrated by Carman- Kozeny equation [54].

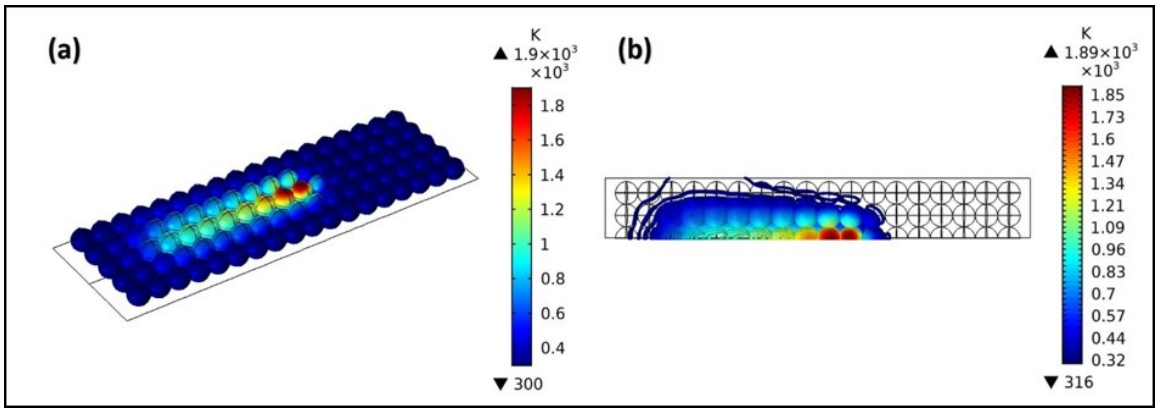


Figure 3.9. 3-D temperature distribution using 800 mm/s scanning velocity, 200 W laser power and 140 μm laser spot diameter. a) Complete view, b) Symmetrical view of isosurface and contours distribution. c) Phase change during process from solid to liquid, while solid phase is denoted with 0 and the liquid phase is denoted with 1.

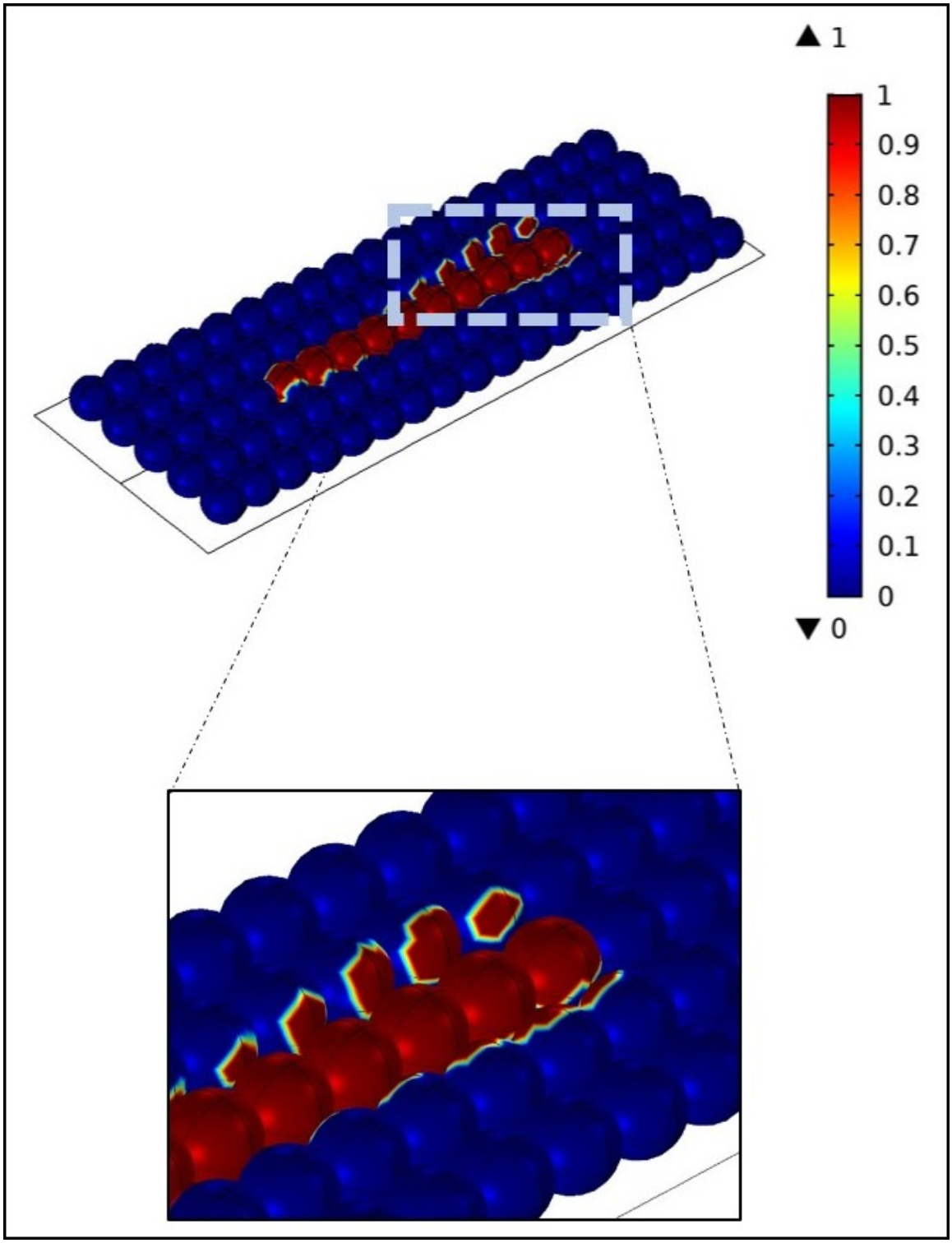


Figure 3.10. Phase change during process from solid to liquid, while solid phase is denoted with 0 and the liquid phase is denoted with 1.

As mentioned for Stainless Steel 316L, we discussed the same in AlSi10Mg and got the results. One of the most concerning issues of the SLM is selecting the proper process parameters and controlling the melt pool temperature during the fabrication process

respecting the product requirements. The selected process parameters should be able to melt the metal powders and also do not cause over-melting. On the other hand, a controllable and constant temperature in the melt pool during the melting process is desired. The minimum deviation from the set temperature for the melt pool, the more homogeneous microstructure in the final part.

As stated in the Stainless Steel 316L discussion, achieving an optimum microstructure and mechanical properties of the final product will make sense by choosing the right parameters and controlling the temperature of the melt pool. Insufficient energy with incorrect process parameters will lead to not-melted or low-melted powders. In addition, incorrect process parameters cause nonconnected melt pools, which are results of low energy and melt pool lifetime in the SLM. On the other hand, excessive energy due to incorrect process parameters cause various defects like spatter, balling, thermal cracks, and holes. Extreme temperature and evaporation in laser-irradiated metal powders are the leading causes of these defects. Accordingly, all of these defects also directly affect the mechanical properties in a bad manner. The appropriate process parameter should form a temperature that melts the metal powder thoroughly, and at the same time, the temperature generated should not exceed the evaporation temperature to avoid defects arising from evaporation.

The next sections explain the effect of the laser power and laser spot diameter on the melt pool temperature in various scanning velocities and discuss the “sensitive” areas in graphs. In addition, their relations were formulated mathematically to indicate the relationship among the process parameters with melt pool temperature.

3.2.1 Effect of laser power

Referring to the Rosenthal’s equation (Equation 12), the melt pool temperature distribution in single track during SLM process have a linear behavior for changing laser powers [64]. Therefore, the melt pool temperatures achieved from simulations for changing laser powers are fitted on a linear curve.

Figure 3.11 shows the melt pool temperature for different laser powers at various scanning velocities. Moreover, it is clear that the increase in the scanning velocity of the laser beam

leads to a decrease in the melt pool temperature due to the reduction of the interaction time of the metal powder with the laser beam.

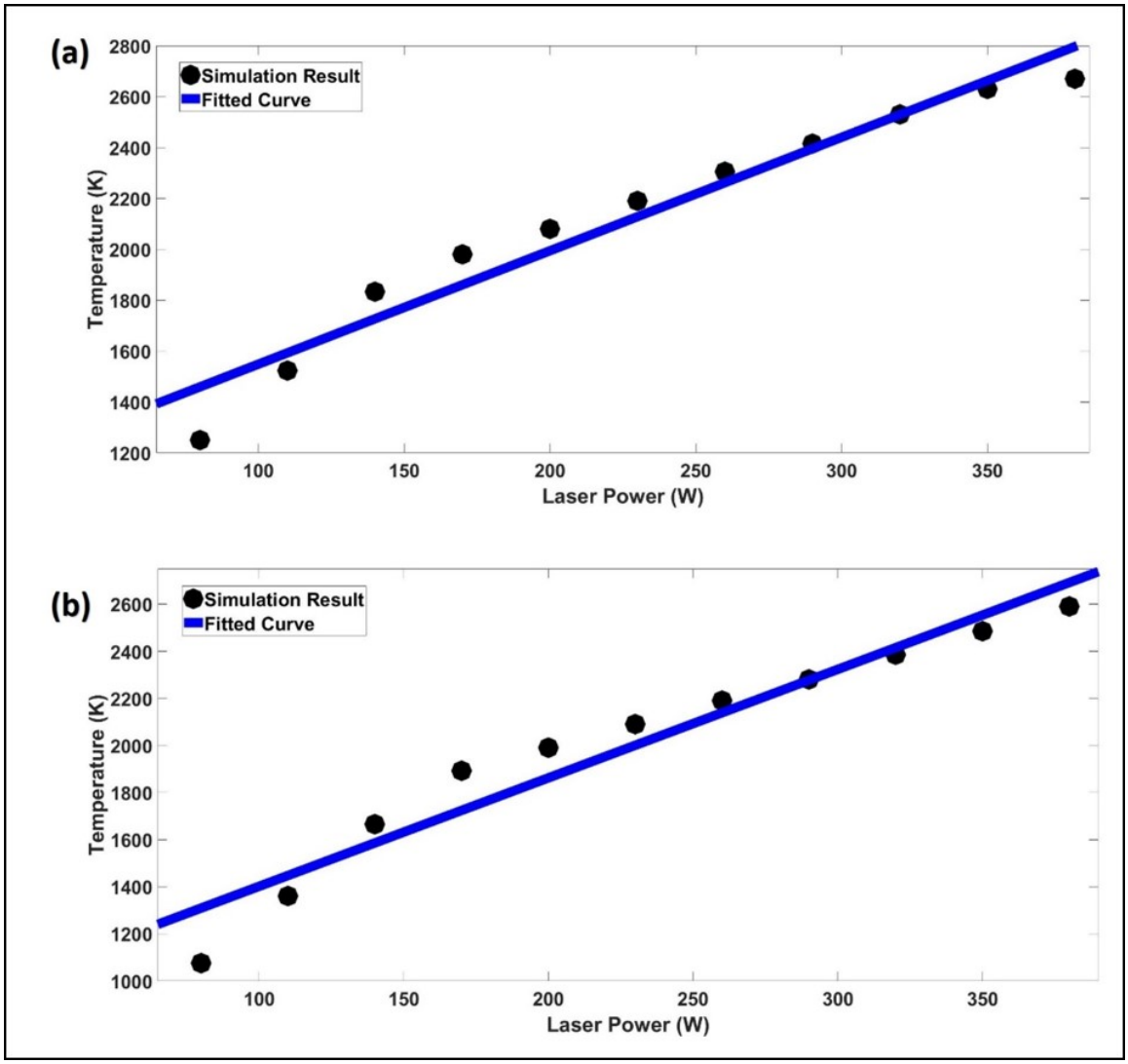


Figure 3.11. Simulation results and fitted curves of melt pool temperature at different laser powers and a laser spot diameter of 140 μm; scanning velocity of a) 600 mm/s, b) 800 m m/s, c) 1100 mm/s, and d) 1400 mm/s.

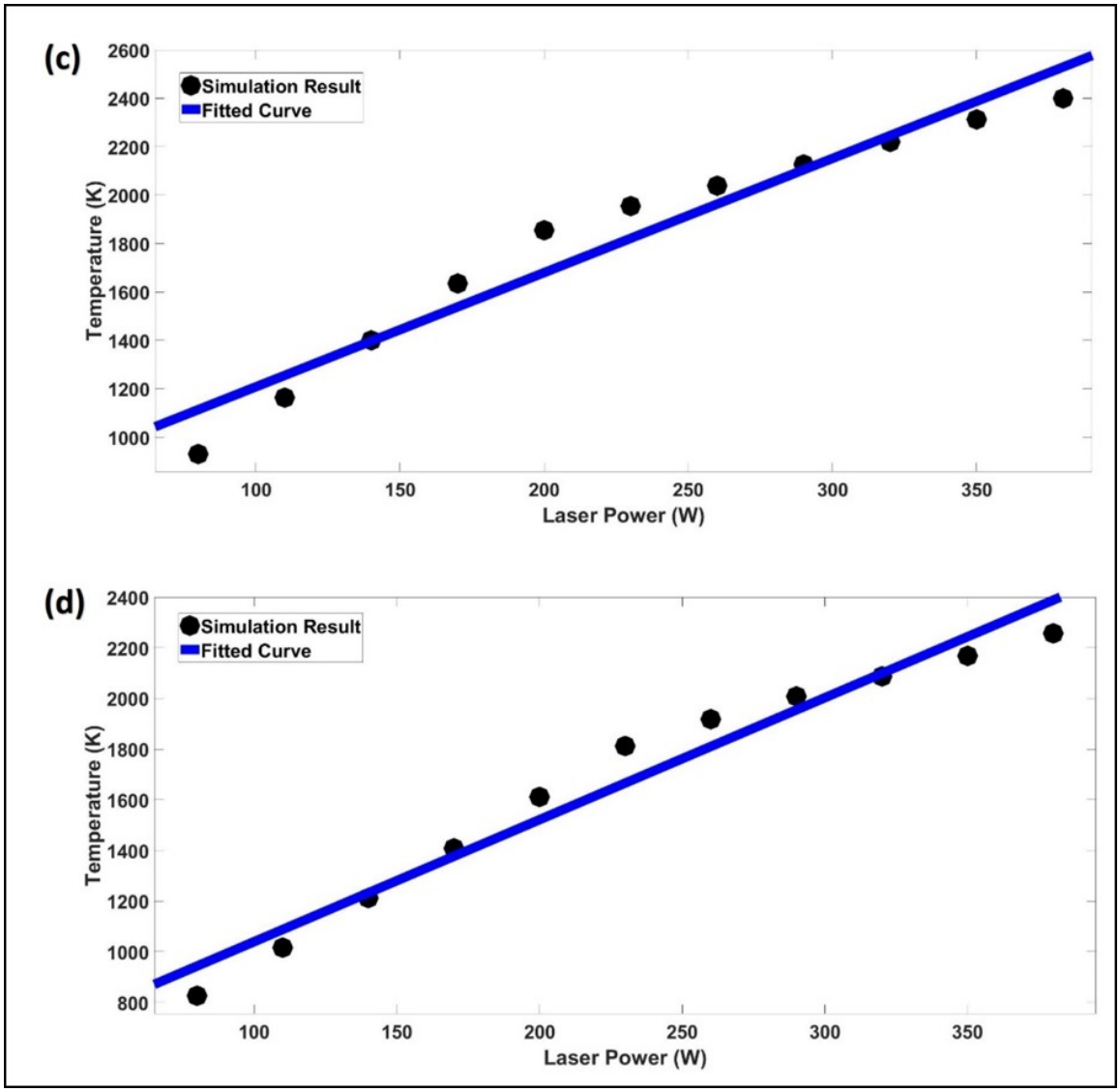


Figure 3.11. (Continue) Simulation results and fitted curves of melt pool temperature at different laser powers and a laser spot diameter of 140 μm; scanning velocity of a) 600 mm/s, b) 800 m m/s, c) 1100 mm/s, and d) 1400 mm/s.

The mathematical relationships (fitted curves equations) between laser power and melt pool temperature for various scanning velocities were tabulated in Table 3.3. Mathematical relationships allow us to calculate the temperature of the melt pool by entering the value of laser power. Their slope is the most important part of them because it could be used as a transfer function in designing a control system for a 3-D printing machine.

Table 3.3. Equations of the fitted curves for simulation results of the laser power-temperature during different scanning velocities. (T: Melt Pool Temperature- P: Laser Power- Laser Spot Diameter =140 μm).

Velocity (mm/s)	Fitted Curve Equation	Slope	Domain	Range
600	$T = 4.459P + 1102$	4.459	$80 \leq P \leq 380$	$1250 \leq T \leq 2670$
800	$T = 4.609P + 940$	4.609	$80 \leq P \leq 380$	$1075 \leq T \leq 2590$
1100	$T = 4.721P + 735.8$	4.72	$80 \leq P \leq 380$	$930 \leq T \leq 2400$
1400	$T = 4.817P + 557.9$	4.817	$80 \leq P \leq 380$	$826 \leq T \leq 2257$

Figure 3.12 shows the fitted curves together for the four different velocities with melting and evaporation temperature border lines. These lines split the graph into three parts. The part below the melting temperature line is the insufficient parameter area for melting, and the part above the evaporation temperature line is the process parameters area that will cause evaporation during production. The middle area is the potential area where appropriate process parameters for production can be selected according to simulations.

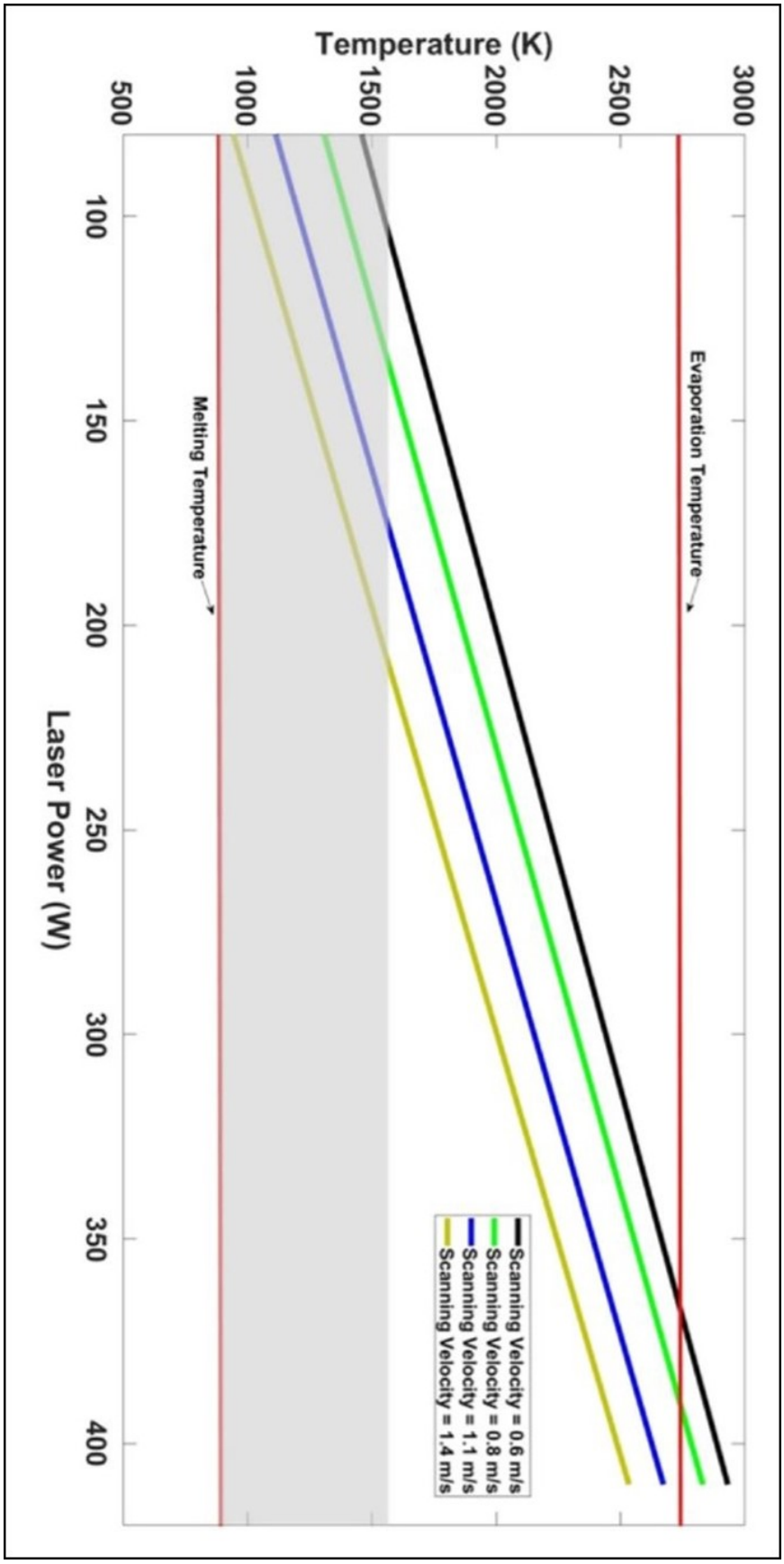


Figure 3.12. Fitted Curves of the laser power- temperature for a laser spot diameter of 140 μm at different scanning velocities.

Areas near the melting and evaporation temperature lines are “sensitive” and can cause fluctuations in production. In the area inside the gray box, the region close to the melting temperature line, the life-time (duration in which the powder melts and eventually solidifies) of the melt pool is low. Low life-time means that, although the temperature is over the melting temperature of AlSi10Mg powders, it can lead to unconnected melt pools or incompletely melted powders. Therefore, it is recommended to avoid these areas during fabrications and do not select parameter sets inside the gray box.

3.2.2 Effect of laser spot diameter

As mentioned earlier in the Stainless Steel 316L discussion, the effect of the laser spot diameter parameter on the melt pool temperature can be explained by the concept of laser energy density, which is defined as the ratio of laser power to process parameters, including laser spot diameter. The laser spot diameter has an opposite relation with laser energy density and melt pool temperature. Also, the laser spot diameter has a second-order relationship with generated laser energy and correspondingly temperature referring to the Gaussian distribution equation of the laser beam (Equations 2 and 3). Figure 3.13 shows the simulation results and fitted curves of the melt pool temperatures for different laser spot diameters. In a constant laser power and scanning velocity, small spot diameters increase the laser energy density and mutually raise the melt pool temperature.

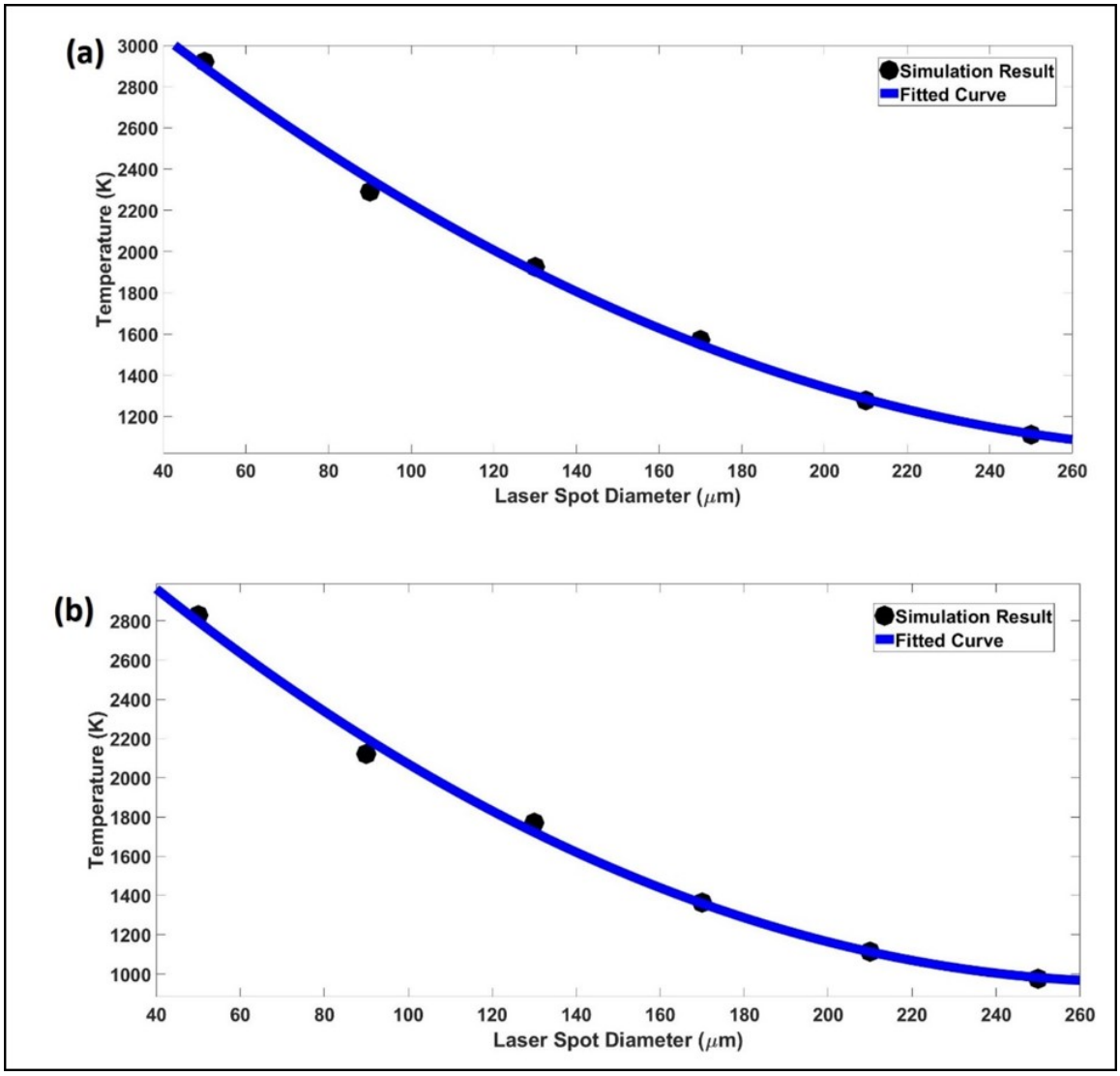


Figure 3.13. Simulation results and fitted curves of melt pool temperature at different laser spot diameters and a laser power of 110 W; scanning velocity of a) 600 mm/s, b) 800 mm/s, c) 1100 mm/s, and d) 1400 mm/s.

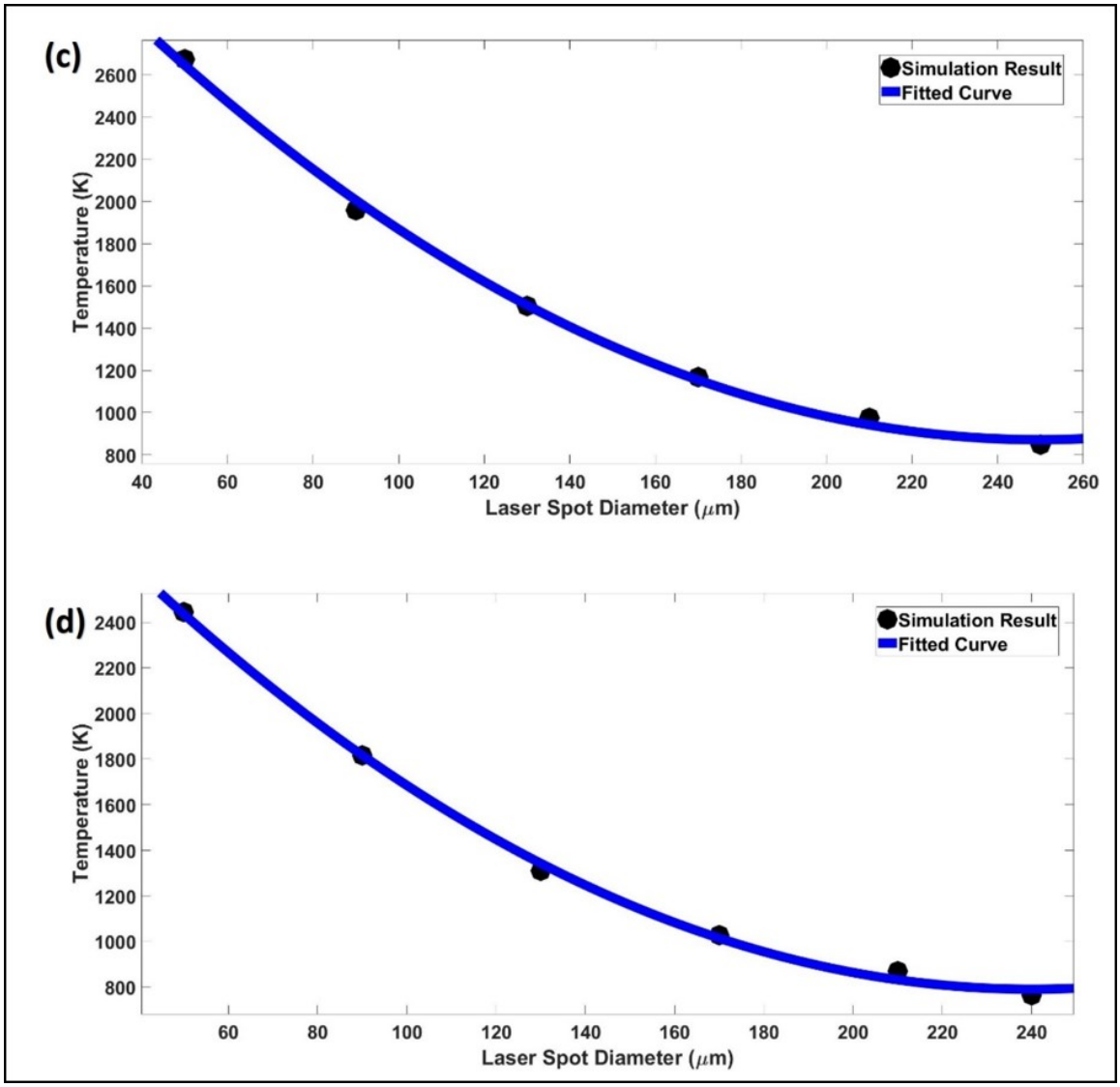


Figure 3.13. (Continue) Simulation results and fitted curves of melt pool temperature at different laser spot diameters and a laser power of 110 W; scanning velocity of a) 600 mm/s, b) 800 mm/s, c) 1100 mm/s, and d) 1400 mm/s.

Table 3.4 illustrates the mathematical expressions of the relationship between the laser spot diameter and melt pool temperature for various scanning velocities. These relationships are another basic material for controller design that can control the melt pool temperature by interfering with the laser spot diameter of the process parameter set. As discussed earlier, if the melt pool temperature deviates from the set temperature, the machine can eliminate the deviation and restore the temperature to the specified amount by the intervention of the designed controller using the following relationships.

Table 3.4 Equations of the fitted curves for simulation results of the laser spot diameter-temperature at different scanning velocities. (T: Melt Pool Temperature- d: Laser Spot Diameter- Laser Power = 110 W).

Velocity (mm/s)	Fitted Curve Equation	Domain	Range
600	$T = 0.02906d^2 - 17.6d + 3700$	$50 \leq d \leq 250$	$1111 \leq T \leq 2920$
800	$T = 0.03626d^2 - 19.95d + 3702$	$50 \leq d \leq 250$	$975 \leq T \leq 2828$
1100	$T = 0.04446d^2 - 22.21d + 3645$	$50 \leq d \leq 250$	$848 \leq T \leq 2674$
1400	$T = 0.04549d^2 - 21.85d + 3414$	$50 \leq d \leq 240$	$765 \leq T \leq 2444$

Figure 3.14 shows together fitted curves for laser spot diameter-temperature at different scanning velocities. The graph is divided into three areas and the process parameter sets of the middle area are potentially suitable for production. The process parameters locating above the evaporation temperature line will result in evaporation mixed melt pool. Spot diameters that cause a temperature below the melting temperature line are insufficient diameters for melting the powders. Similarly, area inside the gray box are hazardous areas due to possible insufficient life-time and may cause fluctuations in melting. According to this, employing the parameter sets from inside the box are not recommended.

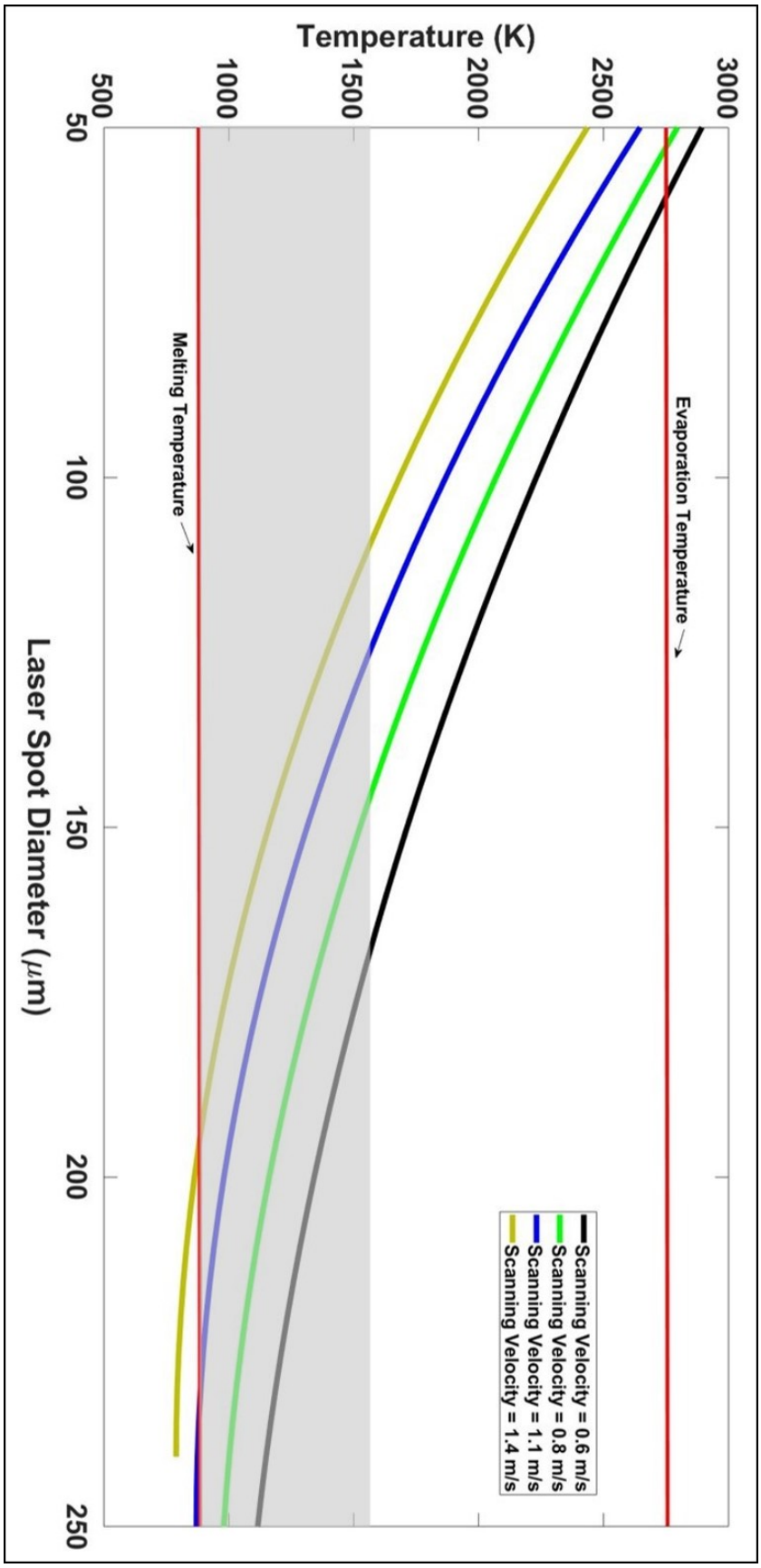


Figure 3.14. Fitted curves of the laser spot diameter- temperature for a Laser Power of 110 W at different scanning velocities.

4. EXPERIMENTAL VALIDATION

4.1 Stainless Steel 316L

Using Stainless Steel 316L powders, ten samples were manufactured by Concept Laser M2 Cusing Machine. The powders used for the fabrication were gas atomized Concept Laser SS 316L powders with a powder size distribution shown in Tables 4.1 and 4.2. Figure 4.1 shows an SEM image of the powders, which are almost spherical in structure.

Table 4.1. Results of the sieve analysis of powders used for fabrication of samples [65].

Particle Size	< 100 µm	< 80 µm	< 63 µm	< 45 µm	< 32 µm	< 20 µm
Value (%)	99.88	99.60	99.11	97.59	73.83	23.42

Table 4.2. Powder size distribution of powders used for the fabrication of samples [65].

Parameter	Dv (10)	Dv (50)	Dv (90)	Width (90;10)
Unit	μm	μm	μm	-
Result	18.680	29.631	47.984	0.989

One of the most important factors in the modeling is the temperature-dependent material properties. Table 4.3 shows the material properties used for Stainless Steel 316L in the model [66][67][68].

Samples were fabricated with ten different sets of parameters, which are listed in Table 4.4. Scanning velocities of 600 mm/s, 900 mm/s, 1200 mm/s, and 1400 mm/s were used during the experimental study. Fabricated samples were categorized into two groups of constant laser spot diameter and constant laser power. Based on the simulation results obtained from the multiphysics software Comsol, three regions were specified which are: “below melting temperature line”, “between melting temperature and evaporation

temperature lines", and "above the evaporation temperature line". The emphasis was given to the region that offers defectless and usable structures, which is "between melting and evaporation temperature lines".

Table 4.3. Material properties of Stainless Steel 316L [66][67][68].

Material Property	Symbol	Value	Unit
Melting Temperature	T_m	1650	K
Melting Interval	δT	± 10	K
Evaporation Temperature	T_{ev}	3086	K
Latent Heat of Melting	H_m	$2.8 \cdot 10^5$	J/kg
Latent Heat of Evaporation	H_{ev}	$6.1 \cdot 10^6$	J/kg
Density	ρ	$7700\ (solid) - 8000\ (liquid)$	$\mathrm{kg/m^3}$
Thermal Conductivity	k	$11.82 + 1.06 \times 10^{-2} T$	W/m. K
Specific Heat Capacity	C_p	$330.9 + 0.563\ \mathrm{T} - 4.015 \times 10^{-4}\ T^2 + 9.465 \times 10^{-8}\ T^3$	J/kg . K
Absorption Coefficient	A	$0.55\ (solid) - 0.3\ (liquid)$	–
Marangoni Coefficient	$\mathrm{d}\gamma/\mathrm{dT}$	-0.40×10^{-3}	N/m. K

This rich area shows the variety of parameters presented by the research. In addition, samples were fabricated employing parameters from sensitive areas with a potential of lack of fusion, "below melting temperature line", and over melting, "above the evaporation temperature line", to show the kind of results obtained by selecting parameters from these sensitive areas. Microstructures were examined and results with respect to the selected parameters were obtained.

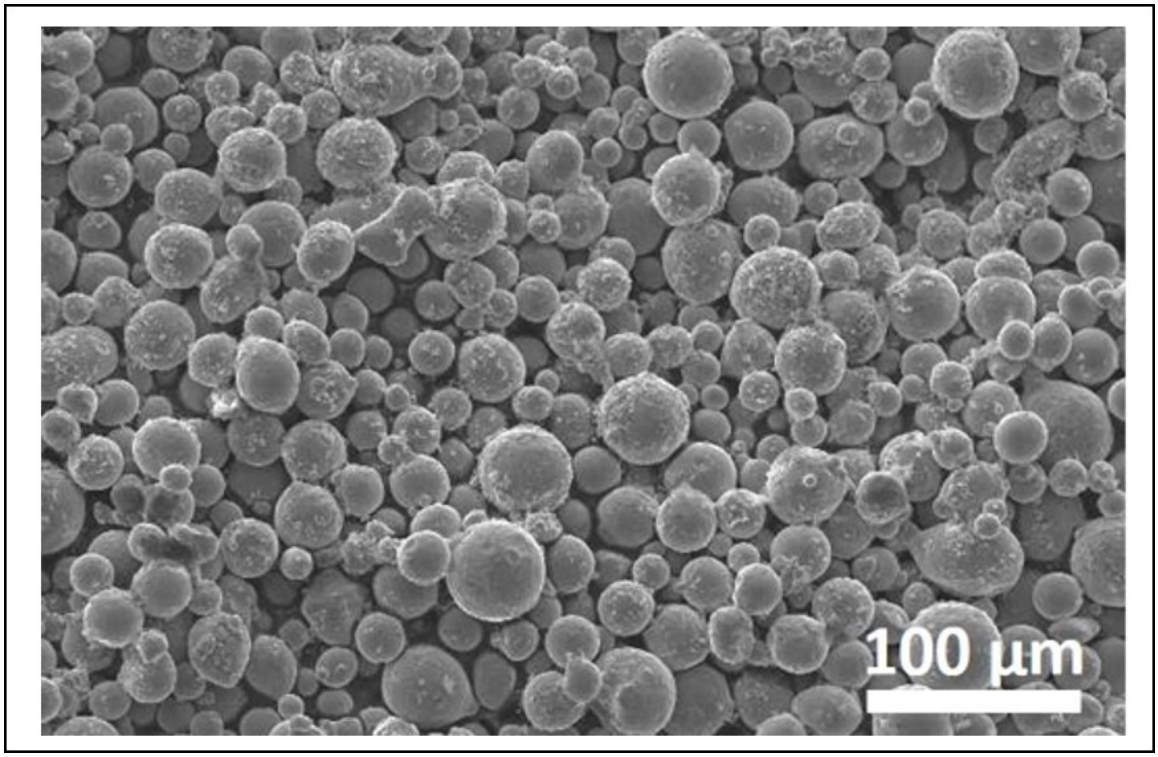


Figure 4.1. SEM image of Stainless Steel 316L powders used for the fabrication of samples.

Referring to optical micrographs of the fabricated samples in Figure 4.2, defects are seen in samples (a), (b), (g), and (j). Voids in samples (a) and (b) are mainly circular. Defects in the samples (g) and (j), are large irregular defects that are the result of lack of fusion and not having sufficient energy in melting. The large irregular defects indicate insufficient layer–layer or track–track bonding [62]. These defects spread unevenly in the 20–250 μm length range in cases (g) and (j) in Figure 4.2. There are some defects in the sample (e), which may not be, in general, related to parameter selection. They could be related to the inert gas trapped in the powder production process, powder bed packing or equipment-related defects such as the deflection of the beam and the calibration error of beam and also insufficiently qualified Galvano mirrors [69].

As cases (a) and (b) show in Figure 4.2, extreme laser power triggers various defects. Powder denudation is one of them, which causes large and grooved defects. Another defect could be spatter that occurs with high energy inputs, and details are provided in Figure 4.2.

Table 4.4. Parameter sets of fabricated samples. A hatch space of 115 μm was used.

Sample	Laser Power (W)	Laser Spot Diameter (μm)	Scanning Velocity (mm/s)
a	150	100	600
b	150	40	900
c	150	130	600
d	150	80	900
e	150	110	900
f	150	160	600
g	150	160	1200
h	130	80	600
i	110	80	600
j	80	80	1400

Spatter occurs when the metal vapor force overcomes the surface tension force and it is difficult to be melted in the next layers; usually spatters are larger than powder size, and would remain as inclusions [70]. Keyholes are one of the most common defects with high energy inputs, which are a result of the vaporization of metal [62]. In cases (a) and (b) of Figure 4.2, the defects are generally in the 35–55 μm range and are typically larger than the powder size. At high energies, crack defects are another defect that is related to high-temperature gradients. Excessive energy input increases cracking ability by decreasing the cracking stress threshold [62]. Two spatters with a total length of close to 100 μm are shown in Figure 4.2 as a result of excessive energy implementation in sample (a). A crack about 50 μm long caused by the same factor in sample (b) is shown in Figure 4.2; also, voids could be observed with a diameter of 30–50 μm with an interlayered morphology. The lines are related to the melt-pool boundaries, and they possibly are the result of high residual stress in the high-speed cooling process. It could encourage the formation of the crack along melt-pool boundaries (Figure 4.3) [27].

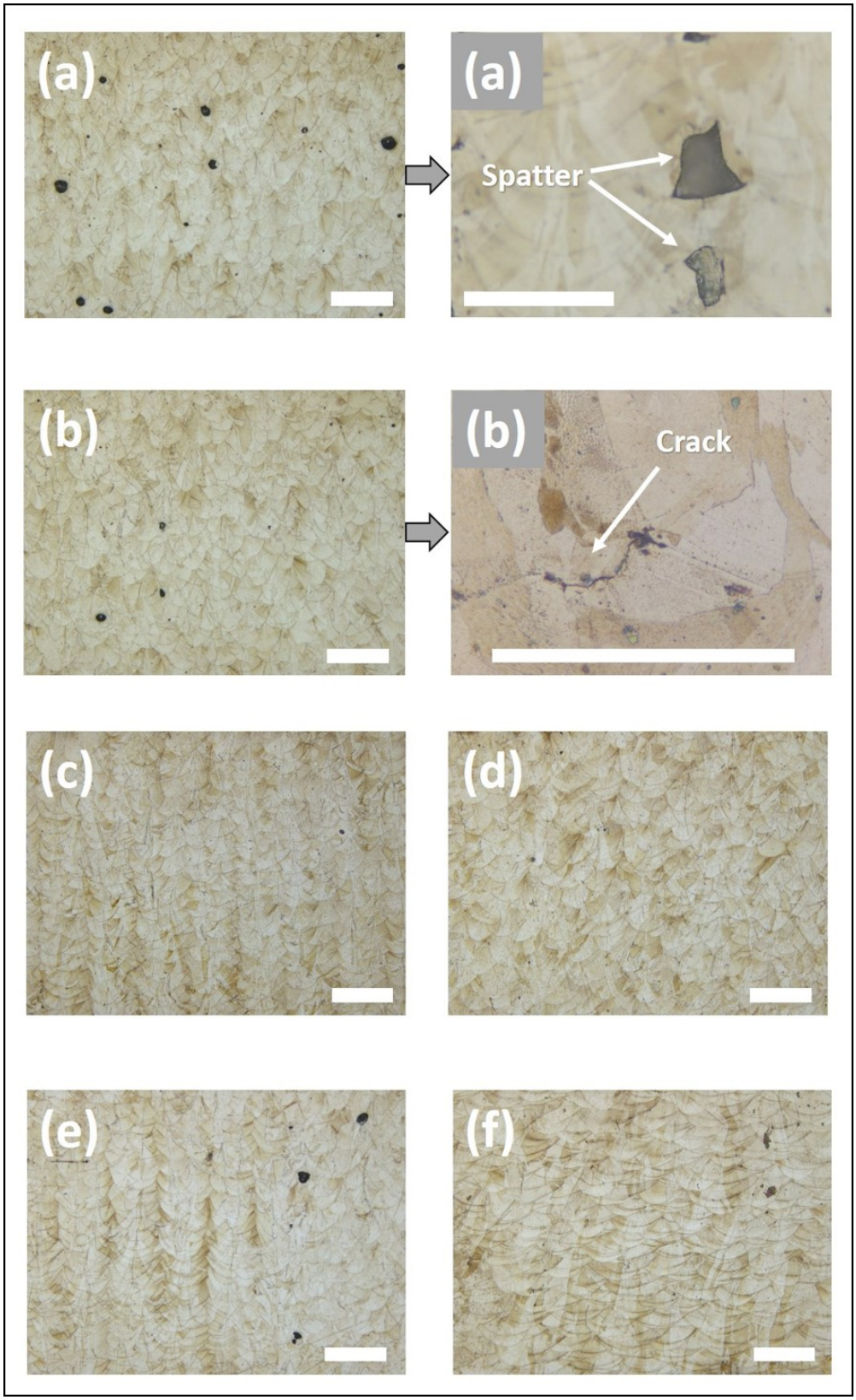


Figure 4.2. Optical micrographs of fabricated samples after etching. Black regions are defects, and the building direction is perpendicular to the plane. The optical micrographs are arranged from sample (a) to sample (j), respectively. Table 4.4 can be consulted for the production parameters of the samples (scale bar: 100 μm).

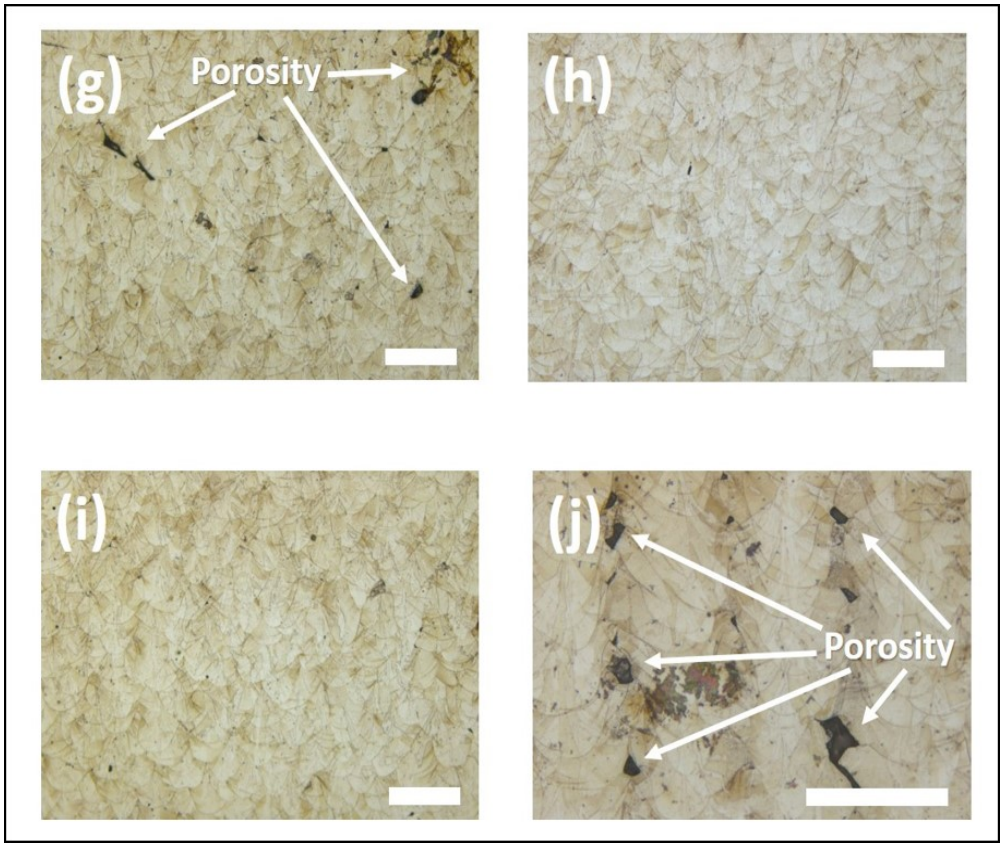


Figure 4.2. (Continue) Optical micrographs of fabricated samples after etching. Black regions are defects, and the building direction is perpendicular to the plane. The optical micrographs are arranged from sample (a) to sample (j), respectively. Table 4.4 can be consulted for the production parameters of the samples (scale bar: 100 μm).

Unmelted regions that belong to the sample (j) are shown more accurately in Figure 4.3. Unmelted powders are evident, and those pores could have two causes. One of them is the lack of sufficient energy to melt them, and another reason is the balling. The balling is the agglomeration of powders to minimize the surface energy due to high viscosity or high wetting angle of the molten track [27]. Regarding the selected parameter set for the fabrication of sample j and Figure 4.3, in this case, the reason for the phenomena is insufficient laser energy to melt powders. There are some other defects which may not depend on the parameters of fabrica-tion, and could probably occur during any fabrication parameters. One of them is gas bubbles, which are entrapped in the melt. Another common defect is due to reusing powder from the previous fabrications [22][24][62][27][71][72] [73][30][74][75].

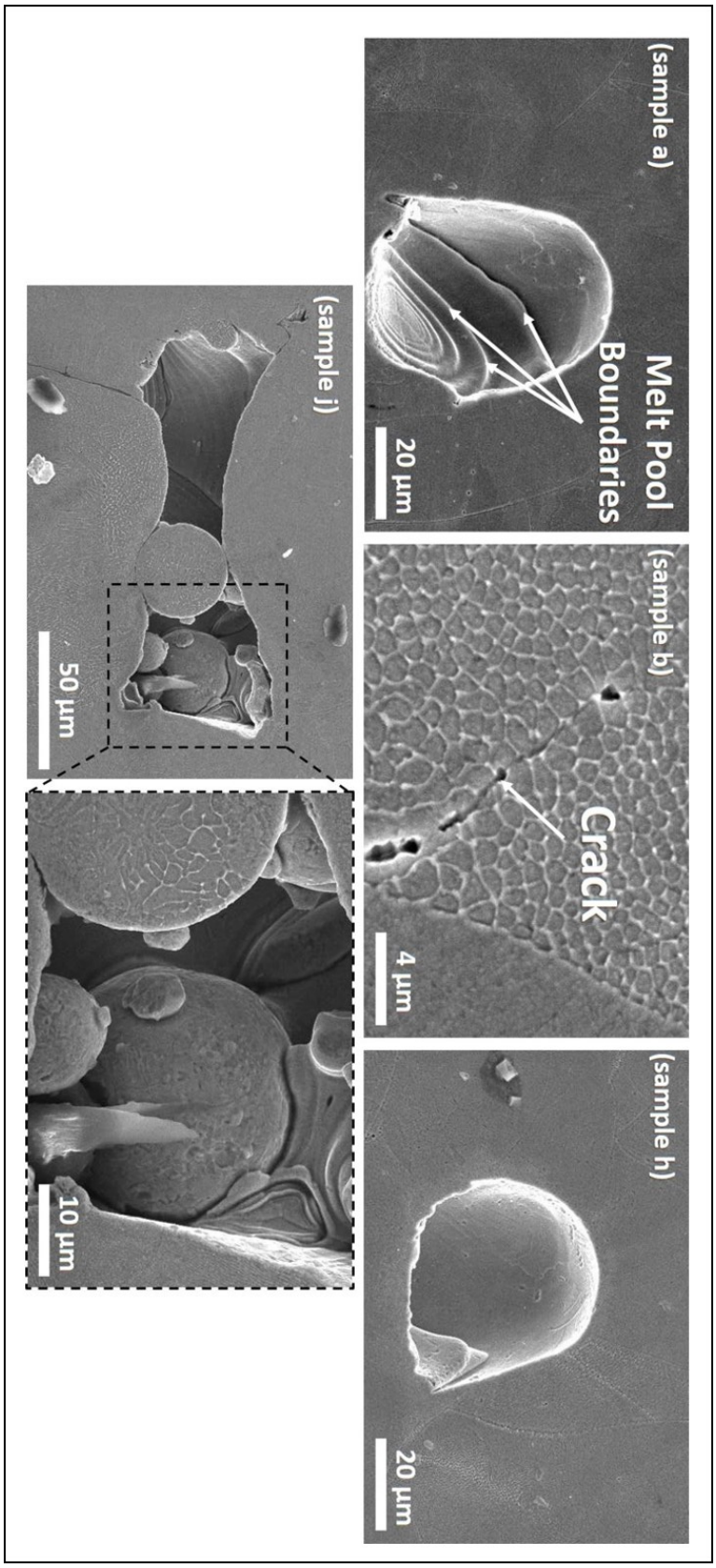


Figure 4.3. SEM images of defects: void with melt-pool boundaries in the sample (a), a crack in the sample (b), entrapped gas pore in the sample (h), unmelted powders in the sample (j).

The samples of (c), (d), (e), (f), (h), and (i) have minimum defects and are almost clean. These samples have parameter sets located in the area between the melting and evaporation lines in the diagram of the simulation results. Their SEM images show favorable structures (Figures 4.4 and 4.5). Reflection of SEM images of experimental results on simulation results is shown more conveniently in Figures 4.4 and 4.5. It is also important to note that the melt-pool lifetime, the duration in which the powder melts and eventually solidifies, is a determinative factor in the melting process. Insufficient lifetime could result in incomplete melting and insufficient wetting of neighboring powders. It hinders the melting phase to propagate. Consequently, this inability will weaken melting the powders to ensure the stable and continuous melt-pool and satisfy hatch space. Sample (g) could be an example of this phenomena. Although the relative temperature for the parameter set of this sample is approximately on the melting temperature line, nevertheless there are unmelted powders in its microstructure. Based on the few previous sentences, most likely, these unmelted powders are a result of an insufficient lifetime (47 μs based on the simulation for sample (g)) of the melt-pool). Due to this issue, the area near the melting temperature line is a delicate area for the process fluctuations and therefore should be avoided for a guaranteed result. Appearance of the lack of fusion defects in samples (g) and (j) with energy densities of 19 J/mm^3 and 18 J/mm^3 and relevant temperatures near to the melting point, reveals that process parameters should be selected outside of this insecure area. Process parameters that result in a temperature of more than almost 2000 K and an energy density above 35 J/mm^3, and also do not exceed the evaporation temperature, will be safe and will allow adequate melt-pool temperature, life-time duration and, as a result, a high-density final product.

Compared with the energy densities reported for producing Stainless Steel 316L in the literature, in which Yusuf et al. [76] reported 42 J/mm^3, Spierings and Gideon [77] reported 33 J/mm^3, and Li et al. [78] reported 42 J/mm^3, the abovementioned milestones show acceptable conformity.

Additionally, the corresponding energy density to the standard parameter set that the Concept Laser company has given for the machine employed for the experimental study here is 42.9 J/mm^3.

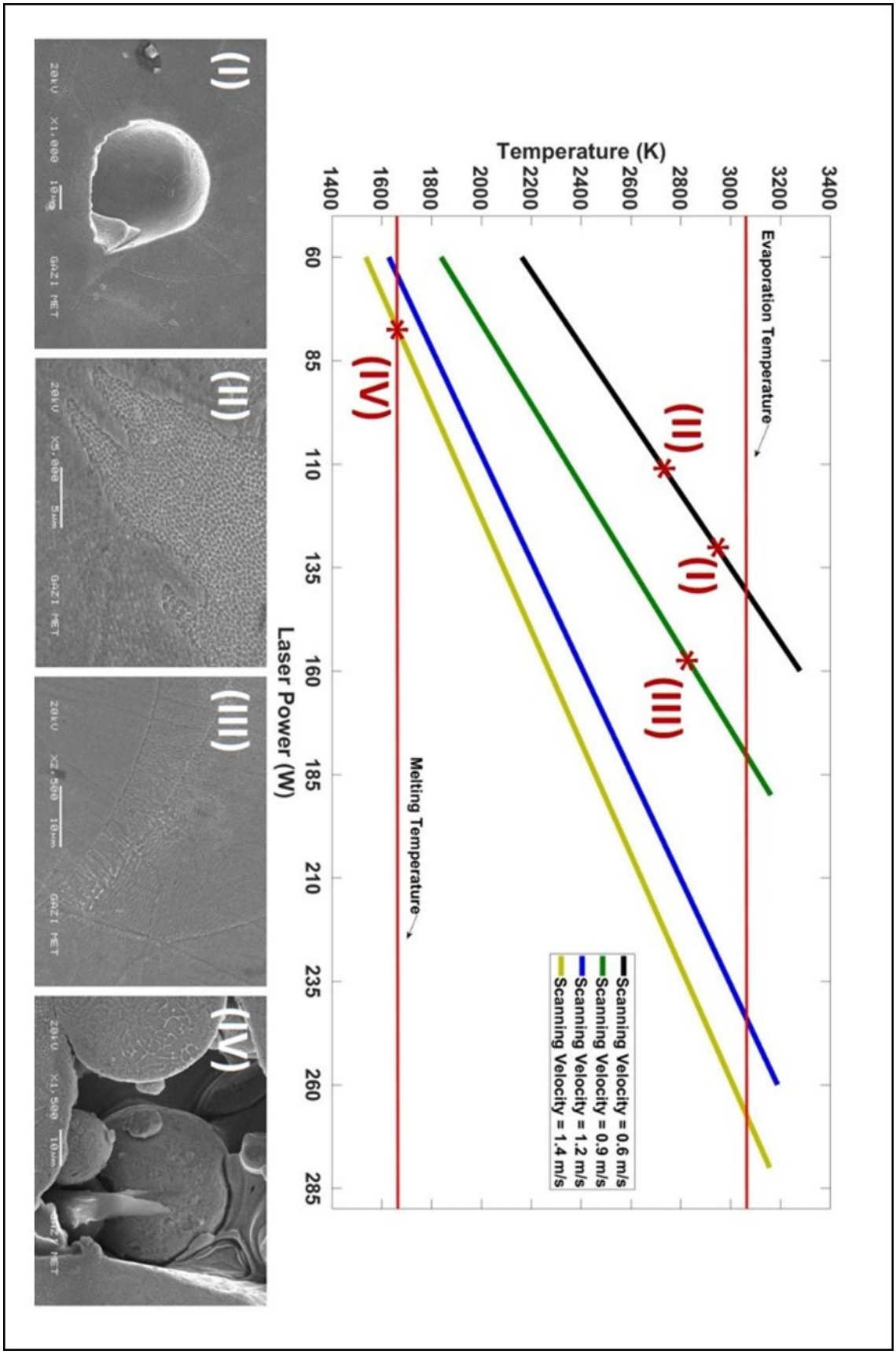


Figure 4.4. Reflection of SEM images of experimental results on simulation results with a laser spot diameter of 80 μm.

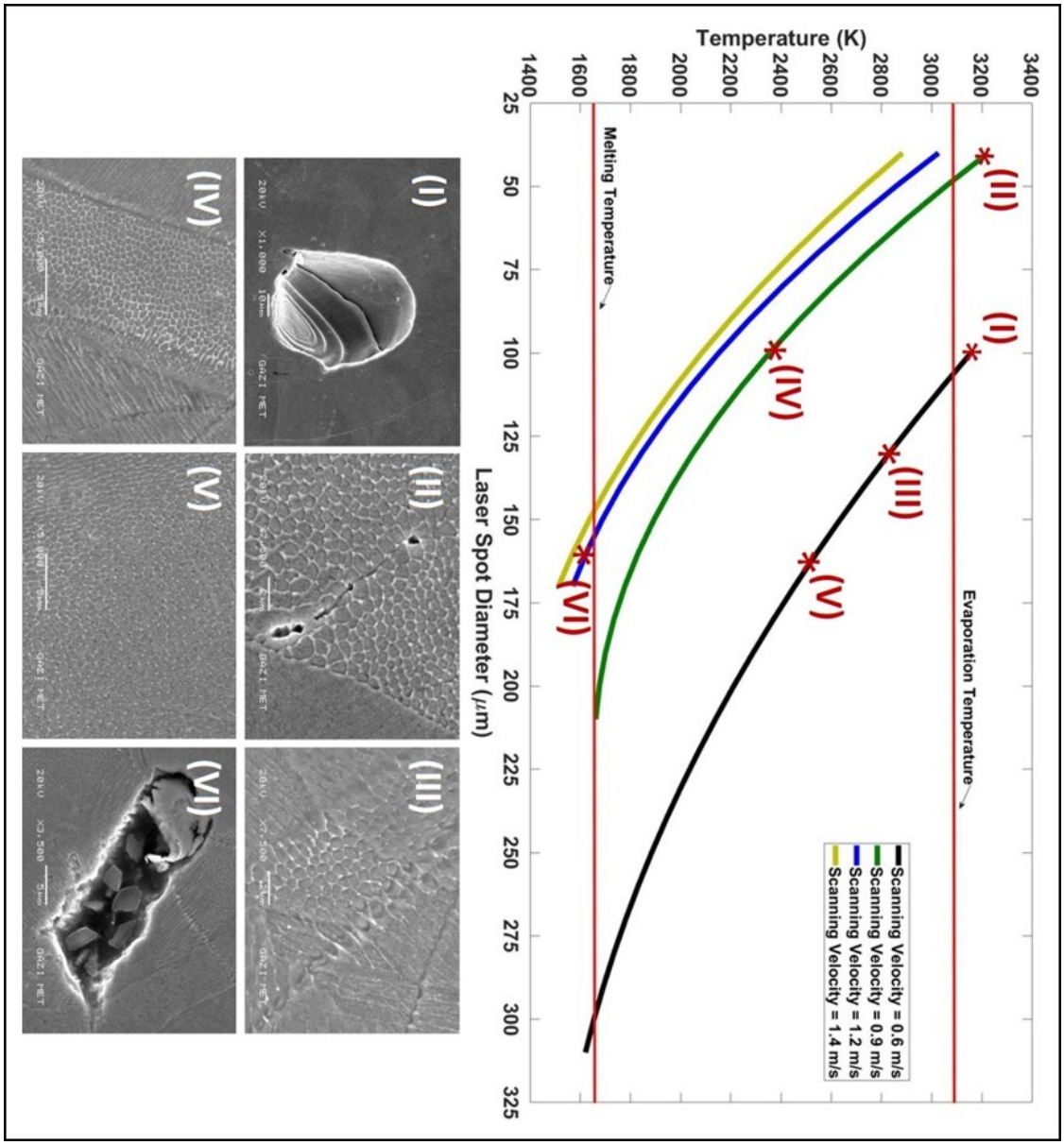


Figure 4.5. Reflection of SEM images of experimental results on simulation results with a laser power of 150 W.

4.2 AlSi10Mg

Comprehensive experimental work was done to validate the model and simulation results. The gas atomized AlSi10Mg powders of Concept Laser company were used in fabrication. The powder composition and powder size distribution are shown in Tables 4.5 and 4.6, respectively, referring to the data sheet. Also, Figure 4.6 shows SEM image of the powders.

Table 4.5. Chemical composition of AlSi10Mg powder [79].

Element	Al	C	Cu	Fe	Mg	Mn	Ni
Mass.-%	Rest	< 0.005	< 0.03	0.13	0.38	< 0.03	< 0.03
Element	O	Pb	Si	Sn	Ti	Zn	-
Mass.-%	0.114	< 0.03	10.3	< 0.03	< 0.03	< 0.03	-

Table 4.6. Powder size distribution of AlSi10Mg powder by light scattering as per ASTM B822 [79].

Size	D10 (µm)	D50 (µm)	D90 (µm)	< 5 (µm)
Minimum	5	26	45	–
Maximum	15	36	55	%10

The temperature-dependent [66] and constant material properties [18] and also evaporation data [80] used for AlSi10Mg in the simulation are listed in the Table 4.7. The absorption coefficient of bulk metal and powder metal is different. The difference has to do with reasons for which multi- reflection is one of the most important. The laser beam is reflected from one powder to another, while it does not occur in bulk metal.

Table 4.7. Material Properties of AlSi10Mg [18] [66] [80].

Material property	Symbol	Value	Unit
Melting Temperature	T_m	867	K
Melting Interval	δT	± 10	K
Evaporation Temperature	T_{ev}	2743	K
Latent Heat of Melting	H_m	4.23×10^5	J/kg
Latent Heat of Evaporation	H_{ev}	1.07×10^7	J/kg
Density	ρ	2670	kg/m^3
Thermal Conductivity	k	$113 + 1.06 \times 10^{-5} T$	$W/m.K$
Specific Heat Capacity	C_p	$536.2 + 0.035T$	$J\ /\ kg.K$
Marangoni Coefficient	$d\gamma/dT$	-0.35×10^{-3}	$N\ /\ m.K$
Absorption Coefficient	A	$0.6\ (solid) - 0.3(liquid)$	–

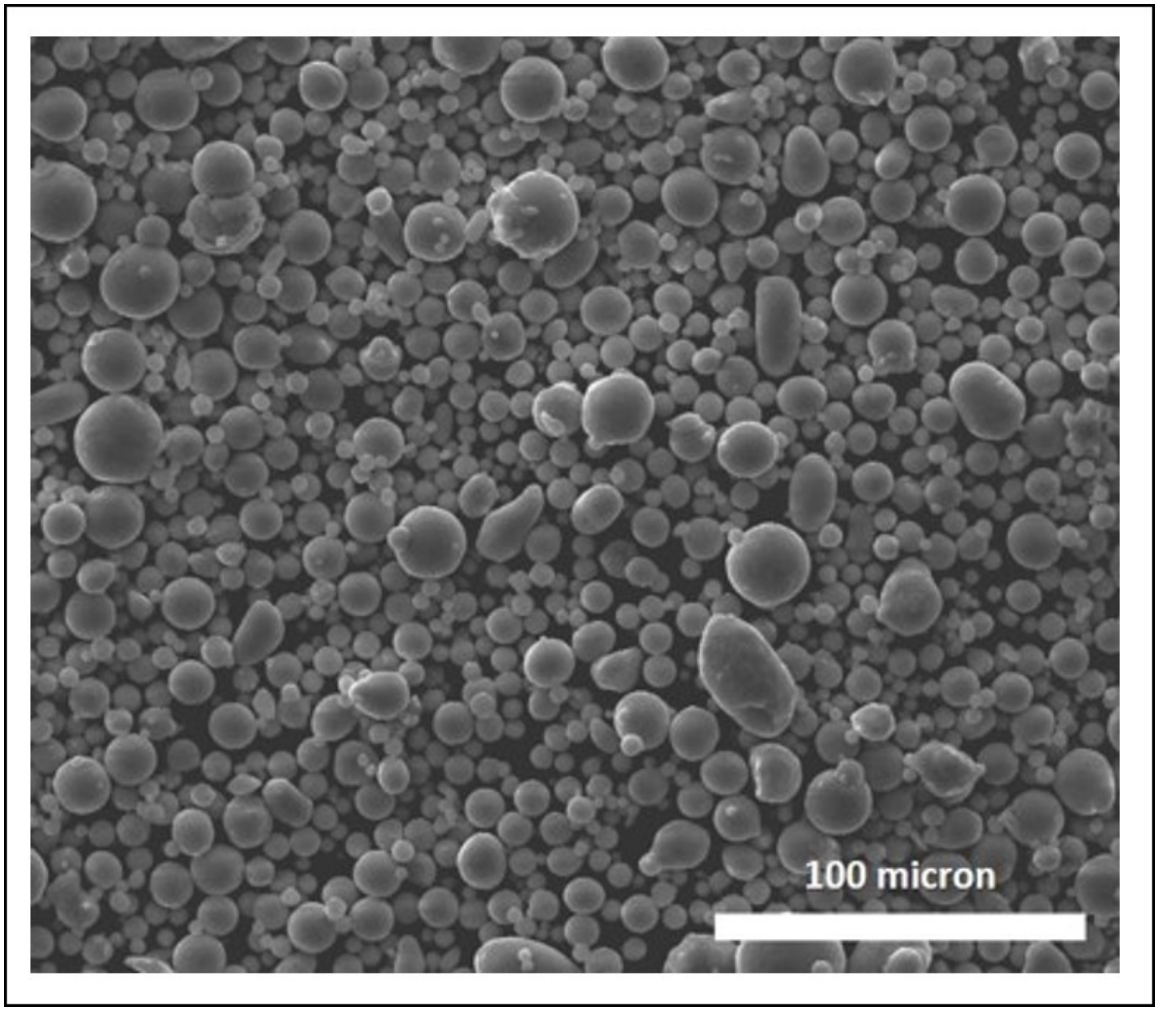


Figure 4.6. SEM image of AlSi10Mg powders used for the fabrication of samples.

Two sets of nineteen test specimens, each for microstructure and tensile behavior study, were fabricated using simulated process parameter sets shown in Figures 3.12 and 3.14. The parameters were selected in three types: insufficient (“sensitive” gray box area), sufficient (between the melting and evaporation lines and outside the gray box) and excessive (above the evaporation line) for melting the AlSi10Mg powders. Defects such as un-melted, low melted, and nonconnected melt pools, and low tensile properties as a result of these defects, are expected at insufficient process parameters in the “sensitive” gray box area. Also, defects such as spatters and holes and their effect in a bad way on tensile properties are expected to be noted at parameters that are excessive as a result of the evaporation of metal powders above the evaporation line. With sufficient parameters, between the melting and evaporation lines and outside the gray box, a smooth and perfect microstructure is expected, except for general defects. There may be some general defects, such as air bubbles-defects relating to the cutting and etching process, that are not dependent on the process parameters and can

occur in any parameter. Table 4.8 shows the parameter sets used to fabricate nineteen test samples.

Table 4.8. Parameter sets of fabricated samples.

No.	Scanning Velocity (m/s)	Laser Spot Diameter (μm)	Laser Power (W)
1	0.6	50	140
2	0.6	140	400
3	1.4	140	85
4	1.1	225	140
5	0.8	140	100
6	0.6	250	140
7	1.4	150	140
8	1.1	140	160
9	0.6	140	300
10	0.6	140	225
11	1.1	140	275
12	1.4	140	350
13	0.6	125	140
14	0.8	80	140
15	1.1	100	140
16	1.4	60	140
17	0.8	140	350
18	0.6	75	140
19	0.8	140	200

4.2.1 Microstructure

The optical micrographs in Figure 4.7 thoroughly confirm the numerical model. Referring Table 4.8 and the position of the parameters in Figures 3.12 and 3.14 the micrographs could be explained.

Samples (1) and (2) were chosen above the evaporation temperature line respectively in

Figures 3.12 and 3.14 and contain melt and vapor metal, as a mixture, due to the excessive energy input. Applying excessive energy causes various defects. The most noticeable defects are holes and spatters which are the result of metal evaporation [62] and high-temperature gradients [27]. Circular defects are visible in relating samples in Figure 4.7 [62]. Referring to the simulation results (Figures 3.12 and 3.14), Samples (9) - (19) were fabricated using the parameter sets located in the region between the melting temperature and evaporation temperature lines and outside the gray box. This is a suitable region for production as it results in sufficient heat and energy. Some common defects may appear in these areas. These defects could be due to the process of cutting sample to examine the microstructure, reuse of powders or the presence of O_2 (maximum % 0.4) in the fabrication chamber. The presence of O_2 could be appeared as gas bubbles in the microstructure and also could lead to oxidation of the AlSi10Mg powders and come up as defects in the microstructure [81]. The parameter sets for samples (3) - (8) were selected near the melting point temperature line and inside the gray box. As a result, they were predicted to have un-melted powders and melt pools not sufficiently bonded (due to low melt pool life-time; with reference to simulations: 279(μs), 250(μs) and 380(μs) respectively for samples 5, 7 and 8). The large irregular defects express insufficient layer-layer or track-track bonding in absence of enough energy and fusion which are clearly visible in Figure 4.7 [62]. The SEM images of the smooth microstructures and major defects mentioned above are shown in Figure 4.8.

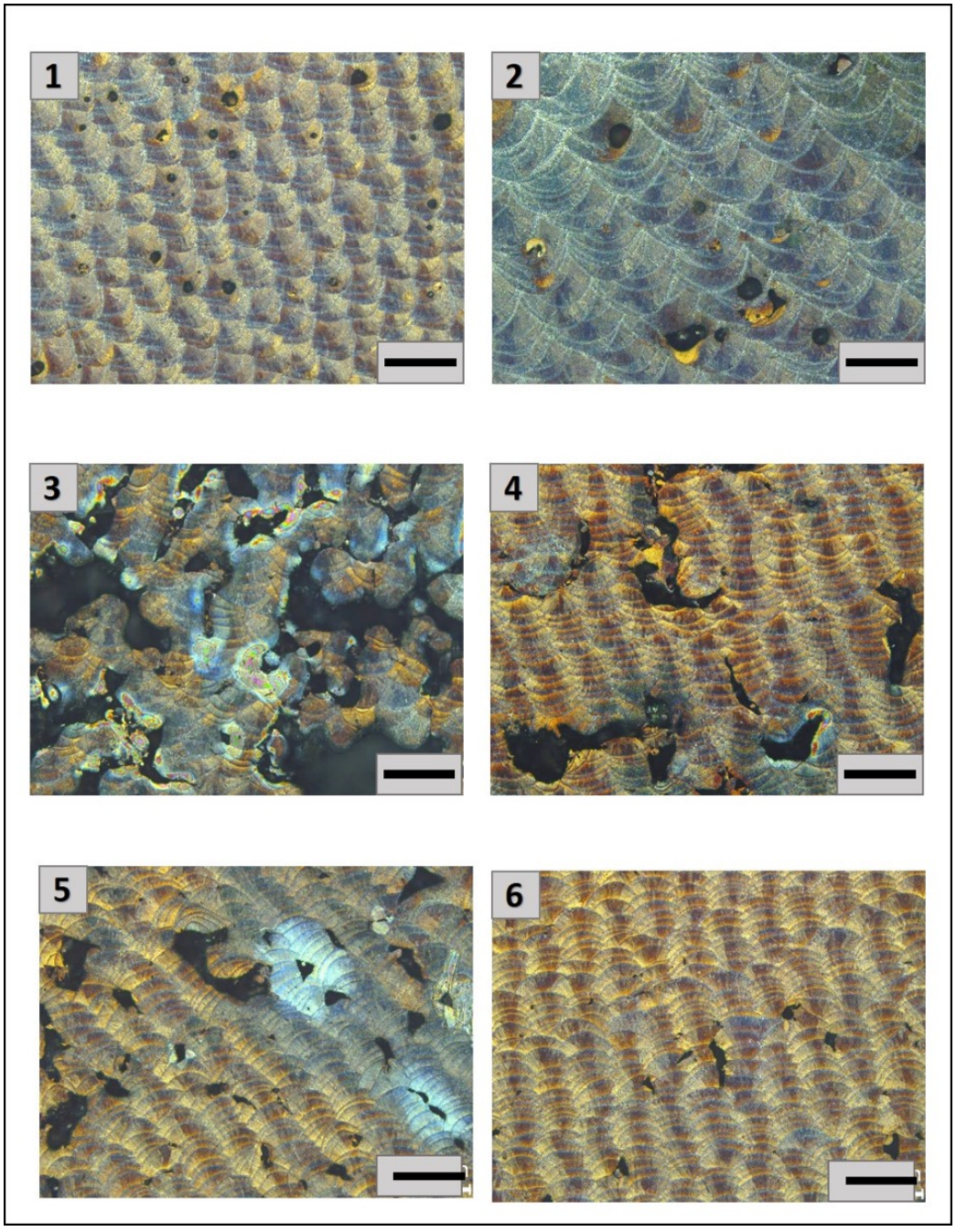


Figure 4.7. Optical micrographs of fabricated samples. Black regions are defects and the building direction is perpendicular to the plane. The optical micrographs are arranged from sample (1) to sample (19), respectively. Table 4.8 can be consulted for the production parameters of the samples. (Scale bar:200(μm)).

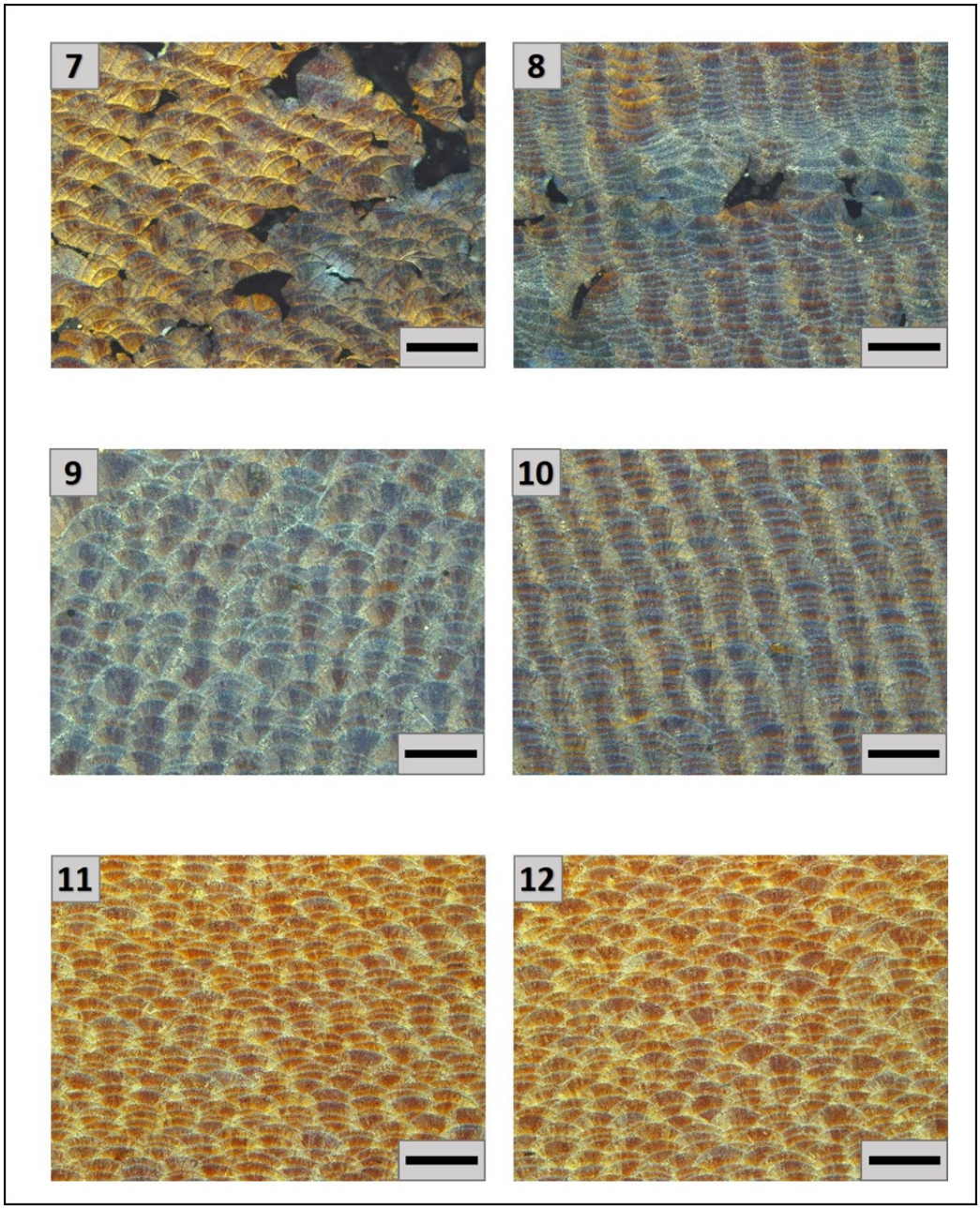


Figure 4.7. (Continue) Optical micrographs of fabricated samples. Black regions are defects and the building direction is perpendicular to the plane. The optical micrographs are arranged from sample (1) to sample (19), respectively. Table 4.8 can be consulted for the production parameters of the samples. (Scale bar:200(μm)).

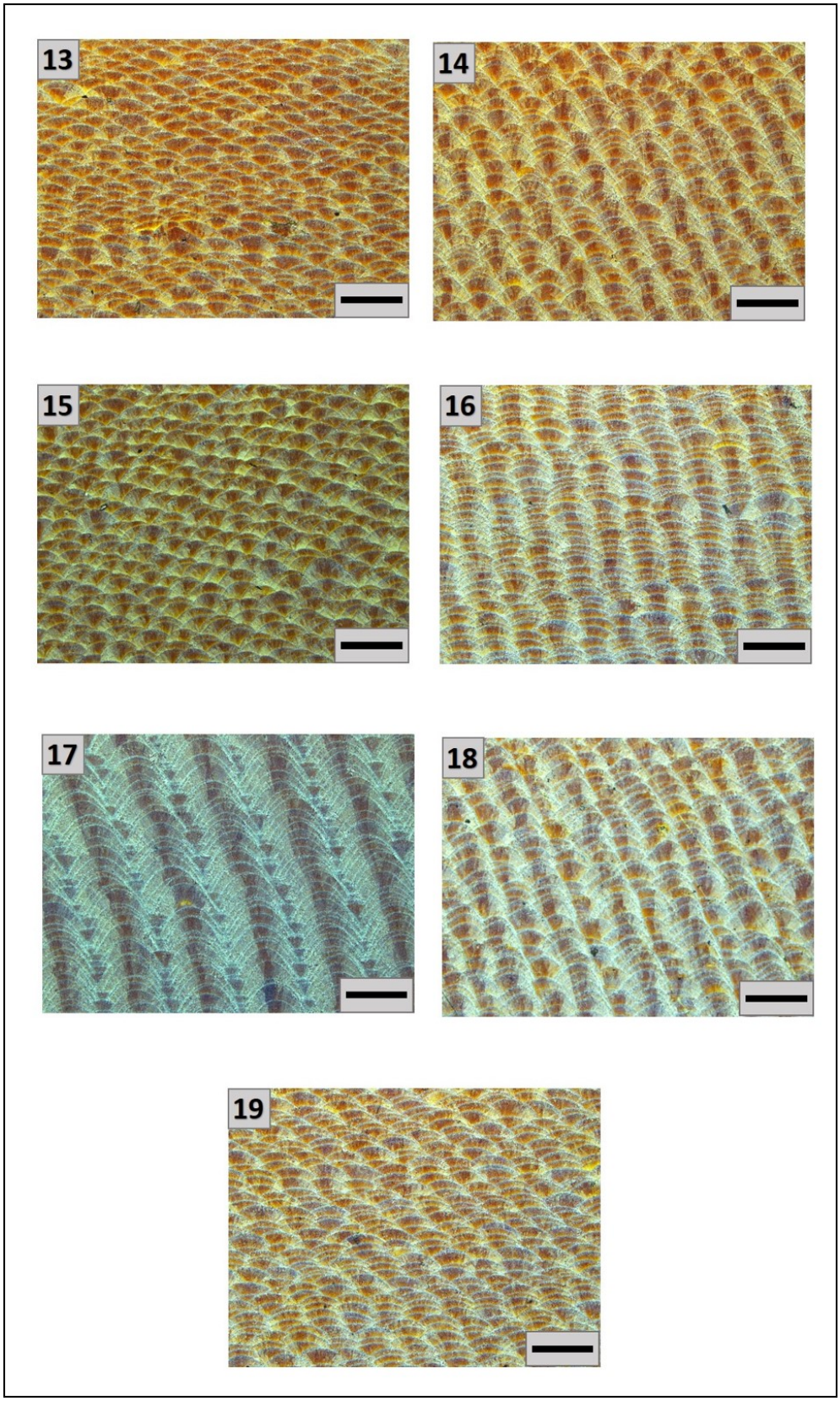


Figure 4.7. Optical micrographs of fabricated samples. Black regions are defects and the building direction is perpendicular to the plane. The optical micrographs are arranged from sample (1) to sample (19), respectively. Table 4.8 can be consulted for the production parameters of the samples. (Scale bar:200(μm)).

In order to explain more effectively the distribution of the produced samples on simulation graphs and to examine the microstructure of the samples fabricated according to the simulated parameter regions more conveniently, the SEM images of the samples were reflected on the simulation results in Figures 4.9 and 4.10. In the samples that locate above the evaporation line, hole defect is shown. In the areas close to the melting line, within the gray box, un-melted powders and nonconnected melt pools are obvious. Suitable structures have been obtained as a result of production with sufficient parameter sets in the middle regions.

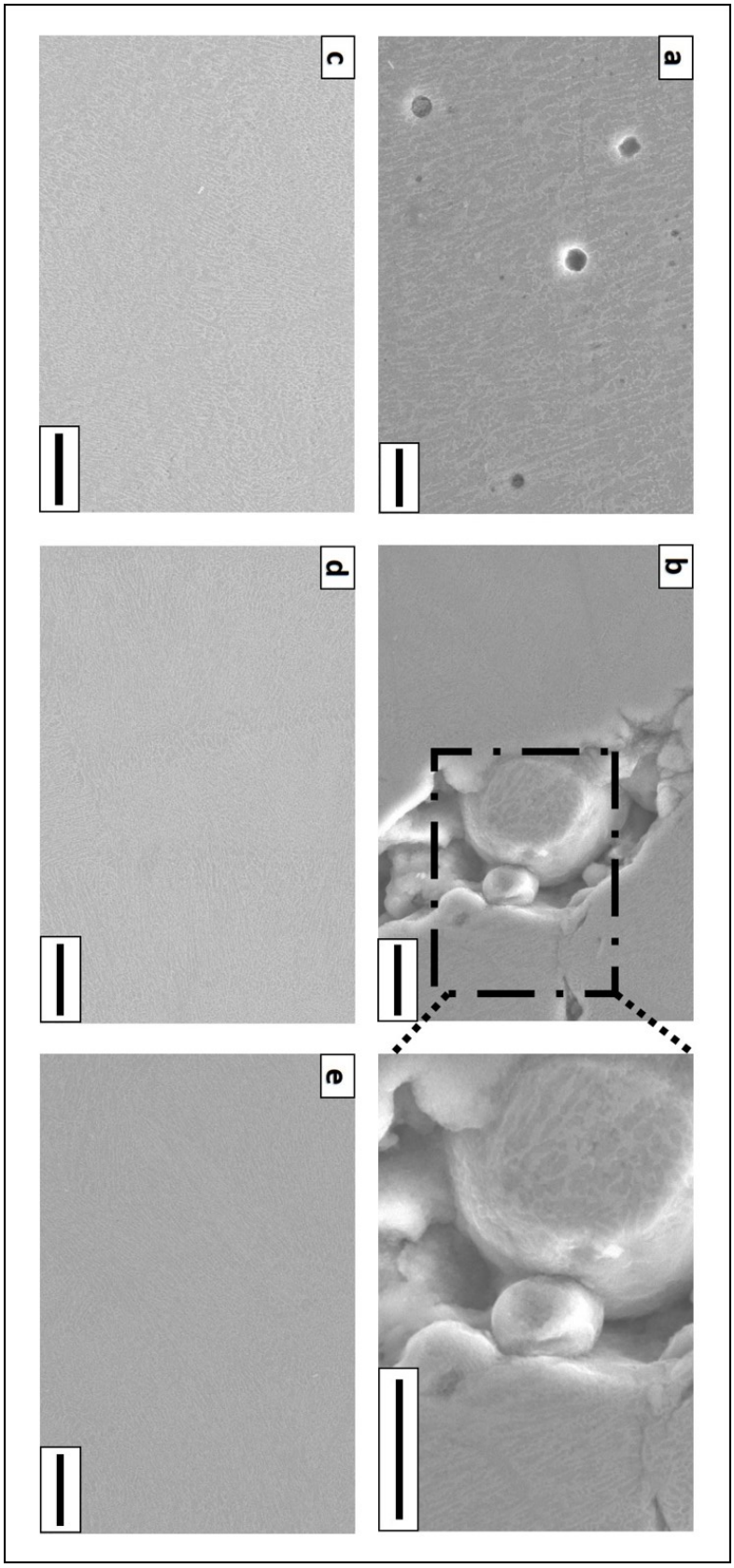


Figure 4.8. SEM image of: (a) hole defect in sample (1), (b) un-melted powder defect in samples (3) and (c), (d), (e) smooth microstructure in samples (10), (15) and (19). (Scale bar:10 μm).

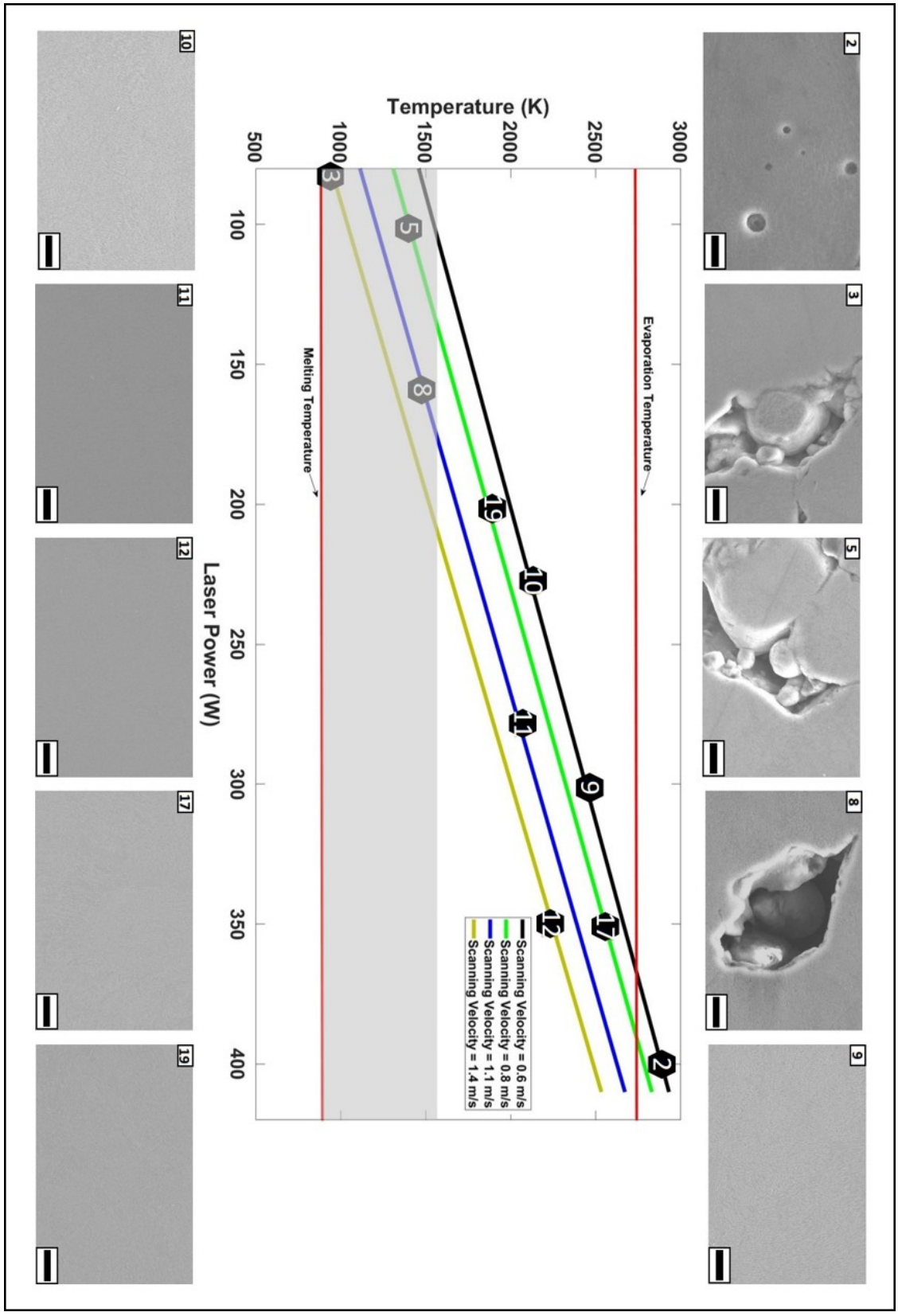


Figure 4.9. Reflection of SEM images of experimental results on simulation results with a laser spot diameter of 140 µm. (Scale bar:10 µm).

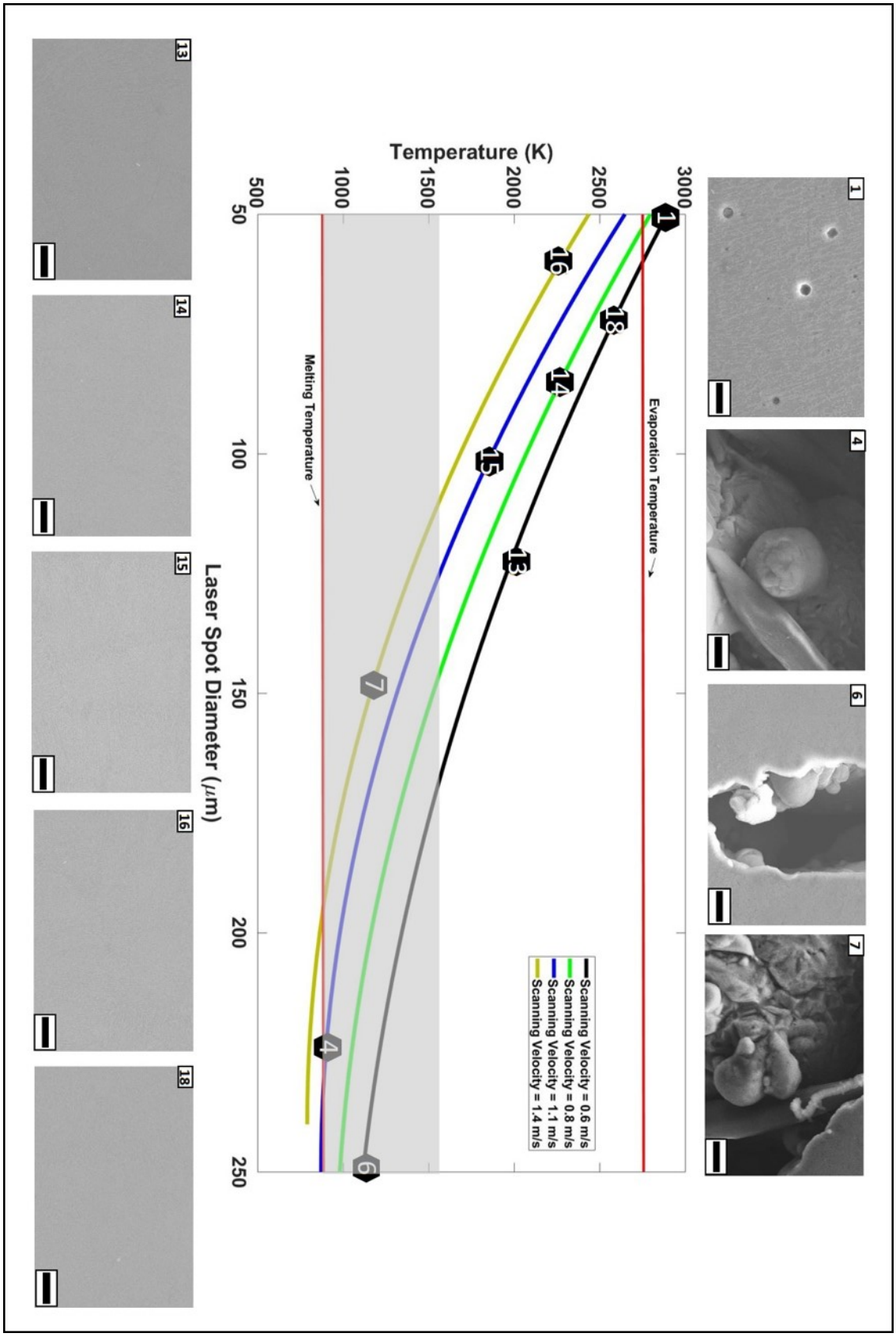


Figure 4.10. Reflection of SEM images of experimental results on simulation results with a laser power of 110 W. (Scale bar:10 μm).

4.2.2 Tensile behavior

Regarding the parameter sets in Table 4.8, nineteen rod-shaped tensile test samples were fabricated and prepared by machining in accordance with ASTM standard [57]. Because the process parameters of samples (3) and (7) were insufficient and therefore had an unstable structure, they became unusable during machining and tensile tests could not be performed on them. For the same reasons, the (4), (5) and (8)'th samples were directly broken during the tensile test and the Yield stress of these three samples could not be measured. The tensile tests were performed by 100kN Instron electromechanical device and the results are presented in Figure 4.11. As predicted by the developed mathematical model, the samples fabricated with the process parameters located in the sensitive region (gray box), the region near the melting temperature with a low life-time, show low and poor tensile properties arising from the defects in the part. Referring Figures 4.11 and 4.12, the parameter sets that are located in the region between melting and evaporation temperature line and out of the gray box show acceptable tensile properties. The samples in the gray box show poor properties and they break off at the slightest tension application. Also, the mechanical properties of samples (1) and (2), the samples above the evaporation temperature line, decreased compared to the samples remaining in the middle area due to the defects occurring as a result of evaporation. The tensile test outcomes confirm well the results predicted by the simulations.

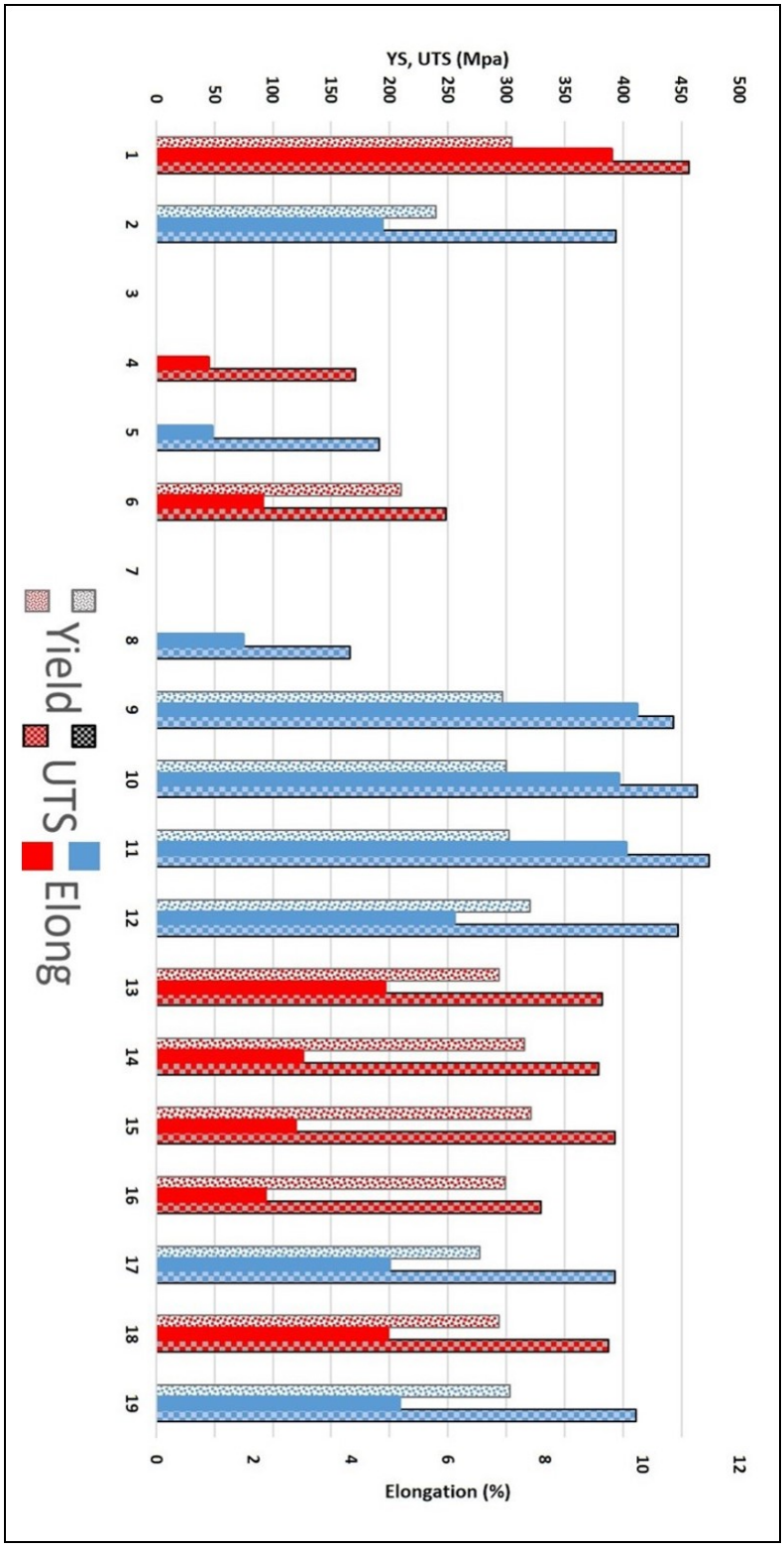


Figure 4.11. Tensile properties of SLM fabricated AlSi10Mg samples fabricated by the parameters given in Table 4.8. The blue-colored samples have a laser spot diameter of 140 μm with different laser powers and speeds, while the red-colored samples have a laser power of 110 W with different laser spot diameters and velocities.

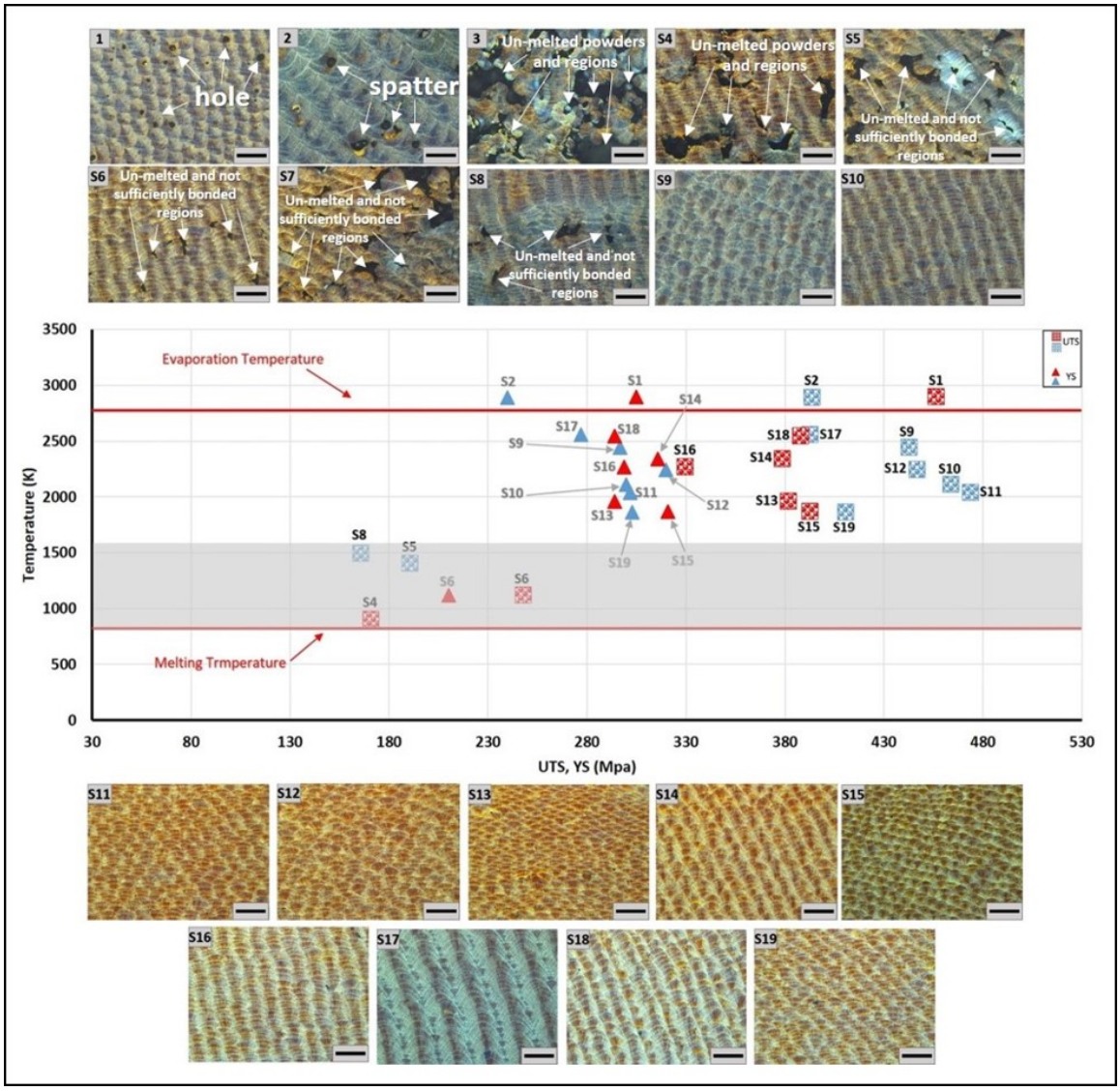


Figure 4.12. UTS and YS distribution of the samples versus the temperature including microstructure details. The blue-colored samples have a laser spot diameter of 140 μm with different laser powers and speeds, while the red-colored samples have a laser power of 110 W with different laser spot diameters and velocities (Scale bar:200 μm).

Figure 4.13 shows the fracture surface of samples found in various areas of the simulation results (Figures 3.12 and 3.14). Holes are evident in the sample (2) as a result of metal evaporation. In addition, heat cracks formed as a result of excessive melting are also potential causes of failure. Un-melted powders and non-connected melt pools are clearly visible in sample (5) as a result of the insufficient process parameter. Numerous circular voids ranging in size from 10-150 μm are evident as solidification defects (pores and cavities) related to lack of fusion. It leads to the lower density of samples and strongly reduces the mechanical properties of the final part [3]. As a result of the existence of these

low density and weak zones surrounding each melt-pool, they will be pulled out leaving crater-like voids on the fracture surface during tensile tests [82]. The cracks of the deformation that occur in the tensile test are caused by such defects, which cause stress concentration and result in failure [27]. The fracture surface of the samples (12) and (19) are typical of ductile failure. They present a ductile fracture view with typical submicron-sized dimples and brittle fracture properties.

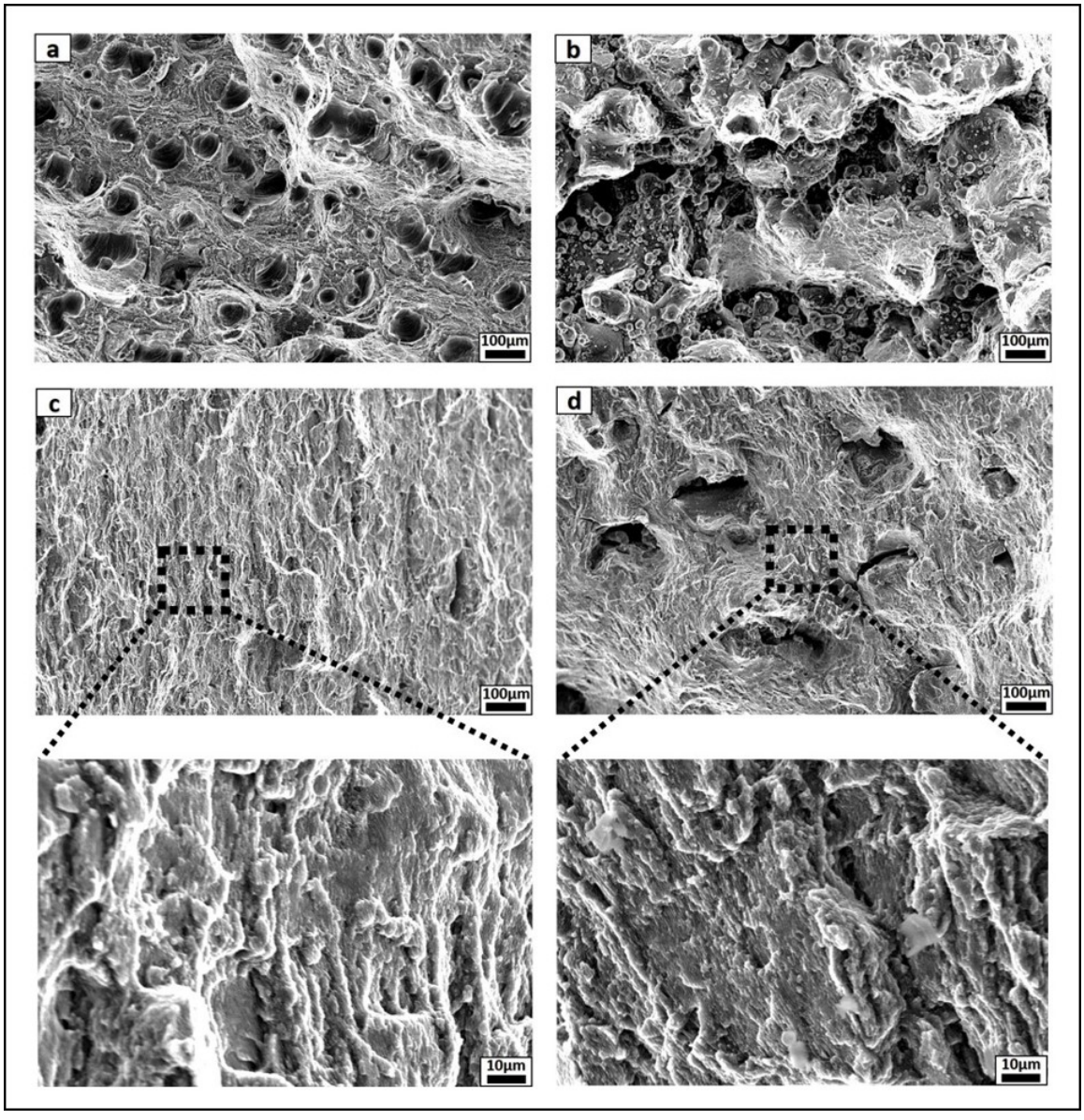


Figure 4.13. SEM images of the fracture surfaces of: (a) sample 2, (b) sample 5, (c) sample 12 and (d) sample 19.

Referring to the results available in the literature, they show very good conformity with

them. Wu et al. [83] investigated 3-D printed AlSi10Mg samples according to the applied energy density. They reported nearly full dense structure at applied energy densities in the 35 J/mm³ - 75 J/mm³ range. In addition, they reported that during the application of energy densities above the range, the defects caused by evaporation, affect the microstructure and mechanical properties of the part in a bad way, and the quality decreases. In another study, Wu et al. [84] introduced the melting of AlSi10Mg powder in the SLM process with three types of models; "conductor mode, transition mode, and keyhole mode" that depend on energy density. While the samples produced by applying an energy density of 30 J/mm³ - 65 J/mm³, corresponding to the conductor mode and the transition mode, show an acceptable mechanical behavior, the mechanical properties of the samples produced by exceeding this range (keyhole mode) decrease due to the defects caused by the evaporation of the powder. These outcomes confirm the developed model validity and simulation results. By referring to the simulation results, as depicted in Figures 3.12 and 3.14, the middle area of the graphs, the potential area for appropriate process parameters, captures process parameters that fall in the energy density range of about 30 J/mm³ – 90 J/mm³. Similarly, when this region is exceeded, microstructure and mechanical properties decrease as a result of evaporation.

5. AN IMPROVED MATHEMATICAL MODEL WITH PHASE FIELD PHYSICS

Fluid flow is controlled by the Navier-Stokes equations, which solve fluid velocity and pressure fields throughout the modeling domain. Fluid properties (viscosity and density) are either constant, or change relatively smoothly in space as a function of temperature, pressure, shear rate, and so on. However, if two immiscible fluids would be modeled, the properties of the fluid will be significantly different at the interface between the two fluids, and the effects of surface tension as well as the effect of contact angles on wet walls can be important. To model this in COMSOL Multiphysics, the Level Set or Phase Field methods could be used. Both methods introduce an additional scalar field (the level set or phase field function) into the modeling domain. These scalar fields vary everywhere between -1 and +1 and are used to define the viscosity and density of the fluid in the Navier-Stokes equations. The transition (in which the fields vary from 0 to 1 for the level set and -1 to +1 for the phase field) is fairly abrupt in space, so it offers a good resolution of the two phases. The governing equations for the Level Set and Phase Field methods are a kind of convection-diffusion equation, with the adjective term from the Navier-Stokes equations. However, solving such equations is quite challenging numerically, as it is a combination of significant advective term, fairly abrupt transition in the field, and strong coupling to the Navier-Stokes equations. If chamber gas is added to the simulated model using phase-field physics, besides more realistic modeling of the melting process, the gas-melt interface will be simulated and the melt pool surface, melt front, and fluid flow will be simulated. For this, the model was improved and phase-field physics was added to the model. Following sections described the improved and revised model and results.

5.1. Governing Equations of Improved Mathematical Modeling

The interaction between laser beam, metal powder, and shielding gas results in phenomena in which the most significant ones are melting, solidification, evaporation, and earlier described mushy zone. To model these phenomena in the simulation three physics of heat transfer, laminar flow, and phase field physics were coupled and a multiphysics simulation was done. In addition, the powder layer is modeled as multi-layers to comprehensively explain the role of conductive and convective heat transfer and fully demonstrate the heat

and melt dissipation. The powder diameter was assumed 30 μm here. Figure 5.1 shows the improved model details. Through the modeling, the fluid flow was assumed as a laminar flow to satisfy the convergence. Also, the multi reflection and shadowing effects were ignored.

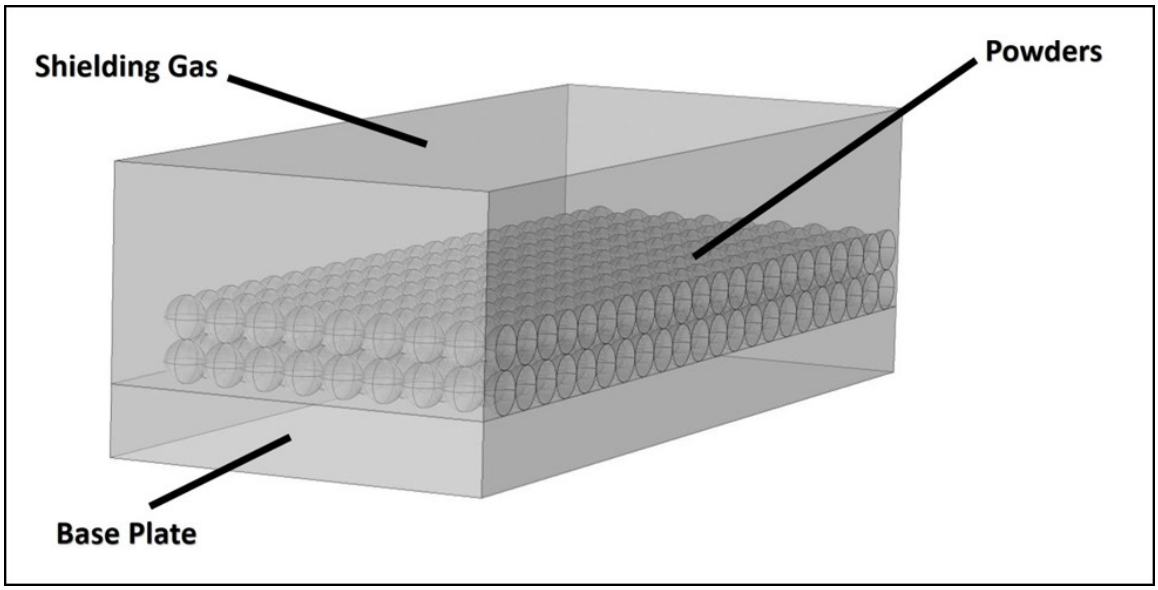


Figure 5.1. Details of the improved model, including shielding gas, double layer powder and base plate.

The heat transfer equation (energy equation) is as,

$$\rho C_p^* \frac{\partial T}{\partial t} + \rho C_p^* u.\nabla T = \nabla.(k\nabla T) + \Pi A Q_{Laser} - \Pi Q_{Rad} - \Pi Q_{ev} \quad (13)$$

where ρ, C_p^*, T, t, u, k, A, Π, Q_{Laser}, Q_{Rad}, and Q_{ev} are density (kg/m^3), modified specific heat capacity $(J/kg.K)$, temperature (K), time (s), velocity (m/s), thermal conductivity $(W/(m.K))$, interface function $(1/m)$, absorption coefficient (-), input laser energy source (W/m^3), radiated energy source (W/m^2) and evaporation heat loss (W/m^3) respectively. The laser beam is modeled as a moving Gaussian distributed heat source on the powders. Shadowing effect, multi-reflection, and beam angle effect on the absorption of the laser are neglected [48].

The mechanics of the fluid in the model are described by the Navier-Stokes equation as follows:

$$\rho\left(\frac{\partial u}{\partial t}+u(\nabla.u)\right)=\nabla.[-pI+\mu(\nabla u+(\nabla u)^T)]+\rho g+F \quad (14)$$

where p, I, μ, $(.)^T$, g, and F are pressure (N/m^2), identity matrix, viscosity $(Pa.s)$, transposed matrix, gravity (m/s^2) and volume force (N/m^3), respectively [13]. The volume forces were illustrated earlier.

To satisfy the conservation of the mass the continuity equation is assumed as following by adding a source term $(1/s)$,

$$\nabla.u=Q_s \quad (15)$$

$$Q_s=m^{\bullet}\Pi(\frac{1}{\rho_{vap}}-\frac{1}{\rho_{met}}) \quad (16)$$

where Q_s, ρ_{vap}, and ρ_{met} are source term $(1/s)$, vapor density (kg/m^3) and metal density (kg/m^3) respectively.

The phase field physics is described using the Cahn–Hillard equation as follows,

$$\frac{\partial \emptyset}{\partial t}+u\nabla\emptyset=\nabla\frac{\gamma\lambda}{\varepsilon^2}\psi+Q_s' \quad (17)$$

$$\psi=-\nabla\varepsilon^2\nabla\emptyset+(\emptyset^2-1)\emptyset \quad (18)$$

$$Q_s'=m^{\bullet}\Pi(\frac{1-\emptyset}{\rho_{vap}}+\frac{\emptyset}{\rho_{melt}}) \quad (19)$$

where $\emptyset$, γ, λ, ε, ψ and Q_s' are phase-field variable (-), mobility $(m.s/kg)$, mixing energy density (N), interface thickness parameter (m), phase-field help variable and source term for evaporation $(1/s)$, respectively.

5.2. Results

The improved model simulates the interaction between laser beam and multi-layer metal powder. Simulations were performed using Ti6Al4V and AlSi10Mg alloys as a medium powder to study the effect of the process parameters on the melt pool width and melt pool life time. The effect of the laser power and scanning velocity on the formed melt pool width and formed melt pool life time was studied. Also, mathematical relationships between process parameters, and melt pool width and melt poo life time were developed.

5.2.1. Ti6Al4V

The model simulates the SLM process by coupling three physics. At a constant laser spot diameter, the effect of the changing laser powers and scanning velocities were studied and mathematical relationships were developed. Figure 5.2 illustrates the process in detail. Figure 5.2a shows an angular view of the scanned powders in which the molten track and melt pool are clearly obvious. Figure 5.2b shows the top view of the scanned powders. Also, Figure 5.2c shows the symmetric view in which the complete melt of the powder layers is understandable.

Effect of Laser Power

Effect of the process parameters on the melt pool width would be described using Rosenthal's equation [64] as following,

$$w = \sqrt{\frac{8}{\pi e} . \frac{PA}{\rho C_p^* V (T_m - T_p)}} \tag{20}$$

where w and T_p are melt pool width (m) and preheat temperature (K) respectively.

The relationship between laser power and melt pool width is a direct quadratic relationship according to the above equation. Any increase in laser power will cause a quadratic increase in melt pool width. Performed simulations also obey this behavior in the normal regime, but the simulations do not obey the Rosenthal equation when the parameters enter the evaporation chaos regions. For this, simulation results were tried to fit on a third-degree

curve to cover the chaotic regions as well. Figure 5.3 shows the fitted curves on the simulation results. It shows melt pool width for different laser powers at various scanning velocities. Also, Table 5.1 shows the material properties for Ti6Al4V that were used in the simulations.

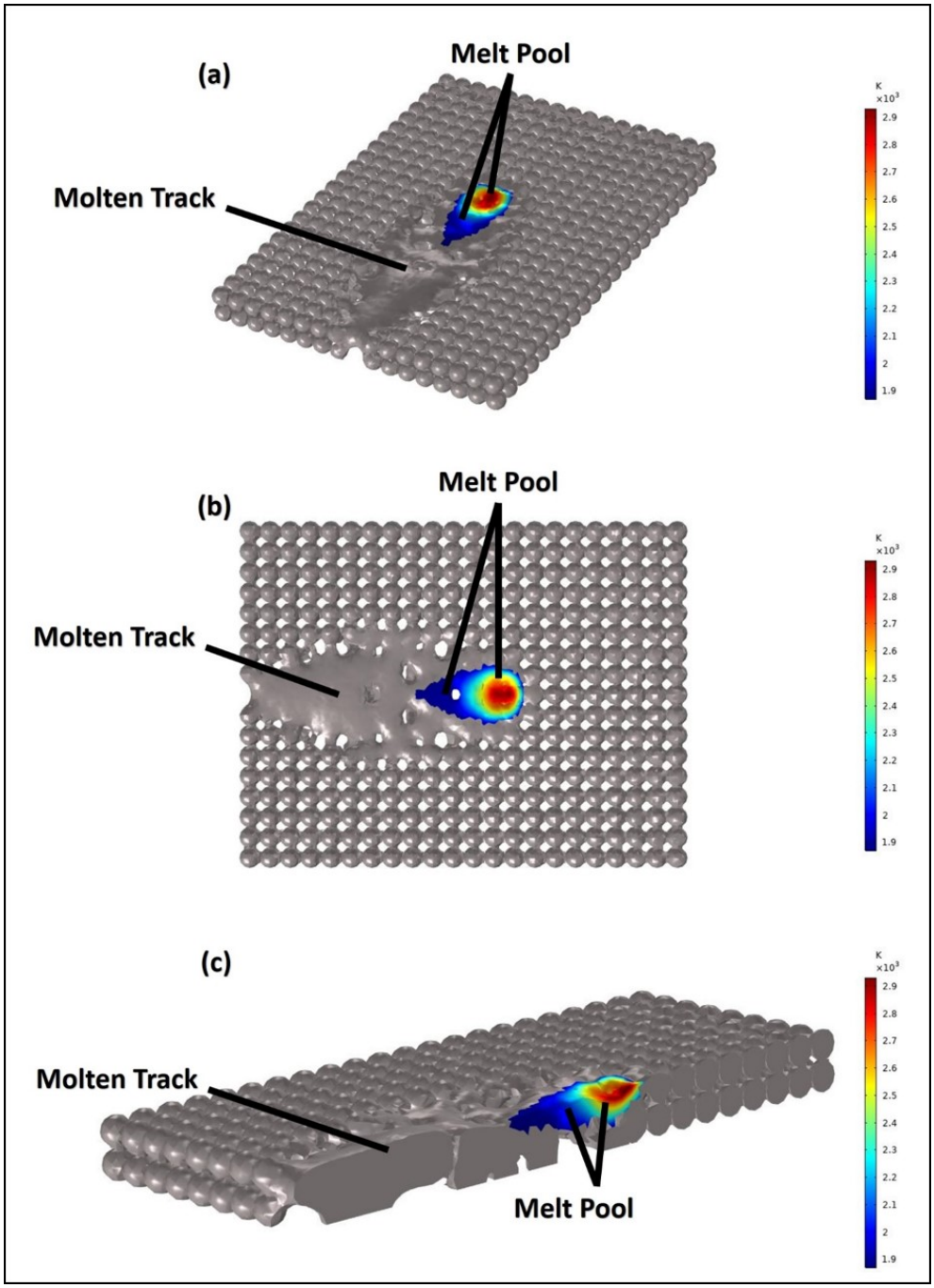


Figure 5.2. 3-D molten track and melt pool temperature distributions of Ti6Al4V using 500 mm/s scanning velocity, 110 W laser power, and 85 μm laser spot diameter: (a) angular complete view, (b) top complete view, (c) symmetry view.

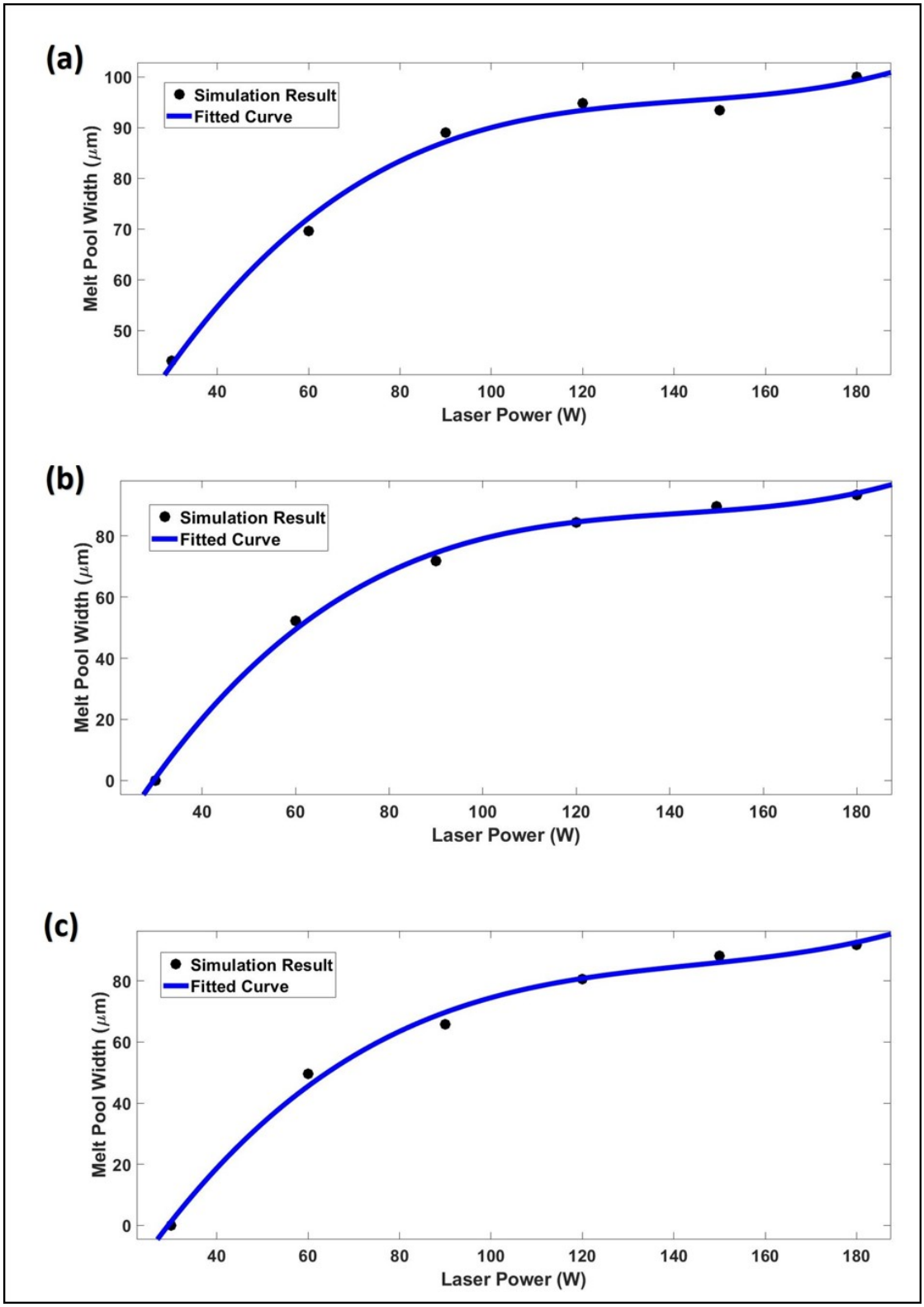


Figure 5.3. Simulation results and fitted curves of melt pool width for Ti6Al4V at different laser powers and a laser spot diameter of 85 μm; scanning velocity of a) 800 mm/s, b) 1100 mm/s, and c) 1400 mm/s.

Table 5.1. Material Properties of Ti6Al4V [24].

Material property	Symbol	Value	Unit
Melting Temperature	T_m	1878	K
Melting Interval	δT	± 10	K
Evaporation Temperature	T_{ev}	3560	K
Latent Heat of Melting	H_m	2.84×10^5	J/kg
Latent Heat of Evaporation	H_{ev}	9.092×10^6	J/kg
Density	ρ	4000	kg/m^3
Thermal Conductivity	k	$1.57 + 1.6 \times 10^{-2}T - 1 \times 10^{-6}T^2$	$W/m.K$
Specific Heat Capacity	C_p	$492.4 + 0.025T - 4.18 \times 10^{-6}T^2$	$J\ /\ kg.K$
Marangoni Coefficient	$d\gamma/dT$	-0.26×10^{-3}	$N\ /\ m.K$
Absorption Coefficient	A	$0.6\ (solid) - 0.3(liquid)$	$-$

Also, Figure 5.4 shows the simulation results for the effect of laser power on melt pool life. The lifetime is related to the amount of input energy in a given metal material. The increased laser power, hence the increased input energy, is expected to extend the melt pool life. Simulation results obey this illustration as shown in Figure 5.4.

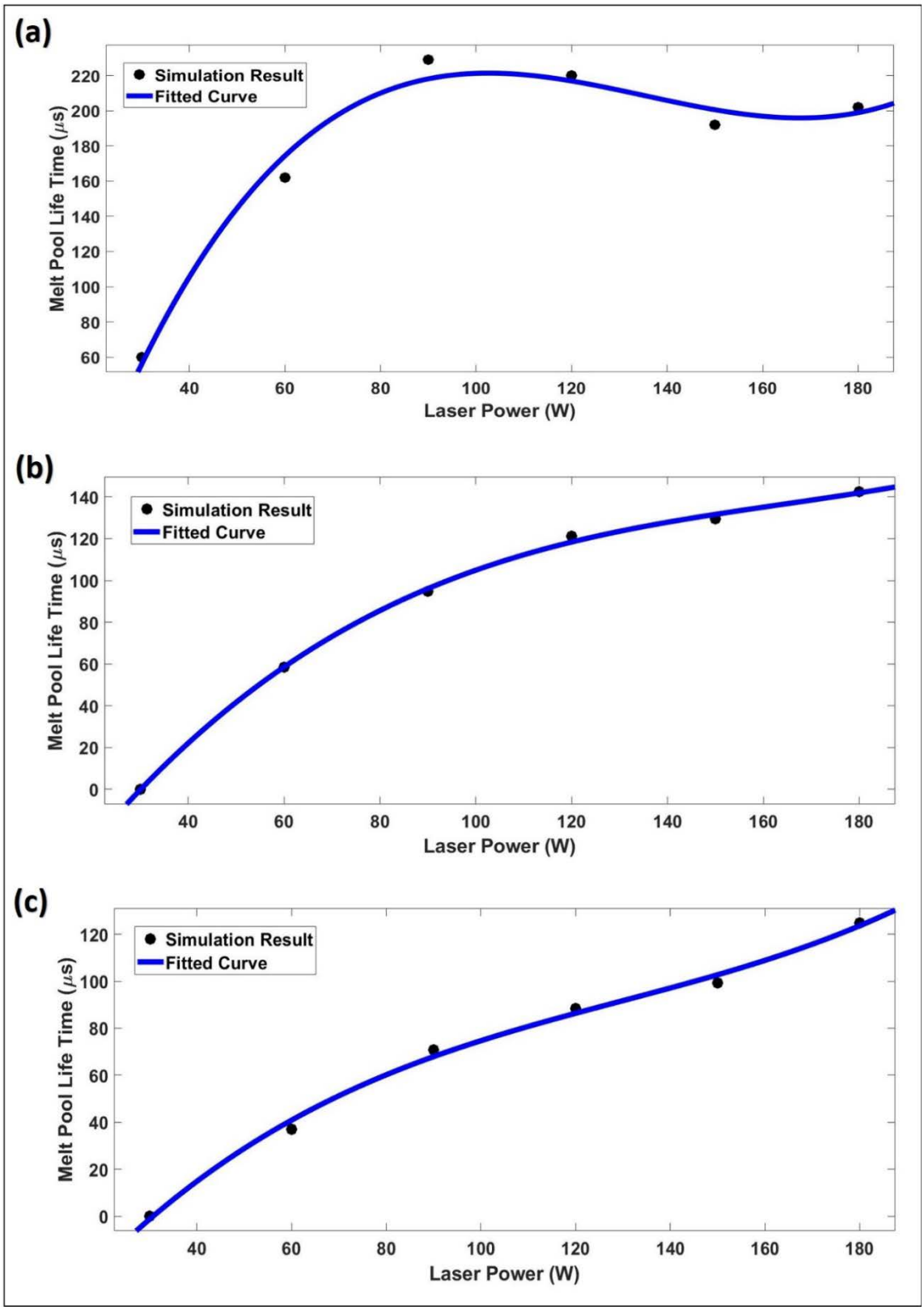


Figure 5.4. Simulation results and fitted curves of melt pool life time for Ti6Al4V at different laser powers and a laser spot diameter of 85 (μm); scanning velocity of a) 800 mm/s, b) 1100 mm/s, and c) 1400 mm/s.

Fitted curves and their mathematical relationships are the base materials of the controller design to contrl the 3-D printing machine. Using mathematical relationships, via a feedback system, the machine will be able to instantly intervene in the melt pool width and life according to the fabrication requirement. The mathematical relationships (fitted curves equations) are listed in Table 5.2 for melt pool width and melt pool life time respectively.

Table 5.2. Equations of the fitted curves for simulation results of the laser power- melt pool width and laser power- melt pool life time for Ti6Al4V at different scanning velocities. (P = Laser Power (W)- w: Melt Pool Width (μm)- t: Melt Pool Life Time (μs)- Laser Spot Diameter = 85 μm).

Velocity (mm/s)	Fitted Curve Equation	Domain	Range
800	$w = (3.09e-5)P^3 - 0.01327P^2 + 1.964P - 4.613$	$30 \le P \le 180$	$43.19 \le w \le 99.16$
	$t = (18.38e-5)P^3 - 0.07457P^2 + 9.498P - 166.7$	$30 \le P \le 180$	$56.08 \le t \le 198.79$
1100	$w = (5.309e-5)P^3 - 0.02267P^2 + 3.327P - 80$	$30 \le P \le 180$	$0.84 \le w \le 93.97$
	$t = (3.769e-5)P^3 - 0.01861P^2 + 3.369P - 86.33$	$30.1 \le P \le 180$	$30.1 \le P \le 180$
1400	$w = (4.444e-5)P^3 - 0.01925P^2 + 2.931P - 70.6$	$30 \le P \le 180$	$1.2 \le w \le 92.45$
	$t = (4.029e-5)P^3 - 0.01565P^2 + 2.56P - 65.07$	$30.8 \le P \le 180$	$30.8 \le P \le 180$

Effect of Scanning Velocity

The effect of the scanning velocity can be explained by referring to Equation 20 as well. Respecting Equation 20 the relationship between scanning velocity and melt pool width, when other parameters are constant, is a quadratic inverse relationship. In other words, an increase in scanning velocity results in a decrease in melt pool width due to the reduction of the interaction time of the metal powder with the laser beam. Figure 5.5 shows the simulation results and fitted curves of the melt pool width during the changing velocities in various laser powers. For the reasons discussed above, it was preferred to fit the simulation results on a third-order equation here as well.

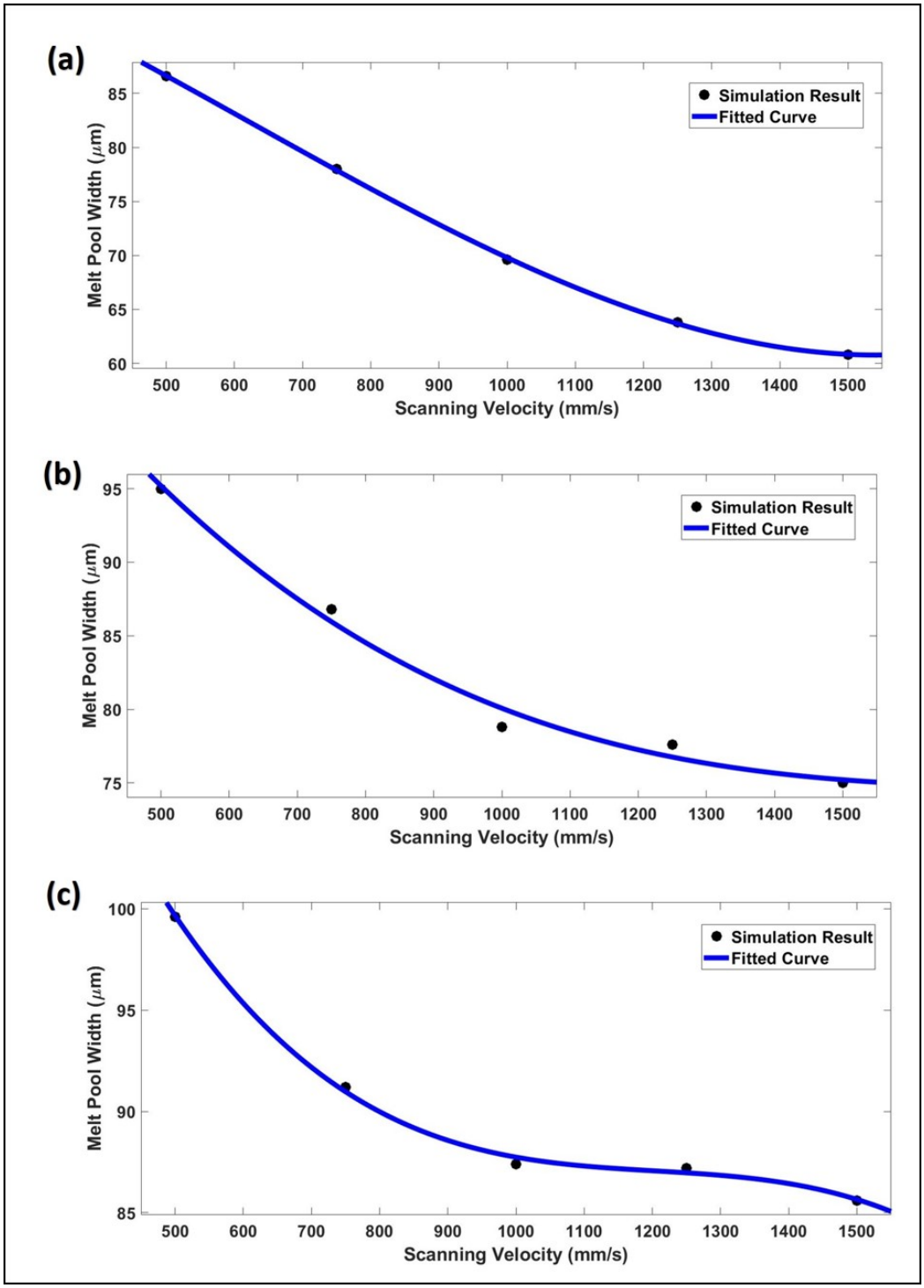


Figure 5.5. Simulation results and fitted curves of melt pool width for Ti6Al4V at different scanning velocities and a laser spot diameter of 85 μm; laser power of a) 80 W, b) 110 W, and c) 140 W.

On the life time of the melt pool during changing velocities in various laser powers, Figure 5.6 shows the simulation results and fitted curve.

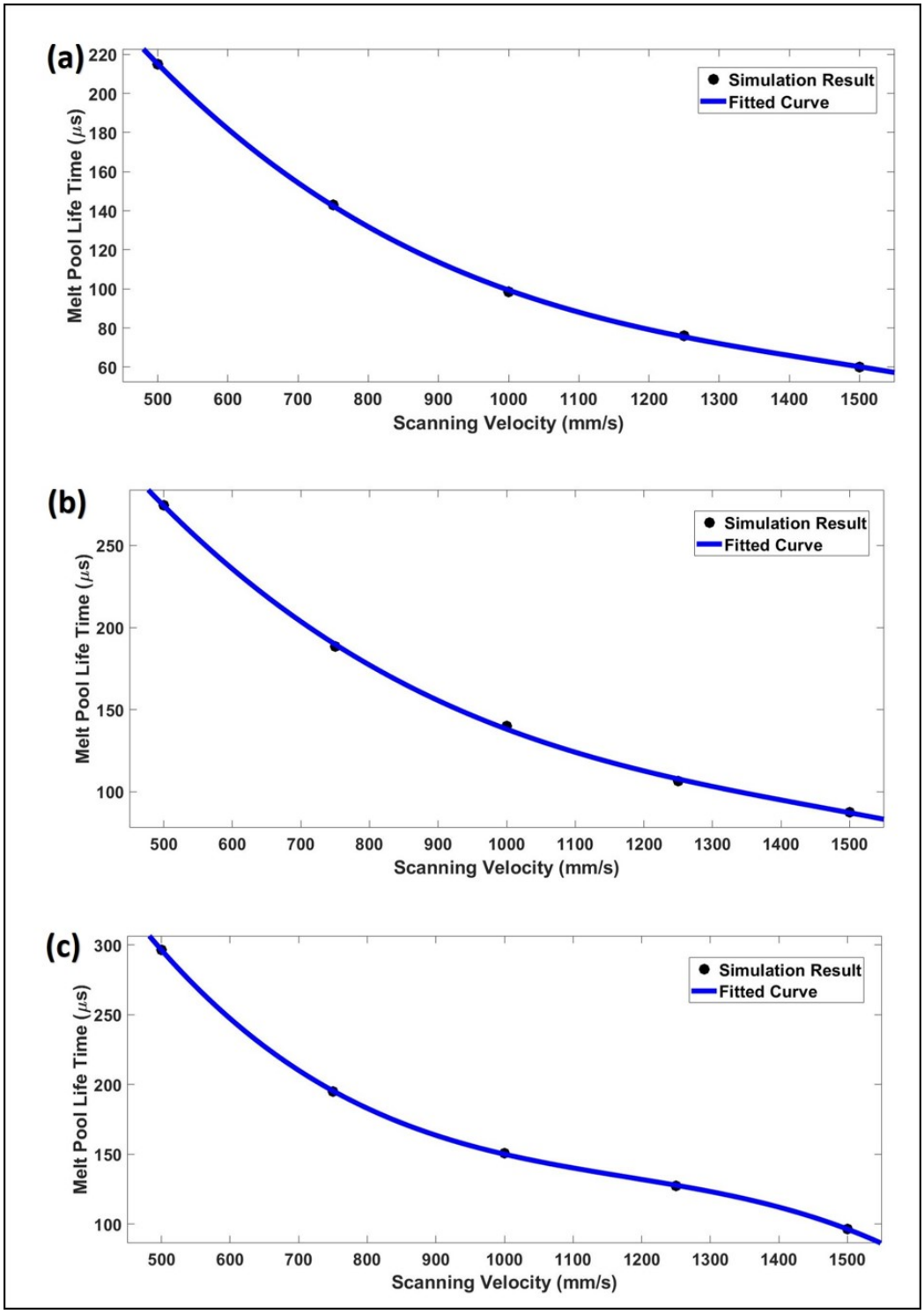


Figure 5.6. Simulation results and fitted curves of melt pool life time for Ti6Al4V at different scanning velocities and a laser spot diameter of 85 μm; laser power of a) 80 W, b) 110 W, and c) 140 W.

Mathematical relationships which relate the scanning velocity to the melt pool width and melt pool life time in constant laser powers are tabulated in Table 5.3 respectively.

Table 5.3. Equations of the fitted curves for simulation results of the scanning velocity- melt pool width and scanning velocity- melt pool life time for Ti6Al4V at different laser powers. (V = Scanning Velocity (mm/s)- w: Melt Pool Width (μm)- t: Melt Pool Life Time (μs)- Laser Spot Diameter = 85 μm).

Laser Power (W)	Fitted Curve Equation	Domain	Range
80	$w = (1.387e-8)V^3 - (2.583e-5)V^2 - 0.01921V + 101$	$500 \leq V \leq 1500$	$60.87 \leq w \leq 86.67$
	$t = -(1.12e-7)V^3 + (48.9e-5)V^2 - 0.7693V + 491.5$	$500 \leq V \leq 1500$	$59.8 \leq t \leq 215.1$
110	$w = -(8.427e-9)V^3 + (4.581e-5)V^2 - 0.0842V + 126.9$	$500 \leq V \leq 1500$	$75.23 \leq w \leq 95.19$
	$t = -(1.227e-7)V^3 + (53.83e-5)V^2 - 0.8649V + 587.4$	$500 \leq V \leq 1500$	$87.11 \leq t \leq 274.18$
140	$w = -(3.2e-8)V^3 + (11.57e-5)V^2 - 0.1413V + 145.4$	$500 \leq V \leq 1500$	$85.77 \leq w \leq 99.67$
	$t = -(3.456e-7)V^3 + (122.2e-5)V^2 - 1.521V + 794.4$	$500 \leq V \leq 1500$	$96 \leq t \leq 296.2$

5.2.2. AlSi10Mg

Similar to the Ti6Al4V, simulations were done for AlSi10Mg alloy as well. Effect of the laser power and scanning velocity on the melt pool width and melt pool life time was developed for AlSi10Mg. The relationships between process parameters and melt pool width and melt pool life time were achieved and graphs were drawn. Figure 5.7 shows the AlSi10Mg powder and laser beam interaction. Figure 5.7a shows the angular view of the temperature distributions, melt pool, and molten track. Figure 5.7b shows the top view of the process and Figure 5.7c shows the symmetry view of the melting and solidification.

Effect of Laser Power

The same behavior of Ti6Al4V discussed earlier was also observed for AlSi10Mg. The effect of laser power on the melt pool width follows Equation 20 in the normal regime. However, the manner of the melt pool width does not follow Equation 20 [64] in the evaporative chaos regime. For this reason, the simulation results are also fitted on a third-degree equation here. Figure 5.8 shows the curves fitted on the simulation results. The width of the melt pool is presented at different scanning speeds according to the changes in laser power.

Figure 5.9 shows the curves that were fitted on the simulation results of the life time. The figure presents the effect of the laser power on the melt pool life time. As discussed earlier the life time of the melt pool is related to the input of the energy amount. Any increase of the laser power and respectively energy resulted in life time increase.

Mathematical relationships of the fitted curves that will be used during the controller design for the 3D-printing machine are presented in Table 5.4. Table 5.4 presents equations that relate the laser power to the melt pool width. Also, the table includes relationships that relate the laser power to the melt pool life time.

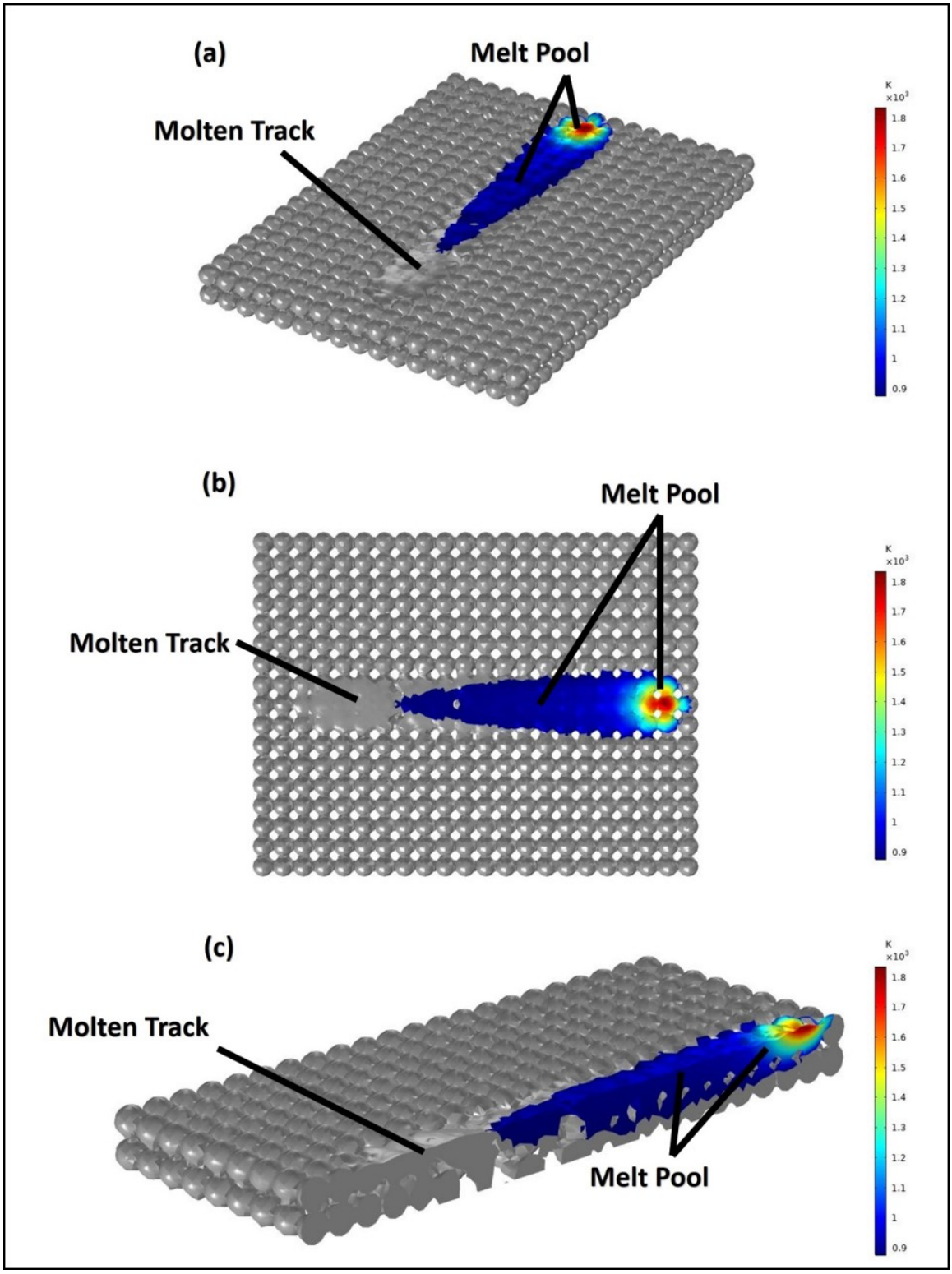


Figure 5.7. 3-D molten track and melt pool temperature distributions of AlSi10Mg using 1100 mm/s scanning velocity, 180 W laser power, and 85 μm laser spot diameter: (a) angular complete view, (b) top complete view, (c) symmetry view.

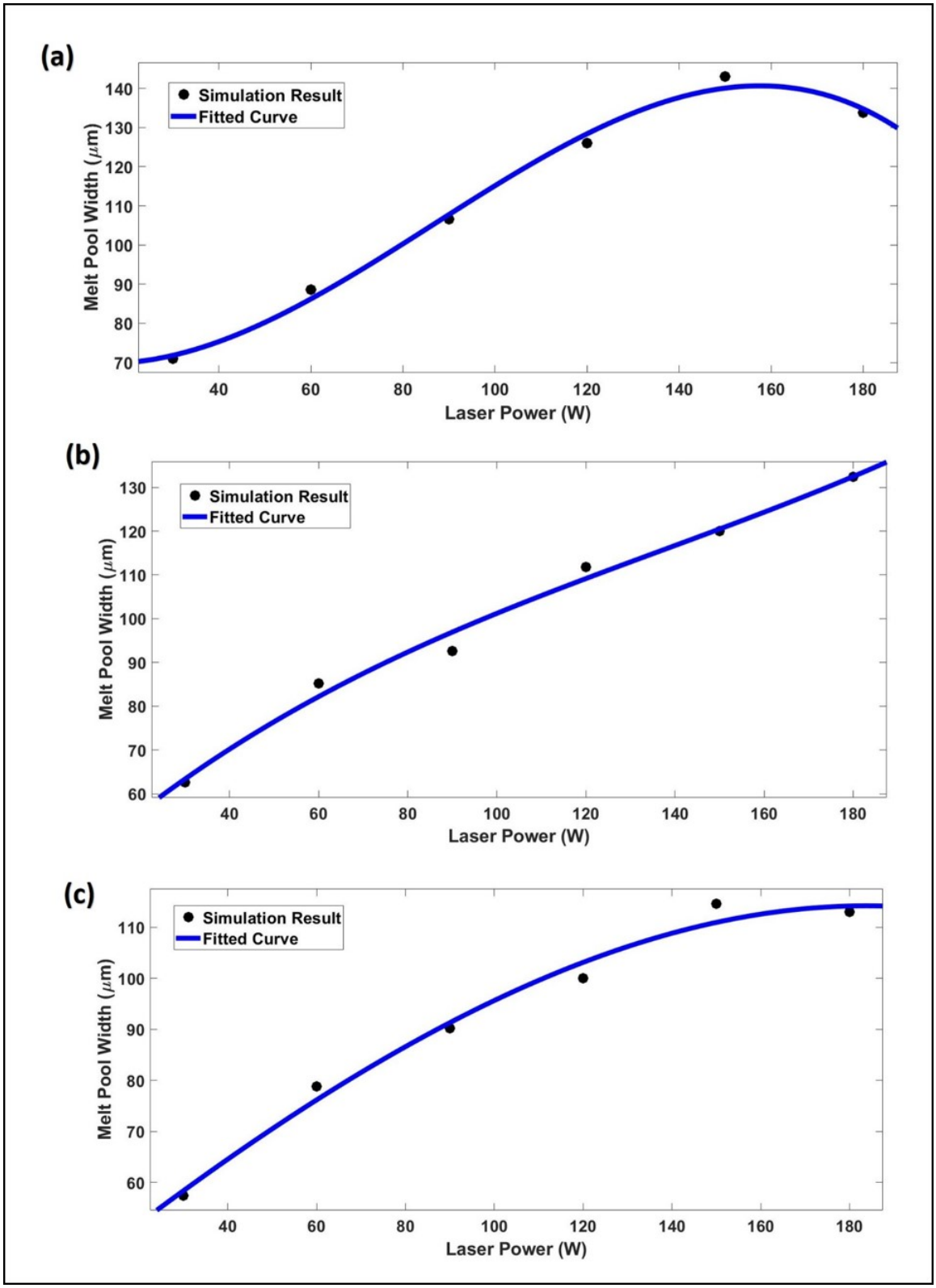


Figure 5.8. Simulation results and fitted curves of melt pool width for AlSi10Mg at different laser powers and a laser spot diameter of 85 μm; scanning velocity of a) 800 mm/s, b) 1100 mm/s, and c) 1400 mm/s.

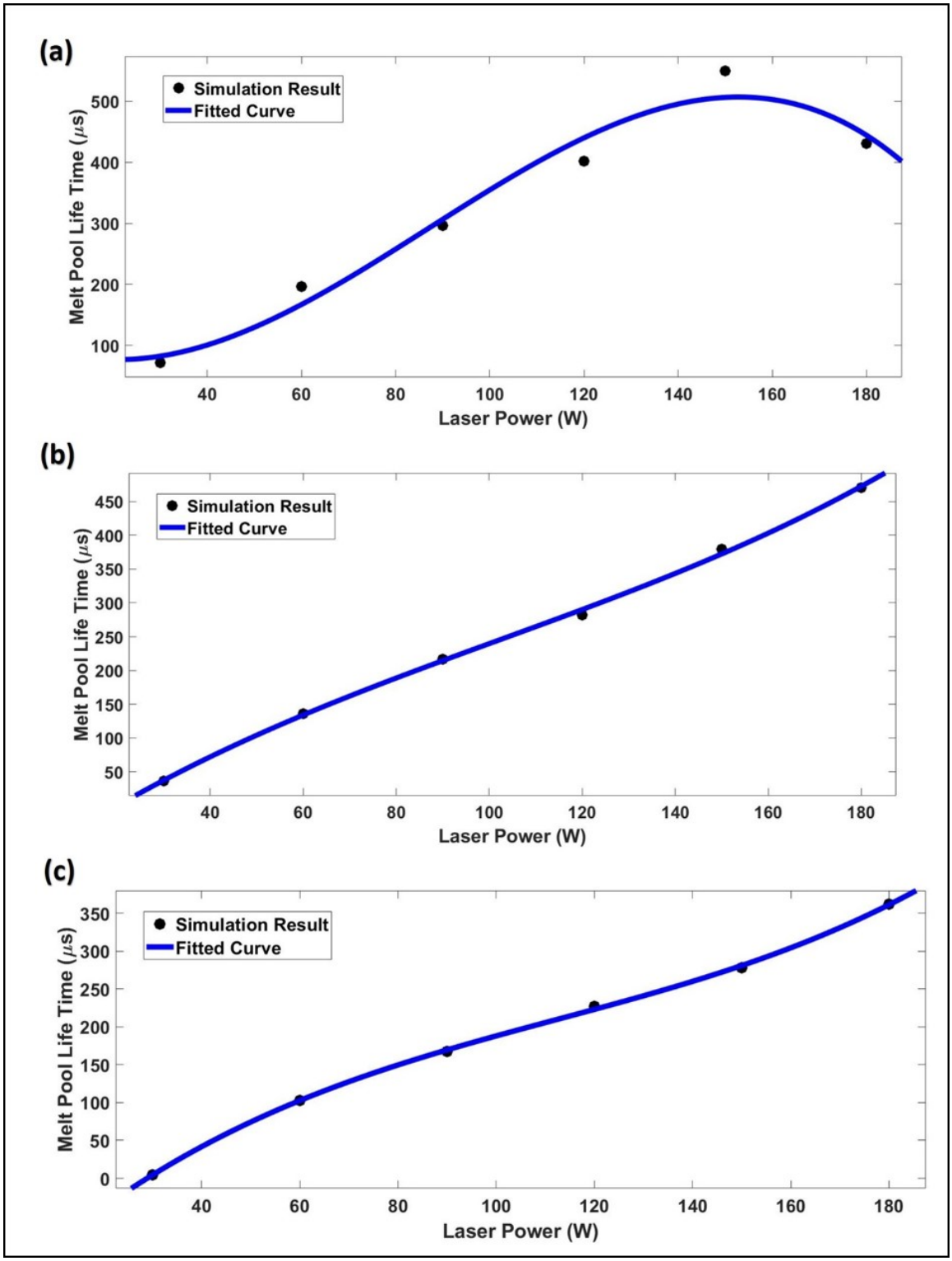


Figure 5.9. Simulation results and fitted curves of melt pool life time for AlSi10Mg at different laser powers and a laser spot diameter of 85 μm; scanning velocity of a) 800 mm/s, b) 1100 mm/s, and c) 1400 mm/s.

Table 5.4. Equations of the fitted curves for simulation results of the laser power- melt pool width and laser power-melt pool life time for AlSi10Mg at different scanning velocities. (P = Laser Power (W)- w: Melt Pool Width (µm)- t: Melt Pool Life Time (µs)- Laser Spot Diameter = 85 µm).

Velocity (mm/s)	Fitted Curve Equation	Domain	Range
800	$w = -(4.952e-5)P^3 + 0.01286P^2 - 0.3649P + 72.53$	$30 \leq P \leq 180$	$71.82 \leq w \leq 134.71$
	$t = -(37.72e-5)P^3 + 0.09844P^2 - 3.66P + 113.7$	$30 \leq P \leq 180$	$82.31 \leq t \leq 444.52$
1100	$w = (9.808e-6)P^3 - (40.98e-4)P^2 + 0.9291P + 38.87$	$30 \leq P \leq 180$	$63.31 \leq w \leq 130.53$
	$t = (7.01e-5)P^3 - 0.02159P^2 + 4.722P - 86.73$	$30 \leq P \leq 180$	$37.39 \leq t \leq 472.53$
1400	$w = -(4.047e-6)P^3 - (75.31e-5)P^2 + 0.6868P + 38.53$	$30 \leq P \leq 180$	$58.34 \leq w \leq 114.15$
	$t = (11.06e-5)P^3 - 0.03734P^2 + 5.941P - 143.1$	$30 \leq P \leq 180$	$4.51 \leq t \leq 361.48$

Effect of Scanning Velocity

For the effect of scanning velocity on the melt pool width, the reference equation for the normal regime is still Equation 20. However, according to the explanation given earlier, the simulation results were fitted on third-order equations. Simulation results and fitted curves are shown in Figure 5.10.

Simulation results for the effect of the melt pool life time during the changing velocities at the different laser powers were fitted on the curves that are shown in Figure 5.11.

Also, Table 5.5 tabulates the mathematical relationships representing the relations relating scanning velocity to the melt pool width and scanning velocity to the life time at the various laser powers.

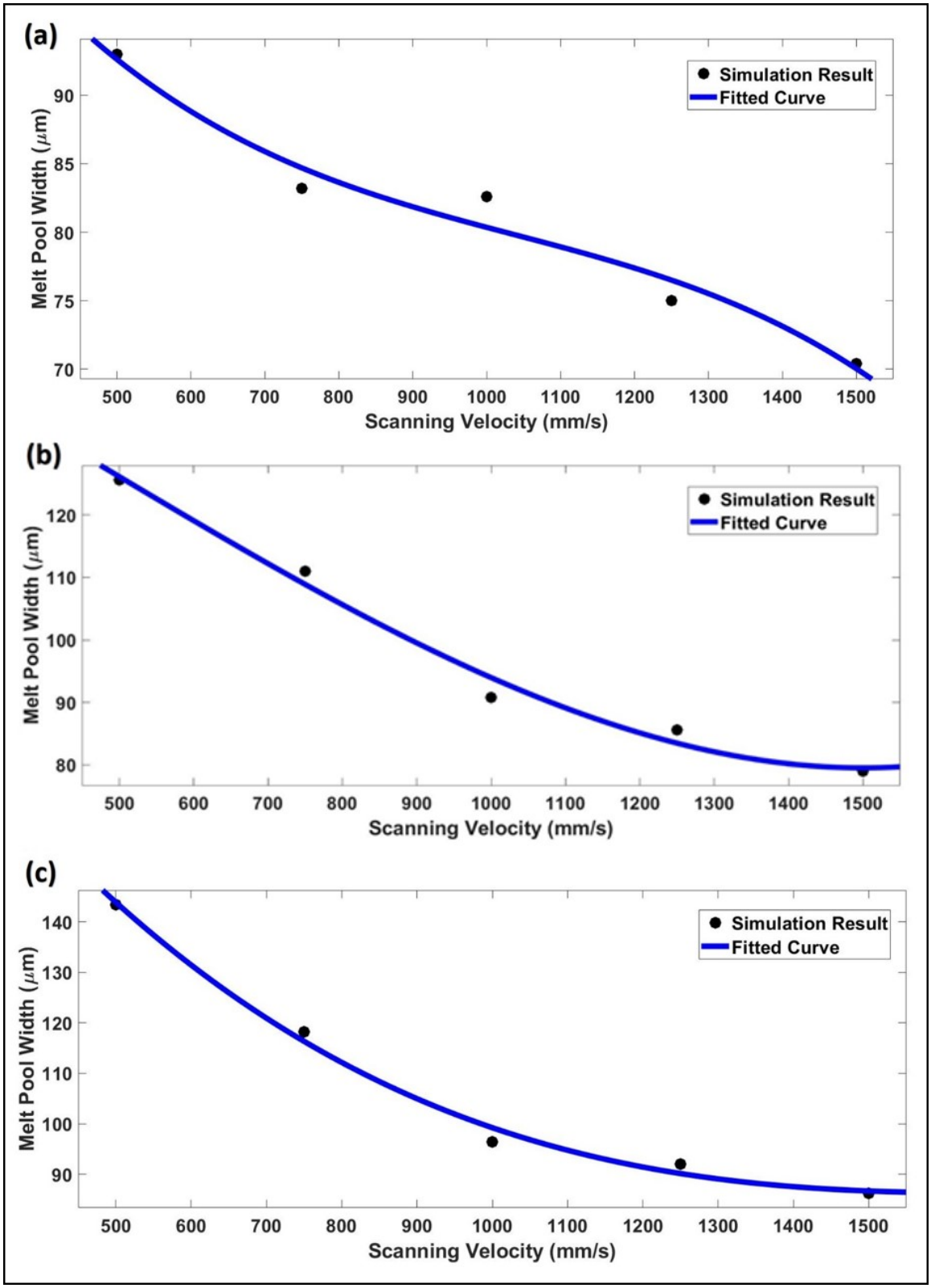


Figure 5.10. Simulation results and fitted curves of melt pool width for AlSi10Mg at different scanning velocities and a laser spot diameter of 85 μm; laser power of a) 80 W, b) 110 W, and c) 140 W.

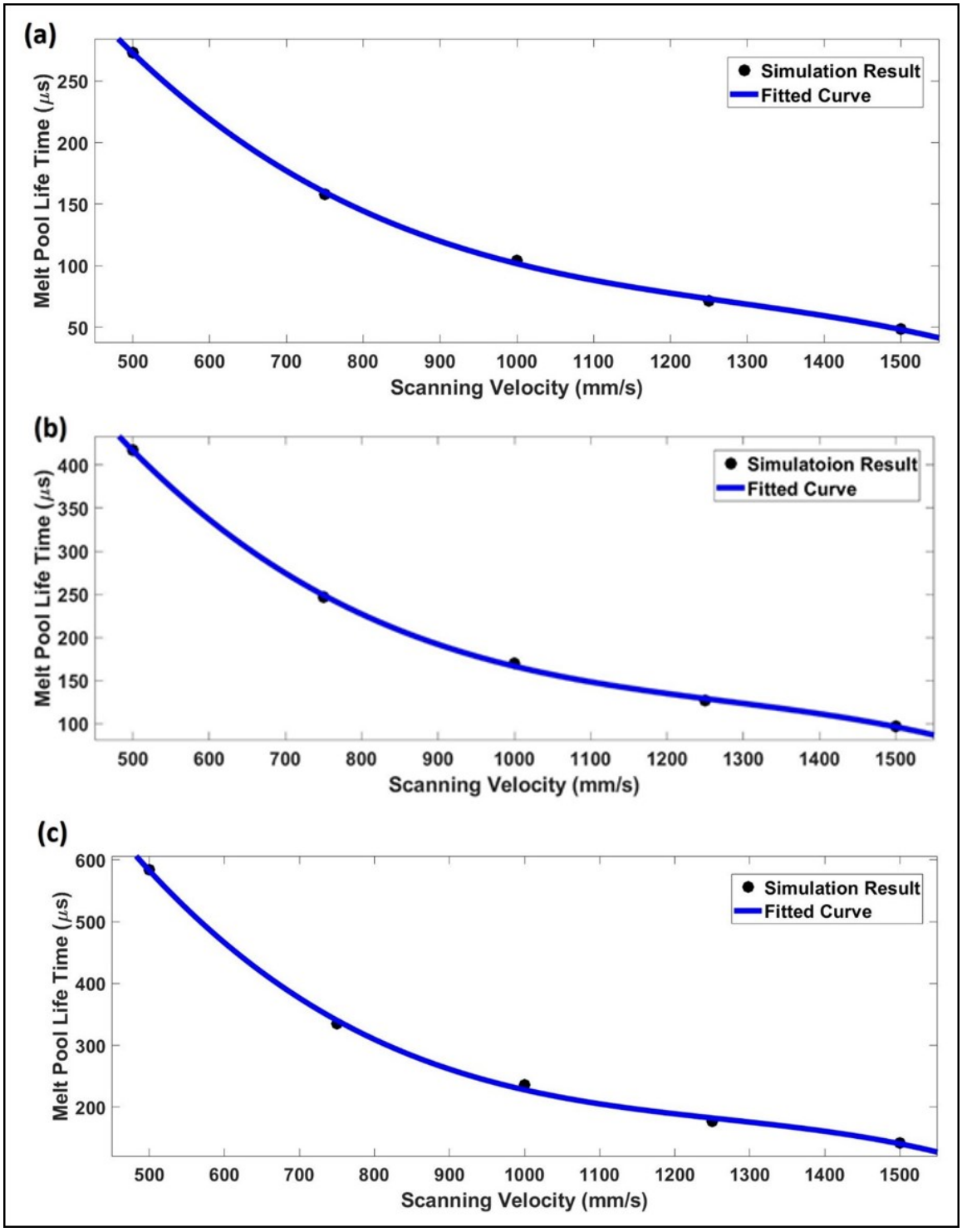


Figure 5.11. Simulation results and fitted curves of melt pool life time for AlSi10Mg at different scanning velocities and a laser spot diameter of 85 μm; laser power of a) 80 W, b) 110 W, and c) 140 W.

Table 5.5. Equations of the fitted curves for simulation results of the scanning velocity- melt pool width and scanning velocity- melt pool life time for AlSi10Mg at different laser powers. (V = Scanning Velocity (mm/s)- w: Melt Pool Width (µm)- t: Melt Pool Life Time (µs)- Laser Spot Diameter = 85 µm).

Laser Power (W)	Fitted Curve Equation	Domain	Range
80	$w = -(3.307e-8)V^3 + (10.31e-5)V^2 - 0.1213V + 131.6$	$500 \leq V \leq 1500$	$92.59 \leq w \leq 70.01$
	$t = -(2.741e-7)V^3 + (105.7e-5)V^2 - 1.448V + 766.4$	$500 \leq V \leq 1500$	$47.56 \leq t \leq 272.38$
110	$w = (2.24e-8)V^3 - (3.177e-5)V^2 - 0.05586V + 159.2$	$500 \leq V \leq 1500$	$126.12 \leq w \leq 79.52$
	$t = -(4.288e-7)V^3 + (16.46e-4)V^2 - 2.218V + 1168$	$500 \leq V \leq 1500$	$97.3 \leq t \leq 416.9$
140	$w = -(2.56e-8)V^3 + (14.1e-5)V^2 - 0.2561V + 239.8$	$500 \leq V \leq 1500$	$143.8 \leq w \leq 86.5$
	$t = -(6.72e-7)V^3 + (255.1e-5)V^2 - 3.36V + 1709$	$500 \leq V \leq 1500$	$140.75 \leq t \leq 582.75$

6. CONCLUSIONS

The thesis studies the SLM modeling, SLM simulation, developing process parameters for SLM, developing mathematical relationships between process parameters and temperature, melt pool width, and melt pool life time, and experimental confirmation of them by microstructure and mechanical marathon for Stainless Steel 316L, AlSi10Mg and Ti6Al4V. The thesis studies the modeling and simulation of the SLM process coupling different physics for Stainless Steel 316L, AlSi10Mg, and Ti6Al4V metal powders. Outcomes are as:

- For the Stainless Steel 316L alloy, using the developed model and simulating the SLM process in COMSOL software, mathematical relationships between laser power, laser spot diameter, and temperature were extracted. These are powerful tools to calculate melt-pool temperature and to predict its manner. The model can predict process parameters by simulating the formed temperature during the process. Mathematical expressions could also be used to control melt-pool temperature. Mathematical relationships between parameters are used to give an overview of the laser-powder interaction, which reduces the need to simulate for each set of parameters. These equations could also be potentially used to overcome the challenge of experimental testing for each set of parameters to obtain the appropriate sets of parameters for production.

  For Stainless Steel 316L powder, temperatures at 40 μm depth of the layer were obtained for various laser powers, scanning velocities, and laser spot diameters. The simulation results were fitted on the curves, and the equations (mathematical relationships between process parameters) of the fitted curves were obtained. One of the most important pieces of data in laser power–temperature equations is the slope of the equations. The slopes could be considered as transfer functions in a control system. Therefore, a controller design could be performed, and the process may be controlled with a temperature or any other available process parameter feedback(s). The feedback system can feed the control system using real-time temperatures measured by a thermal camera.

- In case of AlSi10Mg alloy, employing the developed model, process parameters at different scanning velocities, including laser powers and laser spot diameters, have been developed. The results of the simulations were fitted on the curves and the equations of

the fitted curves- which are the mathematical relationships between laser power, laser spot diameter and melt pool temperature were obtained. Here, as in Stainless Steel 316L alloy, mathematical relationships are basic materials for designing a controller to instantly control the melt pool temperature from deviations with a temperature feedback system. The slope of the equations in the laser power-temperature mathematical relationships can be used as the Transfer Function in designing the control system.

Insufficient and excessive process parameters adversely affect the microstructure and mechanical properties. They cause various microstructure defects in the final product. As a result of defects, mechanical properties weaken and UTS, YS and Elongation values decrease.

- A comprehensive experimental study was done to confirm the validity of the developed model. Using developed process parameters, samples were fabricated in the 3-D printer for both Stainless Steel 316L and AlSi10Mg alloys. A microstructure study was done on the Stainless Steel 316L alloy and the simulation results were confirmed. For the case of AlSi10Mg alloy, besides the samples for microstructure study, samples for the mechanical properties study were fabricated as well. Both microstructure study and mechanical properties study confirm the validity of the simulation results.

- The existing model was improved to be able to present the topology of the melt pool. It was done by adding a new physics, Phase Field physics. Simulations coupling three physics were done for the Ti6Al4V and AlSi10Mg as medium material.

  Phase field physic able us to present the fluid flow, melt pool geometry and etc. The model was more completed by adding this physic, on the other hand, the convergence became more difficult during the simulation.

  Simulation results were presented as the effect of the lase power and scanning velocity on the melt pool width and melt pool life time for both Ti6Al4V and AlSi10Mg alloys. Mathematical relationships that relate the laser power to the melt pool width and melt pool life time at various scanning velocities and also relating scanning velocity to the melt pool width and melt pool life time at different laser powers was developed for both Ti6Al4V and AlSi10Mg alloys.

REFERENCES

1. Jacobs, P. F. (2001). A brief history of rapid prototyping and manufacturing: The growth years. *P/M Science & Technology Briefs*, 3(5), 13-16.

2. The third industrial revolution. (2012). *The Economist Newspaper Limited*,40

3. Olakanmi, E. O., Cochrane, R. F., and Dalgarno, K. W. (2015). A review on selective laser sintering/melting (SLS/SLM) of aluminium alloy powders: Processing, microstructure, and properties. *Progress in Materials Science*, 74, 401-477.

4. Gourd, L. M. (1995). *Fundamentals of Welding-Principles of Welding Technology*. Paris: Arnold, 52.

5. Ahmadi, A., Shayesteh Moghaddam, N., Elahinia, M., Karaca, H. E., and Mirzaeifar, R. (2016, June). *Finite element modeling of selective laser melting 316l stainless steel parts for evaluating the mechanical properties.* In International Manufacturing Science and Engineering Conference (Vol. 49903, p. V002T01A003). American Society of Mechanical Engineers.

6. Totten, G. E. (2006), *Steel Heat Treatment Handbook-2*, (2nd ed.) Florida: CRC Press, 365.

7. Ishimoto, T., Wu, S., Ito, Y., Sun, S. H., Amano, H., and Nakano, T. (2020). Crystallographic orientation control of 316L austenitic stainless steel via selective laser melting. *ISIJ International*, 60(8), 1758-1764.

8. Tsutsumi, Y., Ishimoto, T., Oishi, T., Manaka, T., Chen, P., Ashida, M., ... and Nakano, T. (2021). Crystallographic texture-and grain boundary density-independent improvement of corrosion resistance in austenitic 316L stainless steel fabricated via laser powder bed fusion. *Additive Manufacturing*, 45, 102066.

9. Zhang, K., Liu, T., Liao, W., Zhang, C., Zheng, Y., and Shao, H. (2018). S*imulation of the thermal behavior and analysis of solidification process during selective laser melting of alumina.* International Solid Freeform Fabrication Symposium. University of Texas at Austin, 149

10. Bruna-Rosso, C., Demir, A. G., and Previtali, B. (2018). Selective laser melting finite element modeling: Validation with high-speed imaging and lack of fusion defects prediction. *Materials & Design*, 156, 143-153.

11. Foteinopoulos, P., Papacharalampopoulos, A., and Stavropoulos, P. (2018). On thermal modeling of Additive Manufacturing processes. *CIRP Journal of Manufacturing Science and Technology*, 20, 66-83.

12. Leitz, K. H., Singer, P., Plankensteiner, A., Tabernig, B., Kestler, H., and Sigl, L. S. (2016). *Thermo-Fluiddynamical Modelling of Laser Beam-Matter Interaction in Selective Laser Melting.* In Excerpt from the Proceedings of the 2016 COMSOL Conference in Munich.

13 Artinov, A., Bachmann, M., and Rethmeier, M. (2018). Equivalent heat source approach in a 3D transient heat transfer simulation of full-penetration high power laser beam welding of thick metal plates. *International Journal of Heat and Mass Transfer*, 122, 1003-1013.

14. Bayat, M., Thanki, A., Mohanty, S., Witvrouw, A., Yang, S., Thorborg, J., ... and Hattel, J. H. (2019). Keyhole-induced porosities in Laser-based Powder Bed Fusion (L-PBF) of Ti6Al4V: High-fidelity modelling and experimental validation. *Additive Manufacturing*, 30, 100835.

15. Courtois, M., Carin, M., Le Masson, P., Gaied, S., and Balabane, M. (2013). A new approach to compute multi-reflections of laser beam in a keyhole for heat transfer and fluid flow modelling in laser welding. *Journal of Physics D: Applied Physics*, 46(50), 505305.

16. Mukherjee, T., Wei, H. L., De, A., and DebRoy, T. (2018). Heat and fluid flow in additive manufacturing—Part I: Modeling of powder bed fusion. *Computational Materials Science*, 150, 304-313.

17. Shi, X., Ma, S., Liu, C., and Wu, Q. (2017). Parameter optimization for Ti-47Al-2Cr-2Nb in selective laser melting based on geometric characteristics of single scan tracks. *Optics & Laser Technology*, 90, 71-79.

18. Liu, S., Zhu, H., Peng, G., Yin, J., and Zeng, X. (2018). Microstructure prediction of selective laser melting AlSi10Mg using finite element analysis. *Materials & Design*, 142, 319-328.

19. Liu, B., Li, B. Q., Li, Z., Bai, P., Wang, Y., and Kuai, Z. (2019). Numerical investigation on heat transfer of multi-laser processing during selective laser melting of AlSi10Mg. *Results in Physics*, 12, 454-459.

20. Han, Q., Setchi, R., Lacan, F., Gu, D., and Evans, S. L. (2017). Selective laser melting of advanced Al-Al2O3 nanocomposites: simulation, microstructure and mechanical properties. *Materials Science and Engineering: A*, 698, 162-173.

21. Liu, S., Zhu, J., Zhu, H., Yin, J., Chen, C., and Zeng, X. (2020). Effect of the track length and track number on the evolution of the molten pool characteristics of SLMed Al alloy: Numerical and experimental study. O*ptics & Laser Technology*, 123, 105924.

22. Li, Y., and Gu, D. (2014). Parametric analysis of thermal behavior during selective laser melting additive manufacturing of aluminum alloy powder. *Materials & design*, 63, 856-867.

23. Du, Y., You, X., Qiao, F., Guo, L., and Liu, Z. (2019). A model for predicting the temperature field during selective laser melting. *Results in Physics*, 12, 52-60.

24. Mukherjee, T., Wei, H. L., De, A., and DebRoy, T. (2018). Heat and fluid flow in additive manufacturing–Part II: Powder bed fusion of stainless steel, and titanium, nickel and aluminum base alloys. *Computational Materials Science*, 150, 369-380.

25. Pei, W., Zhengying, W., Zhen, C., Junfeng, L., Shuzhe, Z., and Jun, D. (2017). Numerical simulation and parametric analysis of selective laser melting process of AlSi10Mg powder. *Applied Physics A*, 123(8), 1-15.

26. Cherry, J. A., Davies, H. M., Mehmood, S., Lavery, N. P., Brown, S. G. R., and Sienz, J. (2015). Investigation into the effect of process parameters on microstructural and physical properties of 316L stainless steel parts by selective laser melting. The *International Journal of Advanced Manufacturing Technology*, 76(5), 869-879.

27. Liverani, E., Toschi, S., Ceschini, L., and Fortunato, A. (2017). Effect of selective laser melting (SLM) process parameters on microstructure and mechanical properties of 316L austenitic stainless steel. *Journal of Materials Processing Technology*, 249, 255-263.

28. Kempen, K., Thijs, L., Yasa, E., Badrossamay, M., Verheecke, W., and Kruth, J. P. (2011, August). *Process optimization and microstructural analysis for selective laser melting of AlSi10Mg.* In 2011 International Solid Freeform Fabrication Symposium. University of Texas at Austin.

29. Trevisan, F., Calignano, F., Lorusso, M., Pakkanen, J., Aversa, A., Ambrosio, E. P., ... and Manfredi, D. (2017). On the selective laser melting (SLM) of the AlSi10Mg alloy: process, microstructure, and mechanical properties. *Materials*, 10(1), 76.

30. Kasperovich, G., Haubrich, J., Gussone, J., and Requena, G. (2016). Correlation between porosity and processing parameters in TiAl6V4 produced by selective laser melting. *Materials & Design*, 105, 160-170.

31. Majumdar, T., Bazin, T., Massahud Carvalho Ribeiro, E., Frith, J. E., and Birbilis, N. (2019). Understanding the effects of PBF process parameter interplay on Ti-6Al-4V surface properties. *PloS one*, 14(8), e0221198.

32. Rezaeifar, H., and Elbestawi, M. (2022). Porosity formation mitigation in laser powder bed fusion process using a control approach. *Optics & Laser Technology*, 147, 107611.

33. Bartlett, J. L., Heim, F. M., Murty, Y. V., and Li, X. (2018). In situ defect detection in selective laser melting via full-field infrared thermography. *Additive Manufacturing*, 24, 595-605.

34. Forien, J. B., Calta, N. P., DePond, P. J., Guss, G. M., Roehling, T. T., and Matthews, M. J. (2020). Detecting keyhole pore defects and monitoring process signatures during laser powder bed fusion: A correlation between in situ pyrometry and ex situ X-ray radiography. *Additive Manufacturing*, 35, 101336.

35. Coeck, S., Bisht, M., Plas, J., and Verbist, F. (2019). Prediction of lack of fusion porosity in selective laser melting based on melt pool monitoring data. *Additive Manufacturing*, 25, 347-356.

36. Clijsters, S., Craeghs, T., Buls, S., Kempen, K., and Kruth, J. P. (2014). In situ quality control of the selective laser melting process using a high-speed, real-time melt pool monitoring system. *The International Journal of Advanced Manufacturing Technology*, 75(5), 1089-1101.

37. Rodriguez, E., Mireles, J., Terrazas, C. A., Espalin, D., Perez, M. A., and Wicker, R. B. (2015). Approximation of absolute surface temperature measurements of powder bed fusion additive manufacturing technology using in situ infrared thermography. *Additive Manufacturing*, 5, 31-39.

38. Landowski, M., Świerczyńska, A., Rogalski, G., and Fydrych, D. (2020). Autogenous fiber laser welding of 316L austenitic and 2304 lean duplex stainless steels. *Materials*, 13(13), 2930.

39. Rogalski, G., Świerczyńska, A., Landowski, M., and Fydrych, D. (2020). Mechanical and microstructural characterization of TIG welded dissimilar joints between 304L austenitic stainless steel and Incoloy 800HT nickel alloy. *Metals*, 10(5), 559.

40. Hernández-Trujillo, S. L., Lopez-Morelos, V. H., García-Rentería, M. A., García-Hernández, R., Ruiz, A., and Curiel-López, F. F. (2021). Microstructure and fatigue behavior of 2205/316L stainless steel dissimilar welded joints. *Metals*, 11(1), 93.

41. Sun, S. H., Ishimoto, T., Hagihara, K., Tsutsumi, Y., Hanawa, T., and Nakano, T. (2019). Excellent mechanical and corrosion properties of austenitic stainless steel with a unique crystallographic lamellar microstructure via selective laser melting. *Scripta Materialia*, 159, 89-93.

42. DebRoy, T., Wei, H. L., Zuback, J. S., Mukherjee, T., Elmer, J. W., Milewski, J. O., ... and Zhang, W. (2018). Additive manufacturing of metallic components–process, structure and properties. *Progress in Materials Science*, 92, 112-224.

43. Shipley, H., McDonnell, D., Culleton, M., Coull, R., Lupoi, R., O'Donnell, G., and Trimble, D. (2018). Optimisation of process parameters to address fundamental challenges during selective laser melting of Ti-6Al-4V: A review. *International Journal of Machine Tools and Manufacture*, 128, 1-20.

44. Chu, P. K., and Lu, X. (Eds.). (2013). *Low temperature plasma technology: methods and applications.* Florida: CRC Press, 216.

45. Jerry, B. (2005), *Discrete event system simulation,* India, Pearson Education, 82.

46. Barro, Ó., Arias-González, F., Lusquiños, F., Comesaña, R., del Val, J., Riveiro, A., ... and Pou, J. (2020). Effect of four manufacturing techniques (casting, laser directed energy deposition, milling and selective laser melting) on microstructural, mechanical and electrochemical properties of co-CR dental alloys, before and after PFM firing process. *Metals*, 10(10), 1291.

47. Widder, D. V. (1967), *The heat equation,* Massachusetts, Academic Press, 450.

48. Leitz, K. H., Singer, P., Plankensteiner, A., Tabernig, B., Kestler, H., and Sigl, L. S. (2015). *AM-Non-Conventional Material: Multi-Physical Simulation of Selective Laser Melting of Molybdenum.* In European Congress and Exhibition on Powder Metallurgy. European PM Conference Proceedings. The European Powder Metallurgy Association, 1

49. Zhang, Z., Huang, Y., Kasinathan, A. R., Shahabad, S. I., Ali, U., Mahmoodkhani, Y., and Toyserkani, E. (2019). 3-Dimensional heat transfer modeling for laser powder-bed fusion additive manufacturing with volumetric heat sources based on varied thermal conductivity and absorptivity. *Optics & Laser Technology*, 109, 297-312.

50. Boltzmann, L. (1978). *Ableitung des Stefanschen Gesetzes, 1) betreffend die Abhängigkeit der Wärmestrahlung von der Temperatur aus der elektromagnetischen Lichttheorie. In Von Kirchhoff bis Planck*. Vieweg+ Teubner Verlag, Wiesbaden, 152-156

51. Leitz, K. H. (2018, October). *Thermo-Mechanical Modelling of Laser Beam Welding of Molybdenum.* In Proceedings of the 2018 COMCOL Conference, Lausanne, Switzerland.

52. Hügel, H., & Dausinger, F. (2004). *1.1 Fundamentals of laser-induced processes. Laser Applications*, Berlin/Heidelberg, Springer, 25-68.

53. Manikandan, M., Shivaprasad, U., Suvarna, A. A., Bhat, A. B., Nair, V., and Shivakrishna, G. (2014). *External Aerodynamic Analysis of TATA Nano using Numerical Tool*. 2, 393-396.

54. Voller, V. R., and Prakash, C. (1987). A fixed grid numerical modelling methodology for convection-diffusion mushy region phase-change problems. *International journal of heat and mass transfer*, 30(8), 1709-1719.

55. Mertens, A., Reginster, S., Paydas, H., Contrepois, Q., Dormal, T., Lemaire, O., and Lecomte-Beckers, J. (2014). Mechanical properties of alloy Ti–6Al–4V and of stainless steel 316L processed by selective laser melting: influence of out-of-equilibrium microstructures. *Powder Metallurgy*, 57(3), 184-189.

56. Read, N., Wang, W., Essa, K., and Attallah, M. M. (2015). Selective laser melting of AlSi10Mg alloy: Process optimisation and mechanical properties development. *Materials & Design* (1980-2015), 65, 417-424.

57. Astm, *ASTM-E8/E8M-13a, Standard Test Methods for Tension Testing of Metallic Materials,*. ASTM International.

58. Mauduit, A., Pillot, S., and Frascati, F. (2015). Application study of AlSi10Mg alloy by selective laser melting: physical and mechanical properties, microstructure, heat treatments and manufacturing of aluminium metallic matrix composite (MMC). *Metallurgical research & technology*, 112(6), 605.

59. Vilaro, T., Kottman-Rexerodt, V., Thomas, M., Colin, C., Bertrand, P., Thivillon, L., ... and Malot, T. (2010). *Direct fabrication of a Ti-47Al-2Cr-2Nb alloy by selective laser melting and direct metal deposition processes. In Advanced Materials Research*. Trans Tech Publications Ltd.,89, 586-591

60. Wang, J. H., Ren, J., Liu, W., Wu, X. Y., Gao, M. X., and Bai, P. K. (2018). Effect of selective laser melting process parameters on microstructure and properties of Co-Cr alloy. *Materials*, 11(9), 1546.

61. Marchese, G., Aversa, A., Lorusso, M., Manfredi, D., Calignano, F., Lombardi, M., ... and Pavese, M. (2018). Development and characterisation of aluminium matrix nanocomposites AlSi10Mg/MgAl2O4 by laser powder bed fusion. *Metals*, 8(3), 175.

62. Zhang, M., Sun, C. N., Zhang, X., Goh, P. C., Wei, J., Hardacre, D., and Li, H. (2017). Fatigue and fracture behaviour of laser powder bed fusion stainless steel 316L: Influence of processing parameters. *Materials Science and Engineering: A*, 703, 251-261.

63. Gunenthiram, V., Peyre, P., Schneider, M., Dal, M., Coste, F., Koutiri, I., and Fabbro, R. (2018). Experimental analysis of spatter generation and melt-pool behavior during the powder bed laser beam melting process. *Journal of Materials Processing Technology*, 251, 376-386.

64. Rosenthal, D. (1941). Mathematical theory of heat distribution during welding and cutting. *Welding journal*, 20, 220-234.

65. Concept Laser Company, (2018), “Matal Powder CL20 ES Test Report,” .

66. Mills, K. C. (2002). *Recommended values of thermophysical properties for selected commercial alloys.* Sawston: Woodhead Publishing, 65.

67. Wood, W. D., Deem, H. W., and Lucks, D. F. (1964). *Handbook of high temperature materials* no. 3.

68. Brooks, R. F., Egry, I., Seetharaman, S., and Grant, D. (2001). *Reliable data for high-temperature viscosity and surface tension: results from a European project. High Temperatures High Pressures*(UK), 33(6), 631-637.

69. Sola, A., and Nouri, A. (2019). Microstructural porosity in additive manufacturing: The formation and detection of pores in metal parts fabricated by powder bed fusion. *Journal of Advanced Manufacturing and Processing*, 1(3), e10021.

70. Obeidi, M. A., Mussatto, A., Groarke, R., Vijayaraghavan, R. K., Conway, A., Kaschel, F. R., ... and Brabazon, D. (2020). Comprehensive assessment of spatter material generated during selective laser melting of stainless steel. *Materials Today Communications*, 25, 101294.

71. Chikarakara, E., Naher, S., and Brabazon, D.(2011). *Analysis of microstructural changes during pulsed CO2 laser surface processing of AISI 316L stainless steel. In Advanced Materials Research*.Trans Tech Publications Ltd., 264, 1401-1408.

72. Shankar, V., Gill, T. P. S., Mannan, S. L., and Sundaresan, S. (2003). *Solidification cracking in austenitic stainless steel welds. Sadhana*, 28(3), 359-382.

73. Song, B., Zhao, X., Li, S., Han, C., Wei, Q., Wen, S., ... and Shi, Y. (2015). Differences in microstructure and properties between selective laser melting and traditional manufacturing for fabrication of metal parts: A review. *Frontiers of Mechanical Engineering*, 10(2), 111-125.

74. Simonelli, M., Tuck, C., Aboulkhair, N. T., Maskery, I., Ashcroft, I., Wildman, R. D., and Hague, R. (2015). A study on the laser spatter and the oxidation reactions during selective laser melting of 316L stainless steel, Al-Si10-Mg, and Ti-6Al-4V. *Metallurgical and Materials Transactions A*, 46(9), 3842-3851.

75. Zhou, B., Xu, P., Li, W., Liang, Y., and Liang, Y. (2021). Microstructure and anisotropy of the mechanical properties of 316L stainless steel fabricated by selective laser melting. *Metals*, 11(5), 775.

76. Yusuf, S. M., Chen, Y., Boardman, R., Yang, S., and Gao, N. (2017). Investigation on porosity and microhardness of 316L stainless steel fabricated by selective laser melting. *Metals*, 7(2), 64.

77. Spierings, A. B., and Levy, G. (2009, September). *Comparison of density of stainless steel 316L parts produced with selective laser melting using different powder grades.* In 2009 International Solid Freeform Fabrication Symposium. University of Texas at Austin.

78. Li, R., Liu, J., Shi, Y., Wang, L., and Jiang, W. (2012). *Balling behavior of stainless steel and nickel powder during selective laser melting process.* The International Journal of Advanced Manufacturing Technology, 59(9), 1025-1035.

79. Advanced Powders and Coatings Inc. (2021), AlSi10 Mg Powder Data Sheet, *AP&C*, Québec.

80. Dai, D., and Gu, D. (2015). Effect of metal vaporization behavior on keyhole-mode surface morphology of selective laser melted composites using different protective atmospheres. *Applied Surface Science*, 355, 310-319.

81. Röttger, A., Geenen, K., Windmann, M., Binner, F., and Theisen, W. (2016). Comparison of microstructure and mechanical properties of 316 L austenitic steel processed by selective laser melting with hot-isostatic pressed and cast material. *Materials Science and Engineering: A*, 678, 365-376.

82. Zhong, Y., Liu, L., Wikman, S., Cui, D., and Shen, Z. (2016). Intragranular cellular segregation network structure strengthening 316L stainless steel prepared by selective laser melting. *Journal of Nuclear Materials*, 470, 170-178.

83. Wu, H., Ren, J., Huang, Q., Zai, X., Liu, L., Chen, C., ... and Li, R. (2017). Effect of laser parameters on microstructure, metallurgical defects and property of AlSi10Mg printed by selective laser melting. *Journal of Micromechanics and Molecular Physics*, 2(04), 1750017.

84. Wu, H., Ren, Y., Ren, J., Liang, L., Li, R., Fang, Q., ... and Baker, I. (2021). Selective laser melted AlSi10Mg alloy under melting mode transition: Microstructure evolution, nanomechanical behaviors and tensile properties. *Journal of Alloys and Compounds*, 873, 159823.



GAZİ GELECEKTİR...